EXPERIMENTAL STUDIES ON THE DEVELOPMENT OF FIBER BRAGG GRATING BASED SENSORS FOR STRUCTURAL HEALTH MONITORING

A Thesis Submitted in Partial Fulfillment of the Requirements for the

Award of the Degree

of

DOCTOR OF PHILOSOPHY

by

PATHI MUNENDHAR

DEPARTMENT OF PHYSICS

INDIAN INSTITUTE OF TECHNOLOGY GUWAHATI

GUWAHATI-781039, INDIA

AUGUST - 2014

The present thesis dedicated to

my parents

STATEMENT

I hereby declare that the research work presented in this thesis entitled "EXPERIMENTAL STUDIES ON THE DEVELOPMENT OF FIBER BRAGG GRATING BASED SENSORS FOR STRUCTURAL HEALTH MONITORING" is carried out by me under the supervision of **Prof. Sunil K. Khijwania**, Associate Professor, Department of Physics, Indian Institute of Technology Guwahati. The contents of this thesis have not been submitted to any other Institute or University for the award of any degree.

Date: 19/08/2014

Pathi Munendhar

Research student
Department of Physics
Indian Institute of Technology-Guwahati
Assam-781039
India

CERTIFICATE

This is to certify that work contained in the thesis entitled "EXPERIMENTAL STUDIES ON THE DEVELOPMENT OF FIBER BRAGG GRATING BASED SENSORS FOR STRUCTURAL HEALTH MONITORING," by **Mr. Pathi Munendhar** (Roll No. 09612115), a student of department of physics, Indian Institute of Technology Guwahati, for the award of Doctor of Philosophy, has been carried out under my supervision. The contents of this thesis have not been submitted to any other Institute or University for the award of any degree.

Date: 19/08/2014

Prof. Sunil K. Khijwania

Associate Professor, Department of Physics
Indian Institute of Technology-Guwahati
Assam-781039
India

ACKNOWLEDGEMENTS

First and foremost, I would like to express my deepest gratitude to my respected guide **Prof. Sunil K. Khijwania** for providing me the opportunity to work under his supervision. He has supported me throughout my thesis with his knowledge, ideas and patience which gave me right path in all the time of research for and writing of this thesis. His stimulating suggestions, encouragement and training have made him a source of inspiration throughout my life. I am also thankful for the excellent example he has provided as a successful physicist and professor.

I would like to express my sincere thanks to my doctoral committee members, **Dr. Ashwini K. Sharma, Prof. A. Srinivasan** and **Dr. Anil Verma** for reviewing my research work regularly and for all valuable suggestions.

I would also like to express my thanks to Prof. Pratima Agarwal, Department of Physics, Dr. Hemant B. Kaushik, Department of Civil Engineering, and Prof. S. K. Dwivedy Department of Mechanical Engineering for their support.

I am highly indebted to the members in Fiber Optics lab, Dr. Aneesh, Manoj, Meeth, Sougata, Debopam, Shaival Buch, Nitesh Dasmana, Devi, Chakraborthy, Uttam Nandi, and Hament for their immense support and help.

My special thanks to the staffs of Department of Physics, Mr. Basab Purkhastya, Dr. Sidananda Sarma, and staff of Civil Engineering Department Mr. Biswajit for their support and timely assistance.

I am highly thankful to research students of Mechanical Engineering Department, Arun, Anand, Vinod, and Ramesh. I am also thankful to all my batch mates and my friends from chemistry department for their help at various levels during my stay at IIT Guwahati.

Finally, I am forever obliged to my parents and sister for their understanding, endless patience and encouragement when it was most required.

Guwahati

August-2014 Pathi Munendhar

ABSTRACT

The present thesis work is focussed on the development of fiber Bragg grating (FBG) based novel all-optical sensors to monitor tilt, vibration, strain and RH, which are some of the most important parameters in structural-health-monitoring. Sensors are developed to achieve manifold sensitivity enhancement, possibly with a tunable response characteristics and without any inherent measurement instabilities. First, a novel, all-optical, temperature insensitive, pendulum based sensor design strategy with inherent enhanced tuning capability for its sensitivity is characterized. An excellent sensitivity (~0.0626 nm/^{o}) over a dynamic range of ±10^{o} that can further be nonlinearly tuned is established for this sensor. A completely reversible linear response with a much improved resolution (0.008^{o}), accuracy (±0.36^{o}), maximum discrepancy (less than ±0.0231nm) and maximum angular uncertainty (~±0.34^{o}) are established for this sensor. In order to capture tilt effectively with enhanced stability, a non-pendulum type design strategy for FBG based tilt sensor is proposed. A better resolution (better than 0.004°), better accuracy (~±0.05°) and a lesser maximum discrepancy (~±0.001nm) with a very high degree of reversible and repeatable response over the observed dynamic range is achieved. Next, a simple design strategy of FBG based 2-axial vibration sensor is proposed and experimentally demonstrated. An excellent capability of resolving externally applied signals having frequency in 10Hz to 350Hz and the acceleration in 0.65 to 70m/sec^{2} range is observed. Afterwards, research work was focussed to enhance inherent strain sensitivity of FBG. For this, a single FBG sensor with corrugated cladding structure over the FBG carrying core is designed and experimentally investigated. Proposed structure across the FBG section splits a single FBG into multiple & independent FBGs. A relative strain sensitivity enhancement of more than 10 times is observed, which is impossible to realize with a normal FBG. Finally, FBG based humidity sensor is developed employing a novel mechanism of effective-index modulation with an ambition to achieve widest possible dynamic range and optimum sensitivity. To achieve these objectives, fiber diameter in the grating region was reduced to a lowest possible working limit (~ a few microns). A wide linear dynamic range ~3 – 94 %RH with good sensitivity of ~0.082 pm/%RH is realized. The response of the developed sensor is observed to be completely reversible with an appreciably stable characteristic during repeatability and reliability tests.

LIST OF CONTENTS

LIST OF FIGURES

LIST OF TABLES

Chapter 1

Introduction

Sensing of various parameters is vital for controlling and monitoring various industrial, scientific, and environmental processes. For an effective control mechanism, one requires an easier acquisition of valuable information about process-specific parameter (termed here-in-after as measurand), which is done by employing a suitable sensing device, termed as sensor. The easier acquisition of parameter-specific information through these sensors that need to be precise is realized by mapping change in the magnitude of any desired and application-specific physical parameter onto a more effective change in the magnitude of another and more suitable parameter, that can be measured more conveniently, directly and perhaps more accurately [1]. These application and/or process-specific measurands, in general, span anything from optical signals (e.g., intensity, wavelength, state of polarization and phase of electromagnetic radiation), mechanical/physical signals (e.g., force, pressure, velocity, mass flow, rotation, vibration, tilt, strain, stress, torsion, refractive index etc.), thermal signals, electric & magnetic signals (e.g., voltage, current, charge, resistance, inductance, capacitance, pulse duration, frequency, dielectric constant, magnetic flux density, magnetic field direction and permeability etc.) to chemical and/or biological signals (e.g., chemical composition, concentration, pH, malignancy, blood glucose, relative humidity, gas concentration etc.). Hence, almost all areas of science & engineering as well as industrial applications rely on the information gathered by sensors for an efficient process-control and performance optimization. This makes sensors indispensable in today's science & technological as well as industrial-growth age. Guided by the enormous scope

of sensing technology and the related scope in futuristic market share, lots of research efforts have been devoted over the past few decades for the development of an ultra-precise, reversible and repeatable sensors for various applications. Today millions of sensors are deployed throughout the world. It is difficult to think of any area of engineering which does not make use of sensing technology.

The history of sensor lies in the nature. There are various elements in the nature that inherently respond while being exposed to certain perturbations. Simplest examples are (a) that of mercury, which is inherently characterized with finite thermal expansion coefficient; and (b) that of naturally occurring ores, which are inherently characterized with magnetic properties and specifically align themselves if exposed to a magnetic perturbation. The list goes on. Conventional/traditional sensors are based on (or employ smartly and efficiently) such material and exploit some of their potential inherent properties, which leads to a unique response characteristic (hysteresis loop of a ferromagnetic material as one example) when exposed to an applied perturbation. Apart from the two inherent properties (thermal and magnetic) mentioned above, other inherent properties that are potentially exploited by the conventional/traditional sensors could be electrical, mechanical or chemical to name a few. As an example, conventional strain sensor exploits piezo-electric effects where a piezo-resistor measures strain-changes through the resistance variations. Further, a piezoelectric material produces a potential that is proportional to the applied pressure; this property is exploited for designing a conventional pressure sensor. Another example is capacitive-sensor, where various parameters of interest, e.g., humidity [2], strain [3], acceleration [4], and tilt [5], are monitored through the changes in the capacitance. On the chemical side, simplest conventional pH sensor that exploits chemical

properties of material is pH indicator whose colour changes around particular pH value; and that way, enables an appropriate measurement of the pH of a given solution. These are just a few examples of the conventional sensors. In summary, there are many schemes that are employed to design a suitable conventional sensor for monitoring various parameters. Though, being highly precise with an extremely good characteristic sensitivity, these conventional/traditional sensors have certain major demerits. Their performance is surrounding-condition-specific, i.e., they perform well under certain conditions but, as an example, their performance degrades drastically under the presence of strong environmental electromagnetic/radio-frequency signals, and are particularly inoperative in hazardous environments. One cannot even think of the realization of remote-sensing and multiplexing. As a result, these conventional sensors fall short of expectations at many of the aspects from the field deployability and application point of view. This fuelled enormous thoughts for the development of an alternate sensing-technology that can inherently infuse optimum sensitivity, long-term performance durability, immunity to electromagnetic interference/electrostatic discharge, operatability under hazardous environments and ability for remote-sensing as well as multiplexing.

One possibility to overcome these limitations is switching sensing to the optical domain. Here, being optical (lightwave), the sensing signal is completely unaffected by any surrounding electromagnetic/radio-frequency signal; and that way, immediately overcomes a set of demerits of conventional sensors. In principle, optical sensors measure the change/variation in a given parameter by effectively mapping them in an accurate change in any one of the optical characteristics, e. g, intensity, frequency, wavelength or the phase of the lightwave. Nevertheless, almost all of the optical sensors developed since the first reported in 1930 [6], were based on the

intensity variation through the measurand–initiated absorption/quenching of the optical signal. Invention of laser gave another thrust to optical sensing; enabling the development of more effective laser and holography based all-optical sensors that were characterized with a better resolution. One of the examples of optical sensor is optical proximity sensor, which is widely used for a variety of security as well as consumer-based applications. Another example is the optical tilt sensor where laser and holography techniques were employed to monitor the inclination [7]. Another excellent application of utilization of optical technique is the development of high precision optical sensors for chemical/gas concentration detection, where fluorescence characteristics of certain suitable dyes were exploited to detect CO_2 and O_2 [8-9], and optical responsitivity (e.g., optical absorption) of certain chemical compounds in a thin sensing film were exploited to detect CO, NO and H_2 [10-12]. In another research work, an optical sensor was reported for the monitoring of displacement [13]. Though, the reported optical sensors overcome certain limitations of existing conventional sensors and are characterized with a better sensitivity, they have their own limitations. In general, they are bulky, complicated, highly alignment sensitive; and in certain situations such as on foggy/rainy days, their performance gets seriously degraded. Further, they cannot be deployed in hazardous conditions like places of intense radiation, high voltage environments, high temperature etc. Importantly, remote-sensing and multiplexing are impossible through these sensors. In summary, such optical sensors are impractical for real-field applications.

Sensing technology got revolutionized with the adoption of fiber optics. In fact, discovery of optical fiber during early seventies was a major breakthrough for telecommunication industry. In the very early days when the fiber optics technology was still evolving for telecommunication

purposes, an undesirable sensitivity of optical fiber towards various external factors such as bends, microbends, pressure etc. was noticed. Initially, enormous efforts were made to reduce the sensitivity of fiber to these external perturbations as it degraded the efficiency of a telecommunication system. However, soon it was realized that the exceptional sensitivity of optical fibers to external perturbations can be very effectively exploited for sensing various parameters of interest. Thus, the field of optical fiber sensor (OFS) was born. Exceptional technological advancements in the field of fiber optics as well as in the associated optoelectronic industries leading to the availability of very low-loss optical fiber in different wavelength windows and very sophisticated optical sources/interrogators have given tremendous thrust and made a great impact on the development of optical fiber sensors for various applications, spanning engineering (civil, mechanical, aeronautical, chemical, electrical, automobile etc.), biomedical, general sciences to homeland security as an example. Enormous and remarkable inherent advantages offered by optical fiber sensing technology as against that of the conventional sensors are the reason for the global thrust in the area of optical fiber sensor research & development. Some of the key advantages of optical fiber sensors are [14]:

1. A very high sensitivity over the traditional sensors.
2. Ease of miniaturization and hence the possibility of the development of very small, light and flexible sensors.
3. Low-loss optical fibers in conjugation with fiber amplifiers not only allow propagation of lightwave signals over thousands of kilometres but also enable dense wavelength-division-multiplexing (DWDM) to realize over 100Tb/s-km optical fiber communication systems. Such a large information carrying capacity over thousands of kilometres enables effective remote-sensing.

4. Huge amount of bandwidth and hence massive information-carrying-capacity (ICC) offered by an optical fiber, which is impossible to realize with an electrical system, enables (a) achieving a high sensing-information-density through a single optical channel where each of the optical characteristics (wavelength, phase, intensity etc.) are independently and simultaneously encoded by the external perturbations, (b) multiplexing large number of sensors, each characterised at a particular optical channel over a single fiber transmission line, (c) distributed sensing, i.e. continues sensing along the entire fiber transmission line, and (d) multi-parameter sensing.
5. As optical fibers are made from the insulating materials, optical fiber sensors are inherently electrically isolated from the interrogating electronics.
6. Being optical, primary signal cannot be subjected to electromagnetic interference/radio-frequency interference and has zero risk against fire/sparks. This makes optical fiber sensor highly reliable.
7. Characterized with small volume and light weight, optical fiber sensors can easily be surface-mounted or un-intrusively embedded in composites.
8. Optical fiber sensors can be deployed over a wider temperature range as well as in a harsh environment.

Owing to these numerous but distinct inherent advantages over the conventional/optical sensors, optical fiber based sensors have convincingly established themselves as an alternate to the traditional sensing schemes [15-16]. Almost all the parameters of practical importance, such as, pressure [17], temperature [18], liquid level [19], refractive index [20], pH [21], antibodies [22], electric current [23], voltage [24], rotation [25], displacement [26], acceleration [27], acoustic

[28], electric and magnetic field measurement [29, 30], tilt [31], torsion [32], strain [33] etc. are being successfully and accurately monitored by optical fiber sensors not only in the test-bed set-up but also in the real-field environment.

Optical fiber sensors can be broadly classified as an extrinsic or an intrinsic sensor. In an extrinsic sensor, fiber acts merely as a conduit to guide the lightwave signal to- and from- the sensing head. Modulation of the optical signal by an environmental/external perturbation takes place outside the fiber. On the other hand, in an intrinsic sensor, fiber itself acts as a sensor. Here, one of the inherent characteristics of the guided lightwave signal, e.g., phase, polarization, wavelength, intensity gets modulated within the fiber by an environmental/external perturbation. As obvious, an intrinsic fiber sensor can be further classified on the basis of the employed optical modulation scheme and can be termed, for example, as an intensity-modulation based optical fiber sensor or a wavelength-modulation based optical fiber sensor and so on. Most popular schemes among researchers in terms of ease of realization are intensity, phase and wavelength modulation.

Though, optical fiber sensors employing intensity-modulation schemes are simple to fabricate and fall under the popular category, performance of such sensors suffers from the source power fluctuations. Importantly, such sensors are impractical from the point of view of real-field applications, remote-sensing and multiplexing. Most suitable mechanism that fully exploits tremendous opportunities/merits offered by fiber optics (e.g., huge bandwidth, enormous ICC, DWDM etc. mentioned above) is the wavelength-modulation scheme. Optical fiber sensors employing wavelength-modulation schemes are immune to the source power fluctuations.

Further, in the absence of non-linearity effects, wavelength-encoded lightwave signal carries exact information of the sensing parameter without any degradation or a cross-talk. There are various ways to employ wavelength-modulation scheme. Some of these are wavelength dependent absorption, luminescence, dispersion, interference and scattering. However, since its invention and successive advancements [34], in-fiber Bragg gratings (FBGs) have become synonym to the optical sensing technology as for as real-field applications are concerned. The reason is, apart from inheriting the advantages of fiber optics, FBG sensors are characterized with additional advantages, such as, (1) inherently self-referencing, (2) ease of designing spectral and phase response of FBG as per the requirement, (3) capability of multiplexing a large number of FBGs on a single fiber channel, (4) ease of employing DWDM, spatial-division-multiplexing, time-division-multiplexing (TDM) and quasi-distributed sensing, (4) insensitive to the fluctuations in the irradiance of the illuminating source, (4) compatibility for the application such as strain mapping in advance composite materials where small diameter probes are essential to name a few. Owing to these enormous merits of FBG sensor, they have emerged as a most viable and integral solution for almost all of the engineering/industrial applications, such as, structural-health-monitoring (SHM), mechanical engineering, aeronautical engineering, communication engineering, biomedical/micro-fluidics to name a few. [35]. Importantly, the class of optical fiber sensors, which are based on wavelength modulation scheme, dominantly uses in-fiber gratings (FBG/long period gratings (LPG)) as the constituting sensing element.

A grating structure that facilitates strong coupling between identical or nearly identical forward- and counter-propagating fiber modes in a single-mode fiber is termed as short period grating or fiber Bragg grating (FBG) [34]. FBG is an intra-core periodic refractive index (RI) perturbation

along a small length of a single-mode fiber. When light from a broadband source is launched into the fiber core carrying FBG, it gets scattered by each grating plane and suffers extremely weak reflection. However, under specific condition termed as Bragg condition, reflected light from each grating plane would be in phase and would interfere constructively in the backward direction. This gives rise to strong reflection spectrum centered at a specific wavelength termed as Bragg wavelength (λ_B). On the other hand, other wavelength components would be transmitted by the grating, giving rise to the transmission spectrum of the FBG as depicted in Fig. 1.1. Bragg condition is the manifestation of energy and momentum conservation [36].

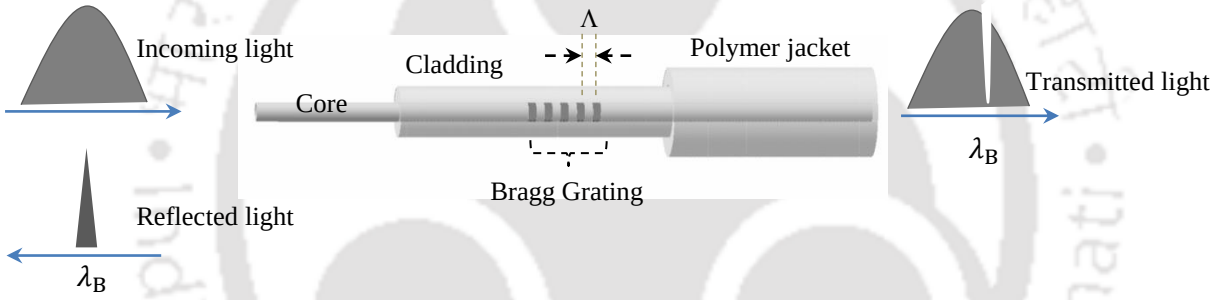

Figure 1.1: *Schematic of fiber Bragg grating principle.*

Energy conservation requires the frequency of the coupled radiations (forward and backward) to be the same. On the other hand, momentum conservation requires the forward mode propagation constant ($\overrightarrow{\beta_f}$) plus the grating wave-vector ($\vec{K}$) to be equal to the backward mode propagation constant ($\overrightarrow{\beta_b}$).

$$\overrightarrow{\beta_b} = \overrightarrow{\beta_f} + \vec{K} \quad 1.1$$

As $\overrightarrow{\beta_b} = -\overrightarrow{\beta_f}$ and $|\vec{K}| = \frac{2\pi}{\Lambda}$ above condition simplifies to

$$\lambda_B = 2\Lambda n_{eff} \quad 1.2$$

As can be observed from Eq. (1.2), the wavelength that satisfies Bragg condition in a uniform fiber grating depends on the effective-refractive-index (n_{eff}) of the mode and the grating-pitch (Λ). Grating-pitch is dictated by the phase-mask used for inscribing the FBG. For a standard optical fiber, effective-refractive-index can only be modulated by applying strain/temperature perturbations through strain-optic/thermo-optics effects. Further, owing to the finite elasticity and thermal expansion coefficient of the material used to fabricate the fiber, strain/temperature variation across the grating region also modulates the grating pitch. These strain & temperature dictated effects leads to a shift in the Bragg wavelength. This wavelength shift that can be derived from Eq. (1.2) is mathematically expressed by the following relation [37]:

$$\Delta\lambda_B = 2\left(\Lambda\frac{\partial n_{eff}}{\partial L} + n_{eff}\frac{\partial \Lambda}{\partial L}\right)\Delta L + 2\left(\Lambda\frac{\partial n_{eff}}{\partial T} + n_{eff}\frac{\partial \Lambda}{\partial T}\right)\Delta T \qquad 1.3$$

Here, first term corresponds to the strain-optic effect, second term corresponds to elongation/compression of the optical fiber, third term corresponds to the thermo-optic effect and the fourth term corresponds to the thermal expansion of the optical fiber. Above equation can be simplified to [37]:

$$\frac{\Delta\lambda_B}{\lambda_B} = (1-\rho_\varepsilon)\Delta\varepsilon + (\alpha+\xi)\Delta T \qquad 1.4$$

where, $\Delta\varepsilon$ is the change in longitudinal strain, ΔT is the change in temperature, ρ_ε is photo-elastic coefficient of the fiber, ξ is thermo-optic coefficient (~8.6x10^{-6} for germanium doped silica fiber core) and α is thermal expansion coefficient of the fiber (~0.55x10^{-6} for silica fiber). Thus, as can be observed from Eq. (1.3), FBG is inherently sensitive to strain and temperature perturbations both. In order to realize an independent strain/temperature sensor employing FBG, one needs to device a smart mechanism to decouple temperature/strain information. Various

techniques/designs have been successfully employed in order to abandon the effect of one parameter on the measurement [38-40], especially that of the temperature. As mentioned earlier, FBGs have been used for a wide variety of sensing applications including monitoring of civil infrastructures, smart manufacturing and non-destructive testing (composites, laminates, etc.), remote sensing (oil wells, power cables, pipelines, space stations, etc.), smart structures (airplane wings, ship hulls, buildings, sports equipment, etc.), as well as traditional strain, pressure and temperature sensing [41]. Thus, apart from strain and temperature, various other parameters (e.g., pressure, tilt, vibration, torsion, acceleration, displacement, flow, field intensity etc.) are also required to be monitored in different engineering applications/industrial processes. In order to develop FBG based sensors, these other parameters that are to be monitored are preferably and strategically mapped in the strain domain. Numerous attempts have been made worldwide to realize such FBG based sensors. Today, almost all the parameters of practical importance such as strain [42], temperature [42], pressure [43], liquid level [44], tilt [45], rotation [46], displacement [47], acceleration [48], electric and magnetic measurements [49], acoustic [50], torsion [51], humidity [52], and refractive index [53] etc., are successfully and accurately monitored by FBG sensors in real-field environment.

As observed from the above discussions, being versatile, optical fiber sensors (and specially, the FBG sensors) become an integral part of the monitoring and sensing systems for almost all of the engineering/industrial applications. One of the most important fields of application which has witnessed tremendous rise recently and has attracted lots of interest as for as human security is concerned with a maximum OFS industry share is the structural-health-monitoring (SHM). With the diverse advancements in the global human civilization as well as in the science and

technology that led to an unimaginable growth of civil infrastructures, synchronized structural-health-monitoring (SHM) becomes a serious issue to deal with. Any reason among (a) possible errors in design and construction, (b) overload, (c) environmental degradation from strong winds, heavy rains, humidity, huge temperature variations, and (d) nature's impact such as earthquakes, storms or floods imposes serious threat and induces adverse changes (damage/deterioration) in the health condition of various civil infrastructures such as bridges, dams, tunnels, high-rise buildings, rail transport network etc. These adverse changes (damage/deterioration) cannot be anticipated during the design and realization stages of such infrastructures [54]. As an example, a serious outcome of these reasons/effects is the accumulation of unwanted strain distribution across certain locations of the structures, termed as defect centers, which may finally lead to the collapse of such structures and hence, casualty to human lives. Damage identification and prevention of its evolution in any civil engineering infrastructure, thus, becomes an integral part of SHM [55]. SHM is the process of assessing the state of the health (e.g., damage) of infrastructures by continuously monitoring them in real-time through the measurement of various parameters that affect them. These parameters depend on the construction material, environmental conditions and expected degradation phenomena. Further, they vary from structure to structure. For example, tilt could be more important in the case of an under-water canal or ropeway bridge, whereas vibration for railway transport network. In general, these parameters are classified as mechanical (strain, deformation, displacement, crack opening, stress, and load), physical (temperature, humidity, pore pressure etc.) and chemical (pH, oxidation, corrosion, carbonation, penetration, and timber decay) [54]. Such monitoring that includes the real-time and continuous access to the variation of so many parameters cannot be done solely by routine manual inspection where engineers inspect the structure with an unaided eye. Such

procedures are time consuming, faulty, inappropriate and inaccurate. The reason that OFS based on FBG have become synonym and only feasible solution to SHM is the exceptional features offered by these sensors. Among the other features/merits, accessibility to enormous sensing data through a single fiber network, accessibility to already existing communication network with a common transmission band ("C" band) that naturally leads to DWDM and remote-sensing, highly precise, secure, reliable, low-cost, robust under hazardous conditions with an extremely high sensitivity are the dominant one for the preference of FBG sensors in SHM. Numerous attempts have been made to realize FBG based smart OFSs to monitor various parameters of interest in SHM. Some of the important parameters to be monitored in SHM are tilt, vibration, strain, and humidity.

Inclination or tilt-angle monitoring is of extreme importance for the health of various civil infrastructures such as tunnel, bridges, dams, etc. In addition, it is also one of the key parameters to be monitored in mechanical, instrumentation, robotics, aeronautical engineering applications [45]. Hence, a very accurate, highly sensitive, compact tilt monitoring sensor-system capable of resolving lowest possible tilt with a large dynamic range would be of extreme importance. Most of the conventional tilt sensors are electronic in nature and transform inclination information into electric signals either through magnetic effects or through capacitive effects [56-58]. For example, slight displacement of the pendulum mass is transferred into an electrical signal by inductive/capacitive methods in pendulum based inclination sensors [56]. In some other electronic tilt sensor, either the small displacement of the magnetic core is transferred into a voltage by an inductive detection of the magnetic fluid, which used to be a signature of the

applied tilt [56], or the relative motion of a dielectric fluid between two semi-circular shaped electrodes is utilized to realize a capacitive based tilt measurement in micromechanical capacitive inclination sensor [57]. However, inherent limitations such as vulnerability towards electromagnetic/radio-frequency interference (EMI/RFI), deployability in harsh environments and inability towards multiplexing/remote-sensing/distributed-sensing pose serious problem for such sensors and make them unthinkable for real-field applications. As mentioned earlier, optical sensors overcome some of the shortcomings of the conventional sensors. Nevertheless, only a few attempts have been made to realize all-optical tilt sensors employing laser based sensing technology. For example, Zhong et al. have reported an optical tilt sensor based on wavefront sensing [59]. Laser based interferometric tilt sensors are reported in [60, 61]. In another work, Hua et al. in [62] have reported tilt sensor based on laser interference; whereas Xiaoyong et al. in [63] have reported another tilt sensor based on laser and holographic technique. However, being bulky and complicated in design configuration, and extremely alignment sensitive, all these methodologies are in fact impractical for real field applications. In order to overcome these limitations, one needs to switch to OFS. However, only a few attempts have been reported in the literature towards the development of optical fiber sensors for inclination/tilt-angle monitoring. As an example, Yuan [64] has reported a push-pull fiber optic tilt sensor based on Mach-Zehnder reflector. Lee et al. [65] have reported another tilt sensor which employed optical fibers as mere transceivers to capture reflected light upon applying tilt. In another such attempt, Bajic et al. [66] have reported tilt sensor employing lead-in and lead-out optical fibers separated by a suitable distance in a liquid container. Upon rotation, liquid surface reorients itself, leading to a variation in the captured optical power by the lead-out fiber. Though, reported sensors exhibit a good capability in capturing the applied tilt, observed sensitivity and tilt-angle resolution along with

inherent measurement errors associated with complicated design strategies were critical limitations in such attempts. Recently, a few FBG based attempts have been made for inclination/tilt measurement [67-72]. Guan et al. in [67] employed a vertical pendulum structure and four FBGs. Dong et al. in [68] employed pre-deflections of steel flakes through a cantilever pendulum to map the tilt angle onto the grating chirp. Chen et al. in [69] proposed a design strategy based on single FBG. Bao et al. in [70] employed another vertical pendulum structure and four FBGs. Though a very high resolution was achieved in [67], the performance in these studies was limited by the design constraints such as a cantilever based pendulum suspension mechanism resulting in unwanted and inherent mechanical frictions at the joints during the rotation and corresponding instabilities in [67, 68, 70] and pre-deflections of steel flakes with a complicated pendulum suspension mechanism in [68]. Also, the sensitivity in all these reported sensors was limited. He et al. in [71] reported a tilt sensor based on three FBGs in series on a single fiber making an inverted pyramidal structure with three fiber arms and a mass (bob) suspended from the vertex. A very high-sensitivity was observed. However, retrieval of the tilt was based on a very intricate mathematical analysis. Ni et al. [72] reported another tilt sensor based on four FBGs in series on a single fiber making an inverted pyramidal structure with four fiber arms and a mass (bob) suspended from the vertex. Nevertheless, stability of the sensor and the cross-sensitivity to unwanted perturbations in both the designs were important issues. As the mass is hanged directly to the fiber loop, any unwanted add-on oscillation is expected to lead to a random vibration/oscillation of the fiber-mass pendulum system of both the sensor designs in [71, 72]. This is bound to give measurement errors and will make these sensors highly unstable. Also, there is a possibility of slacking of one fiber arm in the plane of inclination during the tilt.

Measurement of structural vibrations induced by instantaneous impacts or natural environmental perturbations is a critical issue, particularly in civil engineering applications and rail transport network to name a few. Response of any given structure to such vibrational perturbations depends on the natural frequency of such structures, which is dictated by their physical properties. Often, a decrease in its value results in a damage proliferation [73]. Damage identification and prevention of its evolution in any civil engineering infrastructure, thus, becomes an integral part of SHM. Vibration measurement analysis is a vital approach to implement SHM strategies. Vibration sensors such as accelerometers are one of the key smart-diagnostic systems to study the impact of vibration perturbations in this strategy. Conventional vibration sensors are electronic in nature as they exploit either piezoelectric or capacitive effects. Such existing electronic vibration sensors find numerous useful applications; however, they have their own inherent limitations [74]. On the other hand, several research efforts have also been made to develop optical fiber vibration sensors. These efforts mainly employed cantilever based mechanism where the vibration is encoded in terms of uniaxial misalignment between two similar or different kinds of optical fiber [75-77]. A more complicated sensing scheme that integrated Moiré fringe with fiber optics is reported in [78]. Recently, a variety of optical fiber vibration sensors exploiting interferometric techniques have been reported [79-81]. However, performance of all these optical fiber vibration sensors which are based on the intensity modulation scheme suffers from the source power fluctuations. Also, these sensors are unfit for multiplexing and distributed sensing. Importantly, being one-dimensional, they are unable of resolve arbitrary vibrations. Some attempts have also been made to develop FBG based vibration sensors. For example, Berkoff et al. in [82] embedded FBG element into a thin layer of elastomer between a rigid base and a seismic mass. Sensor suffered seriously from the cross-axis response.

Zhu et al. in [83] and Zhou et al. in [84] employed vibration induced chirping mechanism of a surface loaded FBG. Such power-referenced sensing scheme suffers from light source power fluctuations and is unsuitable for distributed sensing. Weng et al. in [85] employed a very complicated sensing structure based on a U-shaped rigid cantilever beam, a diaphragm and a FBG fixed between the two legs of the cantilever beam. Researcher in [86] reported another diaphragm based sensor employing a centrally attached inertial mass and the FBG. Another sensor design based on a tapered fiber and tilted FBG was employed in [87]. Au et al. in [88] reported FBG based pendulum structure for vibration sensor while employing chirp-free mechanism. In another attempt, Stefani et al. employed microstructured polymer optical fiber Bragg grating to capture vibration/acceleration [89]. Temperature cross-talk, cross-axis sensitivity and complexity in designing remained some of the serious issues with all these sensors reported in the literature. Importantly, being uniaxial, they are incapable of resolving the impact to two-dimensional vibration perturbations. In order to address the later issue and to develop two-axial sensor, Fender et al. employed mass loaded multicore optical fiber carrying FBG in all the four cores of the fiber [90]. However, fabrication of such complicated structure required high level of sophistication and increased the experimental difficulty.

Strain accumulation and its unwanted distribution, as mentioned earlier, is a serious outcome of design or construction defects/environmental degradation/overload/calamity such as earthquake and poses a serious threat to the integrity and health condition/life-span of various infrastructures. Hence, an accurate measurement of a strain plays a crucial role in determining crack, damage, fatigue, vibration etc. in SHM. In particular, a strain monitoring system with high sensitivity in addition to a high accuracy and optimum strain resolution is best suited to mitigate

risks and to prevent disasters at a very early stage of degradation. Conventional strain sensors as well as electronic strain gauges are based on the electrical properties of the sensing material, which transfer induced strain information into an electric signal [91, 92]. A reasonably good sensitivity can be achieved using such conventional sensors. On the other hand a few optical fiber strain sensors (OFSS) have been reported in the literature. As an example, Arregui et al. in [93] reported an optical fiber strain gauge employing intensity modulation through the bending of a bi-conically tapered single-mode fiber. Intensity fluctuation of the optical source posed a challenging limitation. In another attempt to enhance the strain sensitivity, Li in [94] reported a fiber optic strain sensor employing multimode interference in single mode–multimode–single mode fiber structure. Observed strain sensitivity was roughly double of the strain sensitivity offered by FBG. Apart from such OFSS, numerous attempts have been made to realize FBG based strain sensor. As mentioned earlier, FBG sensors are not only used to monitor strain and temperature, but are also desirable to monitor various other parameters critically important in SHM as well as in other engineering applications and processes. In order to develop FBG based sensors, these other parameters are preferably mapped in strain domain. FBG fabricated in a standard telecom fiber offers a limited strain sensitivity of ~1.2 pm/με around 1550 nm wavelength. Limited (small) strain sensitivity of FBG not only affects an early prediction of the degradation of civil infrastructures but also dictates a limited sensitivity to FBG sensors for other parameters. Hence, devising a mechanism that can increase the strain sensitivity of FBG will not only meet the requirement of early prediction of degradation in SHM as mentioned above, will also increase the overall sensitivity of all FBG sensors employing strain-based mechanism. Recently, few attempts have been made to realize FBG strain sensor with enhanced strain sensitivity. For example, James et al. in [95] employed two slightly different FBGs on either side

of the splice between two fibers of different diameters. While applying strain to this structure, FBG in reduced fiber diameter displayed greater strain sensitivity than the FBG in normal fiber diameter. A maximum strain sensitivity of 0.81pm/με was achieved. Modifying the sensing structure of [95], Mondal et al. in [96] designed FBG strain sensor employing single FBG with a reduced fiber diameter over half of the length of the FBG. In agreement with [95], a strain sensitivity enhancement was observed with a very limited dynamic range of ~200με. On the other hand, Fraz et al. in [97] devised a strain sensor formed by a single FBG in series with a fused fiber taper. Authors successfully demonstrated strain sensitivity tuning below the standard strain sensitivity of normal FBG. In another attempt to enhance the sensitivity, Ren et al. in [98] devised a strain sensor employing a single FBG with a specific gripper tube. A strain sensitivity enhancement by a factor of two in comparison to the strain sensitivity of normal FBG was achieved. Xu et al. in [99] employed chirped FBG in a tapered optical fiber to devise another strain sensor. A little better sensitivity in comparison to the normal FBG was observed. In another work, Gu et al. [100] devised a strain sensor employing micro/nano Bragg grating structure in a polymer fiber, where a strain sensitivity of –2.5 pm/με (roughly double of the silica FBG) was achieved. On the other hand, specialty fibers are also exploited in order to design an all-optical strain sensor to improve the sensitivity. Dong et al. in [101] reported a temperature insensitive strain sensor based on Sagnac interferometer that employed 86mm long polarization-maintaining photonic crystal fiber (PCF). Observed strain sensitivity was 0.23pm/με. In another attempt, a PCF Mach-Zehnder interferometer was realized inscribing pair of LPGs directly on a PCF [16]. A maximum strain sensitivity of –2.6pm/με was achieved. However, in comparison to FBG based strain sensors, PCF interferometers are not competitive due to several centimeters length of the PCF and a high splice loss between Hi-Bi PCF and standard fiber. In order to

increase the strain sensitivity, novel grating structures imprinted on a PCF were also exploited. For example, [102] also reported PCF based strain and temperature sensors, which were devised by fabricating long period gratings (LPGs) of different structural parameters in different types of PCF. Comparing the response characteristics of these different LPG-PCF based strain sensors, highest strain sensitivity observed was –7.6pm/με. However, performance of these sensors was limited by power losses due to CO_2 laser induced collapse of air holes, non-periodicity and disorder of the refractive index modulation. Also, the feasibility of distributed sensing as well as simultaneous multi-parameter sensing with such PCF based sensors are yet to be investigated; whereas FBG sensors have also shown the advantage of multi-parameter sensing with a short length single FBG [103]. Thus, in all the attempts to enhance the strain sensitivity of FBG sensors, a maximum sensitivity that was roughly double of the standard FBG was achieved or otherwise, the dynamic range was very limited. Employing LPG–PCF sensing structure, though resulted in a good sensitivity, but had its own inherent limitations.

Relative humidity (RH) is another vital parameter whose precise monitoring is critically important in various fields, such as, SHM, semiconductor manufacturing process, chemical/biochemical/food processing industries, air-conditioning to name a few [104]. There are many conventional humidity sensors reported in the literature, which are characterized with a good sensitivity. However, again, its optical fiber humidity sensors that have convincingly established themselves as an alternate to the traditional sensing schemes. Numerous attempts have been made to realize optical fiber RH sensors [105-110]. Predominantly, these sensors exploit evanescent wave absorption model employing straight and uniform/U-bent/tapered/side-polished fiber structure. Some of such attempts also employed an interferometric model.

Irrespective of the employed methodologies, nonlinearity in the response characteristics, limited dynamic range and piece-wise sensitivity variation remain the matter of great concern for almost all these reported optical fiber based humidity sensors barring a few. On the other hand, various attempts have also been made to realize in-fiber grating based RH sensors. In order to develop FBG based RH sensor, RH is preferably and strategically mapped in strain domain. This strain mapping is achieved as following: a suitable thermoplastic/polyimide material that is coated on the FBG swells in accordance when exposed to the humid vapours. This leads to a strain variation across FBG, which ultimately results in a wavelength modulation, exactly a signature of RH variations, in the response characteristics of FBG. As an example, Kronenberg et al. in [111], Yeo et al. in [112] and Huang et al. in [113] employed polyimide coated FBG structure for humidity detection. A linear response over a limited dynamic range with a sensitivity of ~3.4 pm/%RH is observed in [111]. Comparatively, researcher in [112] succeeded in improving the sensitivity to a maximum value of 5.6 pm/%RH for the observed dynamic range of 23-97%RH; whereas in [113], succeeded in extending the linear dynamic range to 11-98%RH at the expense of sensitivity. In contrast, water affinity of certain polymer facilitates swelling as well as an increase of the refractive-index (RI) of the material. Owing to these two effects, FBGs written in such polymer optical fibers (POF) are observed to be appreciably more sensitive to RH exposure. Exploiting these effects, Zhang et al. [114] have reported POFBG based RH sensor. In another attempt, Rajan et al. have reported etched POFBG based RH sensor [115]. Sensitivity improved as expected. However, response characteristic is observed to be nonlinear with dynamic range limited and sensitivity varying piece-wise across. On the other hand, being inherently sensitive to the ambient RI, structures such as long-period-gratings (LPGs) [116-119] and tilted FBGs [120] in conjugation with a suitable polymer (gelatin/hygrogel/SiO_2/TiO_2/PVA) sensing film are also

exploited to realize RH sensor. For LPG based RH sensors, highest dynamic range of 33–97%RH is observed in [116], but the sensor response was nonlinear throughout. For tilted FBG based RH sensor, a piecewise linear response in the RH range of 20-74% and 74-98% is observed. Recently, an RH sensor based on a polymer-infiltrated photonic crystal fiber interferometer has also been reported in [121]. A nonlinear response across the reported dynamic range is observed. Further, realization of a reversible and repeatable response with this scheme remains a challenge.

The main objective of the thesis is to develop FBG based novel all-optical sensors to monitor some of the most important parameters from the point of view of SHM such as, tilt, vibration, strain and RH. It's important to mention that for SHM and real-field applications, not only a reasonably good sensitivity is required; but the sensor is simultaneously desired to have an ability to capture the applied perturbations strategically very effectively and without any inherent instability. Relatively smaller discrepancy as well as uncertainty and a better angular resolution manifest a stable and effective sensing mechanism. Main objective while developing these sensors is to achieve manifold sensitivity enhancement, possibly with a tunable response characteristics and without any inherent measurement instabilities.

To achieve these objectives, first, a novel, all-optical, temperature insensitive, pendulum based but stable sensor design strategy with inherent enhanced tuning capability for its sensitivity is characterized. This sensor design, which employs FBGs, negates inherent design-defects related response limitations. Sensor exhibits a completely reversible linear response over a dynamic range of $\pm 10^{o}$. The most important feature of the reported sensor is its inherent enhanced tuning

capability for its sensitivity. An excellent sensitivity (~0.0626 nm/^{o}) that can further be nonlinearly tuned is established for this sensor. A much improved resolution (0.008^{o}), accuracy of tilt measurement (±0.36^{o}), maximum discrepancy (less than ±0.0231nm) and maximum angular uncertainty (~±0.34^{o}) are also established for this sensor. In order to capture the applied tilt perturbations strategically more effectively with enhanced stability in the sensor's response, another novel FBG based tilt sensor, employing a non-pendulum type design strategy is realized. Being non-pendulum type, there is no possibility of any inherent friction and the limiting effects at mechanical joints. This sensor exhibits a better resolution (better than 0.004°), a better accuracy (~±0.05°) and a lesser maximum discrepancy (~±0.001nm) during the forward as well as the reverse tilts. Sensor design also facilitates tuning of its sensitivity. Sensor response is characterized by a very high degree of reversibility and repeatability over the designed/observed dynamic range. In the next step, a simple design strategy of FBG based all-optical vibration sensor, employing a methodology to ensure chirp-free mechanism with a capability of resolving two-dimensional perturbations, is proposed and experimentally demonstrated. In this design, vibration of sensor displaces the seismic mass fixed between two flexural beams, thus inducing a variable strain in the two beams. This strain variation results in a Bragg wavelength shift for corresponding FBGs attached to the beams. Sensor was characterized with a series of applied perturbations. An excellent capability of resolving externally applied signals having frequency in 10Hz to 350Hz and the acceleration in 0.65 to 70m/sec^{2} range is observed. As mentioned earlier, FBG based sensors will receive a tremendous boost if its inherent strain sensitivity could be enhanced to a very large value. In order to achieve this, a single FBG sensor with corrugated cladding structure across the FBG carrying core is designed and experimentally investigated for strain sensitivity enhancement. The corrugated structure across the FBG section of the fiber splits

a single FBG into multiple & independent FBGs, each suitable for independently sensing an applied perturbation. A manifold enhancement of the strain sensitivity (over ten times relative enhancement of strain sensitivity) is observed, which is impossible to realize with a normal FBG. Finally, in the last part of research, a fiber Bragg grating based humidity sensor is developed employing a novel mechanism of effective-index modulation with an ambition to achieve widest possible dynamic range and optimum sensitivity. To achieve these objectives, fiber diameter in the grating region is reduced to a lowest possible working limit (~ a few microns) using appropriately controlled chemical etching. A wide linear dynamic range ~3 – 94 %RH with good sensitivity of ~0.082 pm/%RH is realized. The response of the developed sensor is observed to be completely reversible with an appreciably stable characteristic during repeatability tests.

Chapter-2 of the present thesis focuses on the rigorous research & development of a novel and simple FBG based tilt sensor having inherent enhanced tuning capability for its sensitivity. Pendulum based design strategy employed here overcomes inherent design-defects related limitations substantially. Preliminary result is reported in [127]. It's worth mentioning that resolution, accuracy, maximum as well as average discrepancies and maximum angular uncertainties along with repeatability/reliability are critically important features of a sensor in addition to its sensitivity. Rigorous experimental investigations were carried out in order to establish these parameters for the sensor. For a given sensor's geometrical parameters, sensor was characterized for cyclic tilt variations (forward and reverse tilts in positive as well as negative directions) in the *y*-*z* plane first. Afterwards, sensor was characterized for cyclic tilt variations in *x*-*z* plane. In order to investigate various critically important parameters explained earlier, a number of such cyclic experiments were performed for *y*-*z* as well as *x*-*z* plane on

different days at an interval of one week each. Throughout these experiments, individual FBG's response is examined. Sensor is observed to be capable of measuring the magnitude as well as the direction of inclination from the horizontal with a complete reversible and linear response over the designed dynamic range of ±45^o. It also exhibits inherent enhanced tuning capability towards sensitivity by varying only one sensor parameter, namely, the mass of the employed bob. An excellent sensitivity of the order of ~0.0123 nm/^{o} with a small mass and ~0.0626 nm/^{o} with a larger mass that can further be tuned is established for the sensor. Importantly, a maximum discrepancy across all the experimental results obtained with the sensor employing smaller mass is observed to be less than ±0.0069nm with corresponding maximum angular uncertainty of ±0.5609^o for both forward as well as reverse directions of applied tilts. Average discrepancy, resolution and accuracy of tilt measurement are observed to be less than ±0.0008nm, 0.0407^o and ~±0.56^o respectively. For the mass that results in a better sensitivity, a much improved resolution of 0.008^o, an accuracy of tilt measurement of ±0.36^o, maximum discrepancy less than ±0.0231nm and maximum angular uncertainty of ~±0.34^o are observed for this sensor. Further, temperature cross-sensitivity in completely negated by measuring tilt information as a function of difference in the wavelength shifts of two FBGs.

The objective of the research reported in Chapter-3 is to develop a design strategy that negates internal instabilities along with constraints imposed by inherent rotational/mechanical frictions in better ways while enabling tilt measurement in optical domain. A very simple, non-pendulum type design strategy, which is theoretically capable of monitoring tilt/inclination from horizontal in a dynamic range of ±45^o, is employed in order to develop an all-optical FBG based tilt sensor. Employing non-pendulum type design strategy to map tilt in strain domain negates the

possibility of any inherent friction and the limiting effects within mechanical structures. Sensor is observed to be capable of resolving magnitude as well as the direction of inclination from horizontal strategically more effectively and without any inherent instability. This is reflected in a relatively better resolution (better than 0.004º), a better accuracy (~±0.05º) and least maximum discrepancy (~±0.001 nm) during the forward as well as the reverse tilt. Sensitivity of the proposed sensor, theoretically proportional to the half of the mass employed in the sensor design, is observed to be 0.012 nm/º with a comparatively smaller mass. It is observed that a far better sensitivity, in comparison to the highest sensitivity reported in the literature, can be achieved by suitably employing an equivalent mass in the proposed design. Importantly, sensor response is characterized with a very high degree of reversibility and repeatability over the designed/observed dynamic range.

The objective of the research reported in Chapter-4 is to design and construct a simple, compact, FBG grating based two-dimensional temperature insensitive vibration sensor by employing chirp free strain tuning mechanism. The sensor design utilized in this work makes use of a concentrated mass element rigidly fixed between two thin parallel plates to which the FBG is fixed. Performance characteristics for the design strategy of proposed sensor is first theoretically investigated using a 3-D CAD model and ANSYS software. Afterwards, in order to carry out experimental investigations, sensor is excited with an electromechanical shaker by applying pure sine wave signals with varying frequencies (from 10Hz to 350Hz) and amplitudes (from 0.65 to 70m/sec^2). Sensor depicts a great capability of successfully resolving magnitude as well as the direction of applied vibration perturbations with any frequency and amplitude combinations.

Further, temperature cross-sensitivity in completely negated by measuring vibration information as a function of difference in the wavelength shifts of two FBGs.

In Chapter-5, a novel design strategy in terms of corrugated cladding structure over a FBG carrying core is proposed and experimentally investigated, predominantly from the point of view of strain sensitivity enhancement and a possibility of deriving multiple independent sensors from a single FBG. A comparative analysis is also carried out employing different sensing structures on a single FBG. Proposed sensor with corrugated cladding structure over a single FBG acts as three separate and independent sensors. The most striking feature of this sensing structure is a remarkably high strain sensitivity enhancement. Strain sensitivity of one of the etched section of corrugated structure is observed to be over 10.5 times in comparison to the strain sensitivity of unetched section of the corrugated FBG structure. Further, experimental results show that a good strain measurement accuracy of ±2.15με, low maximum discrepancy of ±0.019nm and a strain resolution better than 5.7nε are achieved. In addition, sensor exhibits a very good degree of reversibility and repeatability.

Chapter-6 of the present thesis is devoted to the development of a temperature independent FBG based RH sensor employing novel sensing mechanism to achieve a throughout linear response over a wide dynamic RH range and an optimum sensitivity. Effective-index modulation induced Bragg wavelength shift scheme, rather than strain induced Bragg wavelength shift scheme is employed for the first time to design this sensor. FBG structure is suitably modified, and detailed theoretical investigations are carried out for the proposed sensor to establish its characteristics. Afterwards, sensor is experimentally investigated by exposing it to the repeat cycles of

increasing and decreasing RH variations over a sufficiently long time period. In order to establish various sensor characteristics, experiments are repeated multiple times over a gap of a week in between. A linear response over a dynamic range as wide as ~3 – 94% RH with a good sensitivity of ~0.0825 pm/%RH during increasing as well as decreasing humidity is observed/established. Repeatability and reliability tests are also carried out number of times again with a gap of a week in between to rigorously analyze the sensor performance. A maximum variation in the sensor output across all the experimental data sets for all RH values is observed to be of the order of 10^{-4} nm. Further, response time of FBG based sensor was observed to be more than ten times faster than the commercial sensor.

Chapter-7 of this thesis presents a broad summary of all the research work carried out and reported in this thesis as well as highlights the future scope of the research.

Above work has resulted in following publications:

(A) **IN INTERNATIONAL JOURNALS**

1. Pathi Munendhar, R. Aneesh, and Sunil K. Khijwania, "Development of an All-optical Temperature Insensitive Nonpendulum-type Tilt Sensor Employing Fiber Bragg Gratings", **Applied Optics,** 53, 3574-3580(2014).

2. R. Aneesh, Meeth Maharana, Pathi Munendhar, H. Y. Tam and Sunil K. Khijwania, "Simple Temperature Insensitive Fiber Bragg Grating based Tilt Sensor with Enhanced Tunability", **Applied Optics,** 50, E172-176(2011).

3. Pathi Munendhar, Shaival Buch and Sunil K. Khijwania, "A Novel Fiber Bragg Grating Structure with Enhanced Strain Sensitivity", (communicated), 2014.

4. Pathi Munendhar, H. Y. Tam and Sunil K. Khijwania, "Temperature Insensitive Fiber Bragg Grating Based Two Dimensional Vibration sensor for Structural Health Monitoring", (communicated), 2014.

5. Pathi Munendhar and Sunil K. Khijwania, "Fiber Bragg Grating Based Humidity Sensor Employing Effective Refractive Index Modulation Technique", (communicated), 2014.

(B) **IN INTERNATIONALCONFERENCES**

6. Pathi Munendhar and Sunil K. Khijwania, "Fiber Bragg Grating Based Humidity Sensor with Wide Linear Dynamic Range" **SPIE OPTICS+PHOTONICS-2014**, San Diego, United States, 17-21 August (2014), (Accepted).

7. Pathi Munendhar and Sunil K. Khijwania, "Fiber Bragg Grating Based Humidity sensor". International Conference on Optoelectronics "**ICOL-2014**", Dehradun, India, 05-08 March, (2014).

8. Pathi Munendhar and Sunil K. Khijwania, "Fiber Bragg Grating Based Two Dimensional Vibration sensor for Structural Health Monitoring". International Conference on Recent Trends in Applied Physics & Material Science "**RAM 2013**", Bikaner, India, 01-02 February, 2013. AIP Conf. Proc. 1536, 1324 (2013).

9. Pathi Munendhar, Shaival Buch, R. Aneesh and Sunil K. Khijwania, "A Novel Fiber Bragg Grating Structure for Multi-parameter Sensing with Enhanced Strain Sensitivity"

International Conference on \Recent Trends in Applied Physics & Material Science "**RAM 2013**", Bikaner, India, 01-02 February, 2013. AIP Conf. Proc. 1536, 1327 (2013).

10. Pathi Munendhar, R. Aneesh and Sunil K. Khijwania, "Development of an All-optical Tilt Sensor Employing Fiber Bragg Gratings" International Conference on Fiber Optics and Photonics "**PHOTONICS 12**", Chennai, India, 09-12 December, (2012).

Chapter 2

Simple Temperature Insensitive Fiber Bragg Grating Based Tilt Sensor: Tunable Sensitivity Enhancement

2.1 Introduction

Inclination or tilt-angle monitoring is of extreme importance for the health of various civil infrastructures such as tunnel, bridges, dams, etc. In addition, it is also one of the key parameters to be monitored in mechanical, instrumentation, robotics, aeronautical engineering applications. Hence, a very accurate, highly sensitive, compact tilt monitoring sensor-system capable of resolving lowest possible tilt with a large dynamic range would be of extreme importance. Most of the conventional tilt sensors are electronic in nature and transform inclination information into electric signals either through magnetic effects or through capacitive effects [56, 58]. However, their inherent limitations such as vulnerability towards electromagnetic/radio-frequency interference (EMI/RFI) and inability towards multiplexing and remote sensing pose serious problem and make them unthinkable for real applications. Optical sensors overcome some of the shortcomings of conventional sensors. A few attempts have been made to realize all-optical tilt sensors employing laser based sensing technology. For example, Zhong et al. have reported an optical tilt sensor based on wavefront sensing [59]. In another work, Hua et. al. in [62] have reported tilt sensor based on laser interference; whereas Xiaoyong et al. in [63] have reported another tilt sensor based on laser and holographic technique. However, being bulky and complicated in design configuration, and extremely alignment sensitive, all these methodologies are in fact impractical for real field applications. Relying on a very high sensitivity of the optical signal propagating inside an optical fiber to the external perturbations, optical fiber sensors have emerged as a strong

alternate to the conventional/bulk optics sensors with a capability to address all the inherent limitations of these sensors and have been remarkably developed over the years since the first fiber optic sensor (FOS) was reported in 1974 [122]. Optical fiber sensors with additional inherent advantages such as remote & distributed sensing, multiplexing capabilities, small volume, light weight, potentially resistant to ionizing radiation etc., have found wide range of real field applications including but not limited to environmental monitoring, bio/chemical diagnosis and structural health monitoring to name a few [123]. Nevertheless, only a few attempts have been reported in the literature towards the development of optical fiber sensors for inclination/tilt-angle monitoring. As an example, Yuan [64] has reported a push-pull fiber optic tilt sensor based on Mach-Zehnder reflector. Lee et al. [65] have reported another tilt sensor which employed optical fibers as mere transceivers to capture reflected light upon applying tilt. In another such attempt, Bajic et al. [66] have reported tilt sensor employing lead-in and lead-out optical fibers separated by a suitable distance in a liquid container. Upon rotation, liquid surface reorients itself, leading to a variation in the captured optical power by the lead-out fiber. Though, reported sensors exhibit a good capability in capturing the applied tilt, observed sensitivity and tilt-angle resolution along with inherent measurement errors associated with complicated design strategies were critical limitations in such attempts. A major thrust to all-optical sensing technology is witnessed with the invention of in-fiber Bragg grating (FBG) [34]. Today, FBG sensors have become an integral part of many engineering systems including structural-health-monitoring (SHM), mechanical, aeronautical, communication applications to name a few. FBG sensors are based on wavelength modulation that results from strain-optic/thermo-optic effects. This makes them an inherent sensor for the strain and temperature both. One needs to device a smart mechanism to decouple strain or temperature information. Various techniques/designs have been successfully employed in order to abandon the effect of one parameter on the measurement,

especially the temperature. Being inherently self-referencing with the capability of multiplexing a large number of FBGs [35], they immediately found numerous applications over other types of optical fiber sensors and attracted lots of research efforts worldwide. Recently, a few FBG based attempts have been made for inclination/tilt measurement [45, 67-72]. Though a very high resolution was achieved [67], the performance in these studies was limited by the design constraints such as a cantilever based pendulum suspension mechanism resulting in friction and corresponding instabilities in [68-70] and pre-deflections of steel flakes with a complicated pendulum suspension mechanism in [69]. All these designs relied on the rotation of the pendulum while applying the tilt and hence suffered from the unwanted and inherent mechanical frictions of the joints during the rotation. In [70], a design strategy based on single FBG was proposed. Nevertheless, the sensitivity in all the reported sensors was limited. He et al. in [71] reported a tilt sensor based on three FBGs in series on a single fiber making an inverted pyramidal structure with three fiber arms and a mass (bob) suspended from the vertex. A very high-sensitivity was observed. However, retrieval of the tilt was based on a very intricate mathematical analysis. Ni et al. [72] reported another tilt sensor based on four FBGs in series on a single fiber making an inverted pyramidal structure with four fiber arms and a mass (bob) suspended from the vertex. Nevertheless, stability of the sensor and the cross-sensitivity to unwanted perturbations in both the designs are important issues. As the mass is hanged directly to the fiber loop, any unwanted add-on oscillation is expected to lead to a random vibration/oscillation of the fiber-mass pendulum system of both the sensor designs in [71, 72]. This is bound to give measurement errors and will make these sensors highly unstable. Also, there is a possibility of slacking of one fiber arm in the plane of inclination during the tilt. Au et al. [45] reported another tilt sensor based on four FBGs in the horizontal plane with a response linearly tunable in proportion of the mass of the used bob.

This chapter focuses on the rigorous research & development of a novel and simple FBG based tilt sensor having inherent enhanced tuning capability for its sensitivity. Pendulum based design strategy employed here overcomes inherent design-defects related limitations substantially, and intrinsically negates the possibility of noise/error due to any add-on unwanted perturbations. Theoretically, proposed sensor is capable of monitoring tilt/inclination from horizontal in a dynamic range of ±45^o. It's worth mentioning that resolution, accuracy, maximum as well as average discrepancies and maximum angular uncertainties along with repeatability/reliability are critically important features of a sensor in addition to its sensitivity. Rigorous experimental investigations are carried out in order to establish these parameters for the sensor. Enhanced (nonlinear) tunability is achieved by varying just one sensor parameter, namely the mass of the bob. Sensing strategy is based on decoding the inclination/tilt angle information from the peak wavelength separation between two FBGs. This makes the diagnosing procedure completely temperature independent. Experimental results show that a tilt angle resolution better than 0.0008^o, tilt accuracy of ~±0.34^o, maximum discrepancy less than ±0.0231nm, maximum angular uncertainty of ~±0.34^o and the sensitivity of the order of ~0.0626 nm/^{o} was achieved.

2.2 Experimental

2.2.1 Sensor Design and Construction

The design strategy of the sensor is as follows; two square aluminum plates of dimension 5×5×1 cm^3 were joined by four identical vertical brass rods of diameter 0.6cm (Fig.2.1). A rectangular prism of dimension 1.7×0.8×1cm^3 was removed from the center of the four edges of the top plate. These removed rectangular prisms were replaced by four specially designed small units, termed as strain tuning units (STUs) (see encircled part of Fig.2.1 for schematic

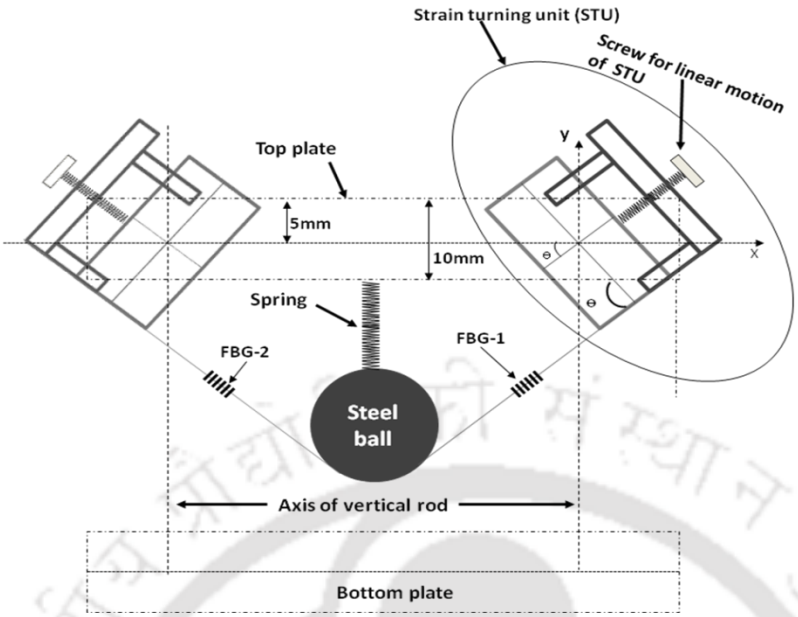

Figure 2.1: *Schematic diagram of pre-straining FBGs using STU.*

of STU). Each STU consists of two parts, namely A and B (Fig.2.2). Part-A, termed as the base plate, is an aluminum rectangular prism of dimension 1.59×0.8×1 cm^3 with a steel axle

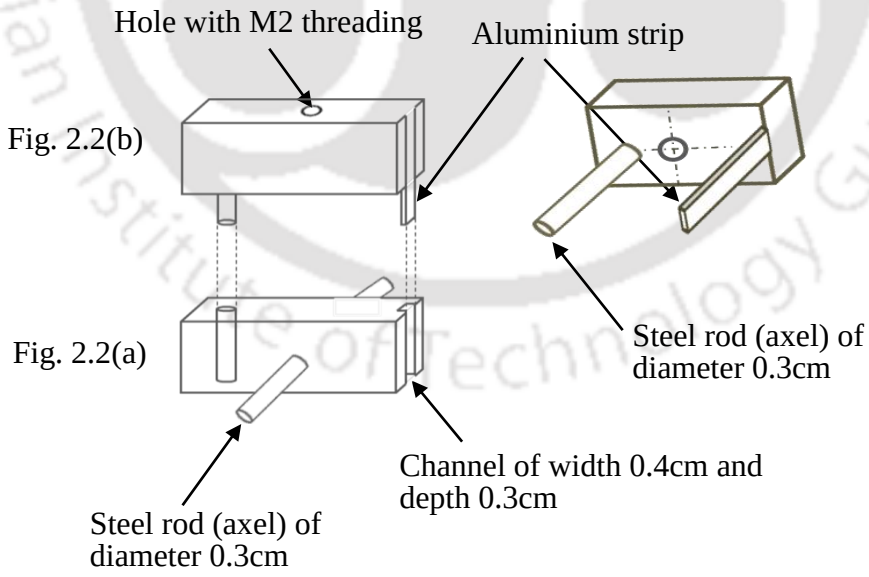

Figure 2.2: *(a) Part A of STU; (b) Part B of STU with two side image.*

through the centre of the two opposite vertical faces of the prism. On one side of this prism, a vertical channel of width 0.4cm and depth 0.3cm was made. Close to the opposite side of this prism (0.35cm from the edge), a hole of diameter 0.3cm was drilled (Fig 2.2(a)).Part B is an aluminum rectangular prism of dimension 1.7×0.8×1 cm^3. It has an aluminum strip of dimension 1×0.4×0.3 cm^3 on one side. Close to the opposite side of this prism (at distance

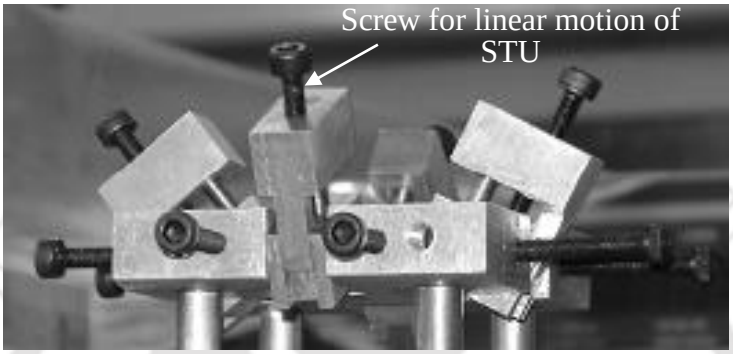

Figure 2.3: *Linear motion of Part-A of STU against Part B using M2 screw.*

0.46cm), a steel rod of diameter 0.3cm was fixed (Fig 2.2(b)). At the center of this prism, a hole (H) having M2 threading was made and a M2 screw was fixed in it. Part B was fixed onto Part A. While turning the M2 screw, Part B moved linearly against the base plate

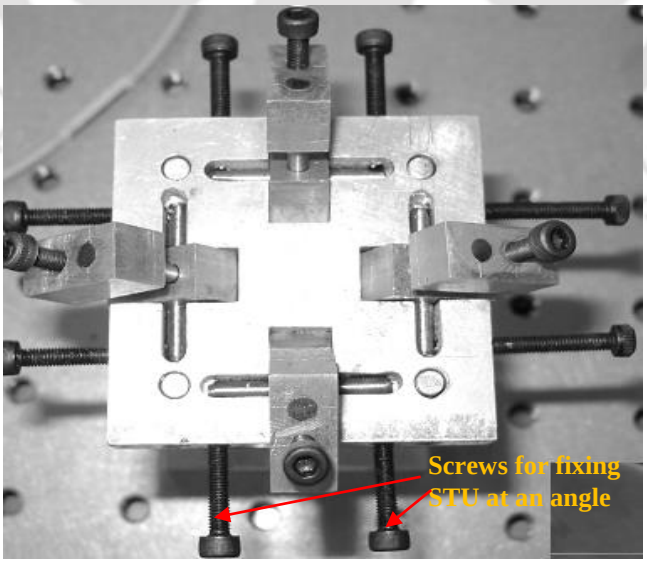

Figure 2.4: *Top plate with STUs fixed on it.*

irrespective of the base plate's orientation (Fig.2.3). Axel of Part A was fixed at the middle of the width of the top plate (Fig. 2.4). Part A, and hence STU, was free to rotate within 0-90°. Nevertheless, it was kept static at a given orientation with the help of two adjusting screws (Fig. 2.4). Thus, each STU were capable of moving linearly at a predetermined angle and thus provided fine strain tuning mechanism. From the center of the top plate, a steel bob was hanged through a spring of optimized spring constant. Four FBGs were written onto a single fiber such that the distance between FBG1 (λ_1) and FBG2 (λ_2) as well as FBG3 (λ_3) and FBG4 (λ_4) were kept identical. The fiber carrying four FBGs was glued at the center of first STU, then to the bottom of the bob, then to the opposite, i.e., third STU; then to the second STU and via the bottom of the bob to the opposite, i.e., fourth STU; thus making two crossing triangular/inclined fiber arms each having curved vertex at the bottom of the bob. In this arrangement, FBGs rested at the middle of the fiber joining STU and the bottom of the bob. Spring was maintained to its natural length by pre-straining each fiber arms equally along the crossed and inclined directions through STUs. The center of the gravity (CG) of the bob was ensured to be at the vertical line (longitudinal axis) joining the center of the top and the bottom plates. It is important to mention that the role of the spring was to give the stability to the proposed sensor. In the absence of the spring, bob is bound to rotate with respect to its bottom point where fibers are glued while applying tilt (say in *x*-*z* plane). This will lead to the slackening of the fiber arms and the random strain distribution. Further, its CG will also get displaced from the longitudinal axis of the sensor. Owing to this, the angle θ made by FBG1 and FBG2 from the top plate (Fig. 2.1) will no longer remain the same and will change to two different angles, say α and β. These angles will vary slightly with the inclination angle in different ratios. Same would be the case in the *y*-*z* plane, another two different angles, say α' and β', will be induced and vary with the inclination angle. In an ideal situation, deviation from θ to these angles should be very small and negligible. Further,

sensor performance critically depends on the spring's characteristics. Springs of various spring constant were considered in optimizing the sensor performance. Spring with low spring constant resulted in the deformation of the four fiber arms carrying FBGs while applying tilt.

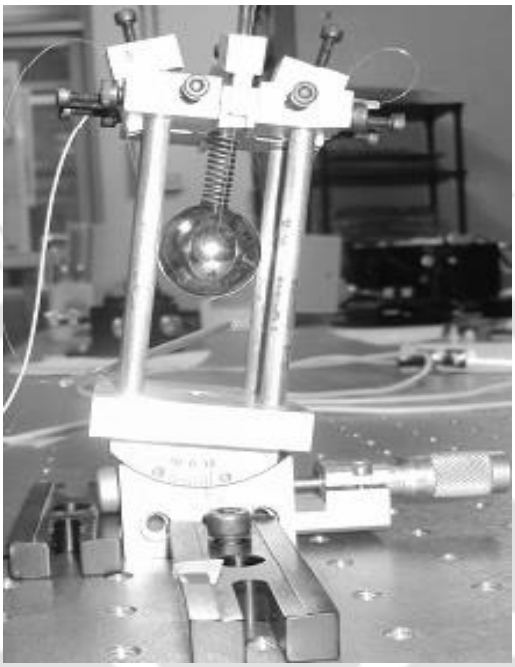

Figure 2.5: *Proposed FBG based tilt sensor.*

With such springs, it was difficult to keep the CG of the bob in the longitudinal axis of the sensor, to avoid rotation of the bob and to avoid slackening of fiber arms during the application of the tilt. Further, sensor with such spring (low spring constant) was observed to be unstable with the spring-mass-fiber system vibrating in response to any unwanted add-on perturbation and thus modulating the sensor characteristics with unwanted noise. Increasing the spring constant resulted in a better stability and less deformation of the sensor. Spring with a particular higher value of the spring constant that almost negated the deformation (rotation of the bob, deviation of CG from the sensor's longitudinal axis, slackening of fiber arms etc.) was used in the final sensor design. Total dimension of the sensor was $5\times5\times8$ cm^3. Photograph of the developed sensor is shown in Fig. 2.5.

2.2.2 Sensing principle

When the sensor is inclined by an angle ϕ, say, in the *y-z* plane keeping inclination in *x-z* plane zero, the strain in the gratings gets redistributed and the corresponding wavelength shift difference is given by

$$\Delta(\lambda_2 - \lambda_1) = \frac{(1-P_e)mg\,\lambda_1 \sin\phi}{AE\cos\theta} \tag{2.1}$$

and

$$\Delta(\lambda_4 - \lambda_3) = 0 \tag{2.2}$$

In the same way, when the sensor is inclined by an angle ϕ, say, in the *x-z* plane keeping inclination in *y-z* plane zero, the strain in the gratings gets redistributed and the corresponding wavelength shift difference is given by

$$\Delta(\lambda_4 - \lambda_3) = \frac{(1-P_e)mg\,\lambda_3 \sin\phi}{AE\cos\theta} \tag{2.3}$$

and

$$\Delta(\lambda_2 - \lambda_1) = 0 \tag{2.4}$$

Here *'m'* is the mass of the bob, '*g'* is the acceleration due to gravity, *'P_e'* is the photoelastic constant of the fiber, *'A'* is the area of cross-section of the fiber, *'E'* is the Young's modulus of the material of the fiber and θ is the angle made by the fiber arms from the horizontal. Equations (2.1) and (2.3) show that the wavelength separations are linearly proportional to $\sin\phi$. Further, as the temperature-change during the experiment shifts each FBG's wavelength in the same direction, measuring the tilt angle through wavelength separation between the two FBGs in a given fiber arm overcomes the problem of temperature cross-talk in the final measurement; thus making the sensor temperature independent. The most striking feature of the proposed sensor is its inherent enhanced (nonlinear) tuning capability for its sensitivity. This can be understood by analyzing equations (2.1) and (2.3). As can be observed, instead of

one, there are two factors influencing the sensitivity, namely m and $\cos\theta$. As m increases, size of the bob and hence θ increases. The increase of θ leads to a nonlinear increase of $1/\cos\theta$. Thus, the linear increase in m and nonlinear increase in $1/\cos\theta$ multiplying together leads to a manifold increase in the sensor's sensitivity. It's worth mentioning that this enhanced sensitivity tuning is realized by changing only one parameter, namely the mass of the bob m. This is in contrast to [45, 71, 72], where an increase in mass has resulted in a linearly proportional increase in the sensitivity. One needs to change other sensor parameters, e.g., fiber length or the dimension of the top plate in [71, 72].

2.2.3 Sensor characterization

Four FBGs were written onto a hydrogen-loaded single mode fiber using phase-mask method. The parameters of the fiber used are E =7.27×10^{10} N/m^2, A = 1.2266×10^{-8} m^2 and P_e = 0.22. Also, the peak reflection wavelengths of FBGs are 1544.56nm (λ_1), 1536.75nm (λ_2), 1559.34nm (λ_3), and 1571.05nm (λ_4). The fiber was glued at two opposite STUs through the bottom of the bob (having mass 67g in one experiment and 110.3g in other experiment) as explained in the previous section. The one end of the fiber carrying four FBGs was connected to FBG interrogator (Micron Optics, si425, resolution 0.5 pm). The four FBGs are rested at the center of each arm. Next, these gratings were pre-strained by a pre-determined value of 1750 με through the STUs. The spring maintained its natural length with the center of the bob passing through the line joining the center of the top and bottom square plates. The sensor was mounted on the available tilt stage (goniometer), which had a provision to turn the sensor within ±10^o range only. This was the laboratory constraints. It is important to mention that the sensor is not limited to a maximum tilt of ±10^o, rather it is designed for a ±45^o applied tilt. To carry out the experiment, the sensor was first tilted in y-z plane and the wavelength shifts

for four FBGs corresponding to different values of tilt angle (ϕ) were recorded using the interrogator. The tilt angle was varied from -10^o to 10^o (forward) and then back to -10^o (reverse) in a suitable minimum steps allowed by the goniometer.

2.3 Results and Discussions

Elementary result is reported in [25]. In order to rigorously investigate the response characteristics of the proposed FBG based tilt sensor employing bob of mass 67g (mass-1), sensor was mounted on the available tilt stage (goniometer). Sensor was then tilted first in the *y-z* plane (plane carrying FBG1 and FBG2) in a suitable minimum amount of steps as allowed by the goniometer from 0^o–10^o (forward tilt) and then from 10^o–0^o (reverse tilt) in positive direction. Afterwards, sensor was tilted from 0^o–(-10^o) (reverse tilt) and then from (-10^o)–0^o (forward tilt) in negative direction. Wavelength of all the individual FBG (FBG1 and FBG2 in the plane of inclination, whereas FBG3 and FBG4 in a plane perpendicular to that of the inclination) during the entire experiment was recorded through the interrogator. Experiment was repeated afterwards by applying tilt variations to the sensor in *x-z* plane (plane carrying FBG3 and FBG4). In order to investigate the repeatability and reliability of the sensor, a total of three such cyclic experiments for *y-z* plane as well as *x-z* plane were performed on three different days at an interval of one week each. Figure 2.6 depicts, as an example, wavelength response of individual FBG employed in the sensor during the forward (-10^o to +10^o) as well as reverse (+10^o to -10^o) applied tilt cycles in *y-z* plane for all the three sets of the experiment. Following observations can be made from this response: (a) wavelength response of all individual FBG is linear during increasing as well as decreasing inclinations for all cyclic tilt variations; (b) a linear response for FBG1 and FBG2 indicates that these FBGs strategically share change of the center of gravity of the bob (mass) equally during the applied tilt; (c) wavelength response for FBG3 and FBG4 indicates that strain

remains invariant in these FBG arms; (d) analyzing the response characteristics in all the three sets indicates a highly repeatable and reliable nature of the sensor.

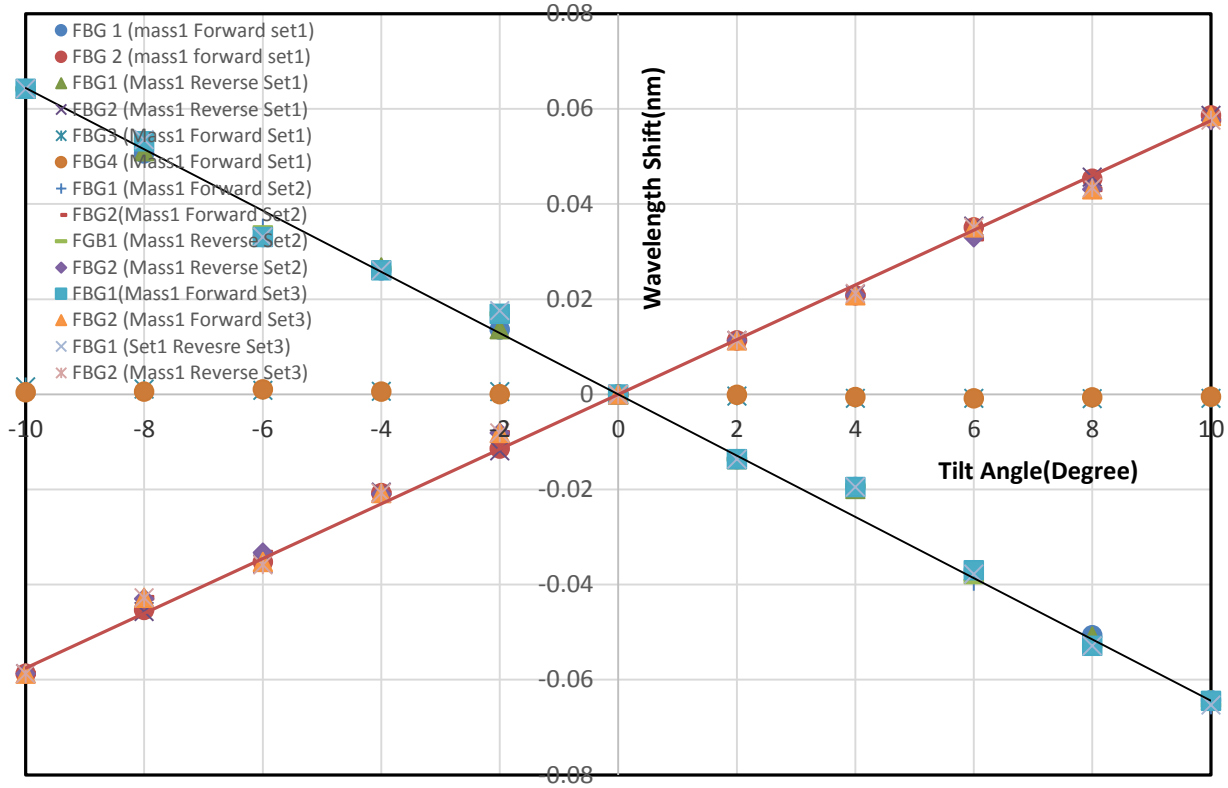

Figure 2.6: *Individual response of each FBG versus applied forward and reverse tilts for the three sets of the experiments with the proposed sensor employing mass-1.*

In order to find actual response characteristics of the sensor, experimentally observed wavelength differences, $\Delta(\lambda_2-\lambda_1)$ and $\Delta(\lambda_4-\lambda_3)$, for 0^o–10^o (forward tilt) and 10^o–0^o (reverse tilt) for the positive direction in *y-z* plane are shown in Fig. 2.7 (tilted squares and circles for forward whereas squares and triangles for reverse tilt). As can be observed from Fig. 2.7, the sensor response ($\Delta(\lambda_4-\lambda_3)$) for the orthogonal direction is observed to be zero as expected from Eq. (2.2). On the other hand, sensor response ($\Delta(\lambda_2-\lambda_1)$) is observed to be linear for the forward as well as the reverse tilt variations as predicted by Eq. 2.1. Measured linear sensitivities for forward (0^o-10^o) and reverse (10^o-0^o) directions are found to be 0.0122nm/^{o}

and 0.0123nm/^{o}, respectively. On the other hand, Fig. 2.8 depicts wavelength differences, $\Delta(\lambda_2-\lambda_1)$ and $\Delta(\lambda_4-\lambda_3)$, for 0^o–(-10^o) (reverse tilt) and $(-10^o$–$0^o)$ (forward tilt) for the negative direction in the same (*y-z*) plane. Following observations can be made from Fig. 2.8: (a) response in orthogonal plane, i.e., $\Delta(\lambda_4-\lambda_3)$ is again found to be zero as predicted by Eq. (2.2); (b) sensor response, $\Delta(\lambda_1-\lambda_2)$, is linear again in the 0^o-(-10^o) and (-10^o)-0^o tilt angle variations; (c) measured linear sensitivities for forward and reverse directions are once again found to be 0.0122nm/^{o} and 0.0123nm/^{o}, respectively. Linear response with identical sensitivity during the complete cycle of applied tilt (0^o-10^o-0^o and then 0^o-(-10^o)-0^o) manifests a highly reversible nature of the sensor.

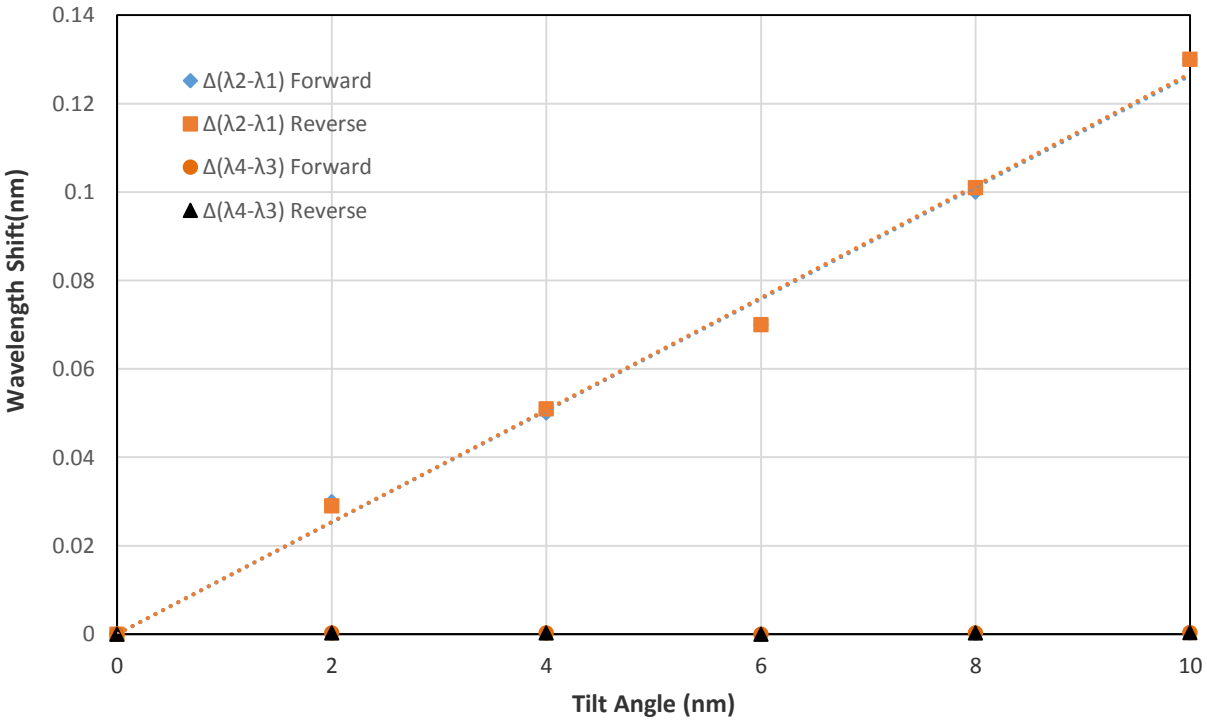

Figure 2.7: *Variation of $\Delta(\lambda_2-\lambda_1)$ for the +ve forward & reverse tilt in the y-z plane where the sensor employed lesser mass. $\Delta(\lambda_4-\lambda_3)$ shows the cross axis response.*

Identical response was observed when the tilt angle in the *x-z* plane was varied from 0° to 10° to 0° and then from 0° to -10° to 0°. In order to analyze the sensor performance critically,

sensor's response during the forward and reverse tilt variations in all the three sets were considered. A maximum discrepancy across all the experimental sets (for both the planes, *y-z* and *x-z*) is observed to be less than ±0.0069nm with corresponding maximum angular uncertainty of ±0.5609º for both forward as well as reverse directions of applied tilt. Average discrepancy is observed to be less than ±0.0008nm. The resolution of the sensor completely depends on the resolution of the interrogating device. The wavelength resolution of 0.5 pm of the interrogator resulted in the angular resolution of 0.0407º for the sensor. The accuracy of tilt angle measurement is observed to be ±0.56º.

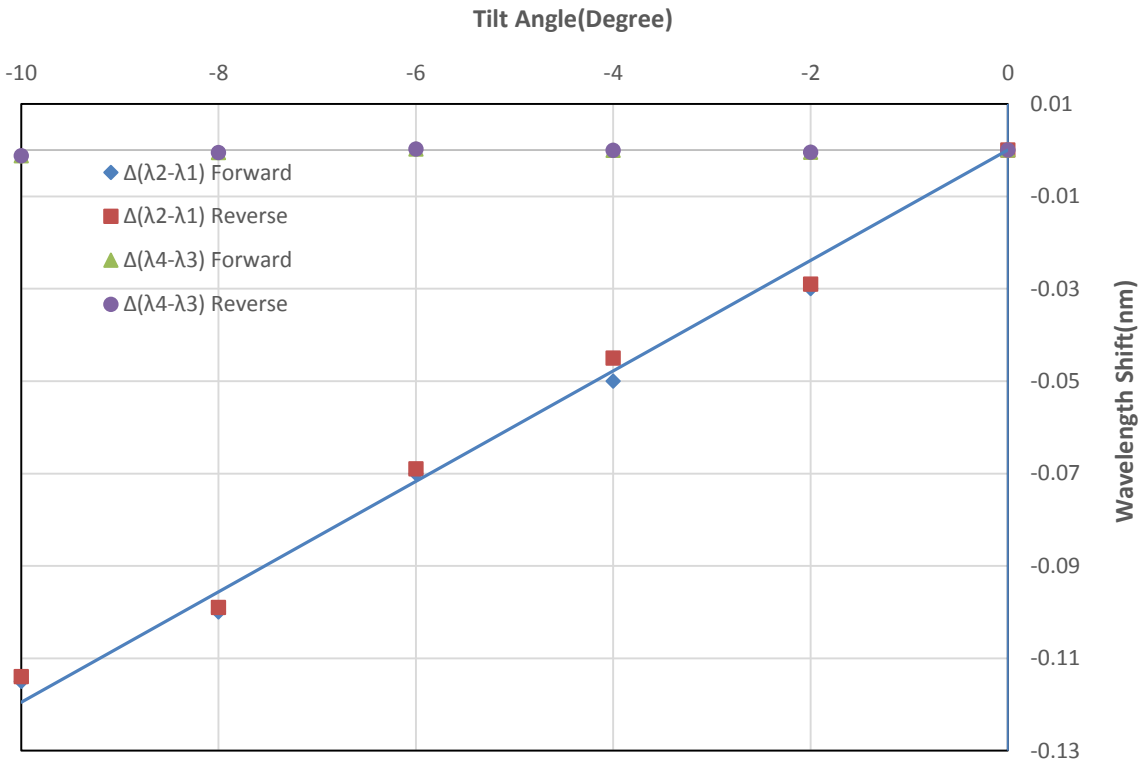

Figure 2.8: *Variation of $\Delta(\lambda_2-\lambda_1)$ for the -ve forward & reverse tilt in the y-z plane where the sensor employed lesser mass. $\Delta(\lambda_4-\lambda_3)$ shows the cross axis response.*

As can be observed from the design principal of the sensor [Eq. (2.1) or (2.3)], sensitivity can be increased manifold by simply increasing the mass of the bob. Hence, in the next step, in order to see the effect of mass on sensor performance, another senor was developed by

replacing the existing bob of mass 67g by another bob of mass 110.3g. Same sets of experiment, mentioned for the sensor comprising lesser mass, were repeated for the sensor comprising the new bob of higher mass (mass-2). Figure 2.9 depicts, as an example, wavelength response of individual FBG employed in the sensor during the forward (-10º to +10º) as well as reverse (+10º to -10º) applied tilt cycles in *y-z* plane for all the three sets of

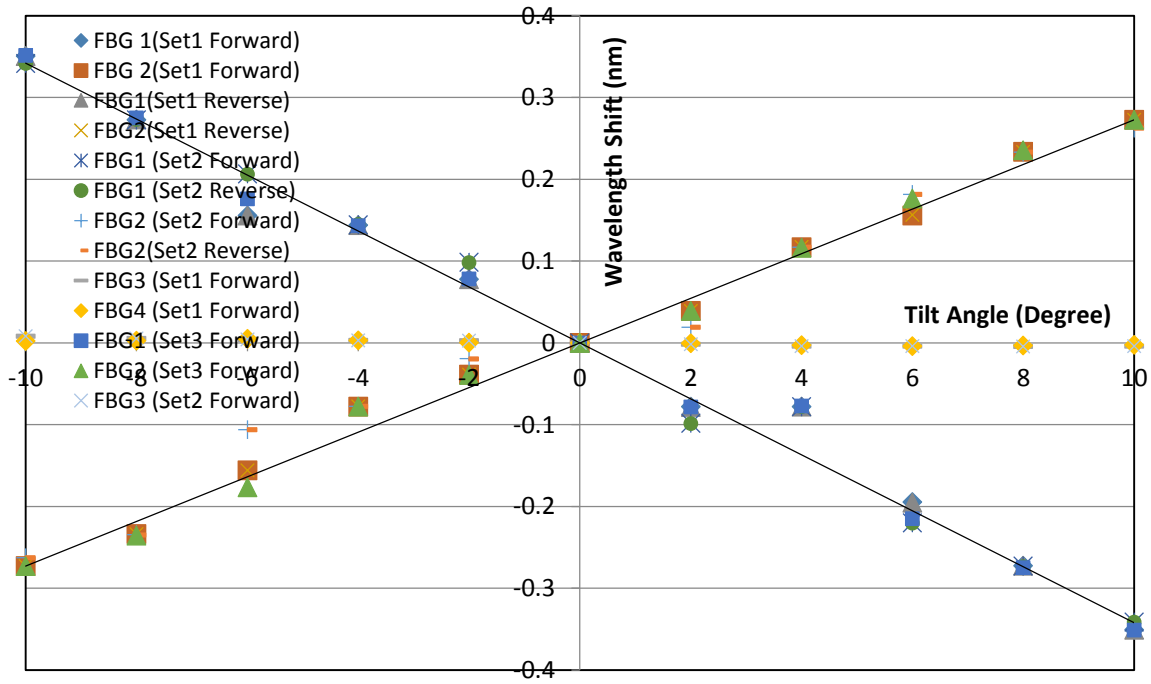

Figure 2.9: *Individual response of each FBG versus applied forward and reverse tilts for the three sets of the experiments with the proposed sensor employing mass-2.*

the experiment. For the sensor comprising higher mass, once again wavelength response of all individual FBG is observed to be linear during increasing/decreasing inclinations indicating FBG1 and FBG2 strategically sharing change of the center of gravity of the bob (mass) equally whereas FBG3 and FBG4 observing strain invariance during the applied tilt. Careful analysis of the response characteristics in all the three sets once again indicates a highly repeatable and reliable nature of the sensor. In order to find actual response characteristics of the sensor, experimentally observed wavelength differences, $\Delta(\lambda_2-\lambda_1)$ and

$\Delta(\lambda_4-\lambda_3)$, for 0^o–10^o (forward tilt) and 10^o–0^o (reverse tilt) for the positive direction in *y-z* plane are once again plotted in Fig. 2.10 (squares and tilted squares for forward whereas circles and triangles for reverse tilt). As can be observed from Fig. 2.10, the sensor response ($\Delta(\lambda_4-\lambda_3)$) for the orthogonal direction was observed to be zero as expected from Eq. (2.2). On the other hand, sensor response ($\Delta(\lambda_2-\lambda_1)$) is observed to be linear for the forward as well as the reverse tilt variations as predicted by Eq. 2.1. Measured linear sensitivities for forward (0^o-10^o) and reverse (10^o-0^o) directions are found to

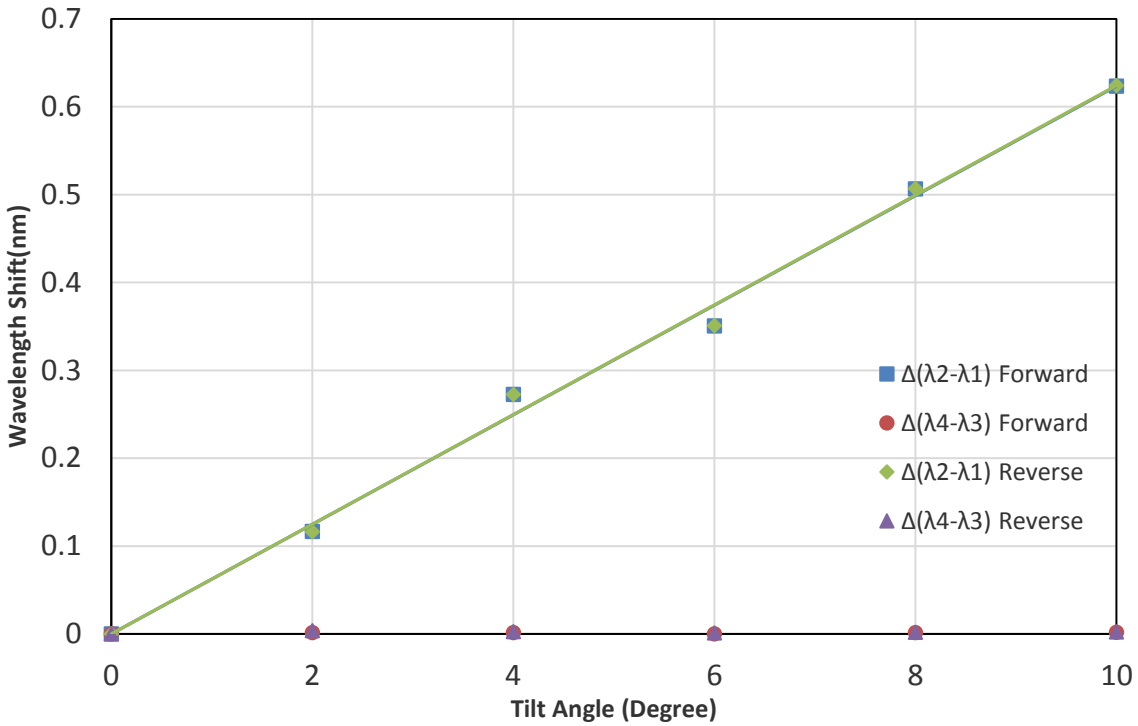

Figure 2.10: *Variation of $\Delta(\lambda_2-\lambda_1)$ for the +ve forward & reverse tilt in the y-z plane where the sensor employed higher mass. $\Delta(\lambda_4-\lambda_3)$ shows the cross axis response.*

be 0.0626nm/^{o} and 0.0624nm/^{o}, respectively. On the other hand, Fig. 2.11 depicts wavelength differences, $\Delta(\lambda_2-\lambda_1)$ and $\Delta(\lambda_4-\lambda_3)$, for 0^o–(-10^o) (reverse tilt) and $(-10^o$–$0^o)$ (forward tilt) for the negative direction in the same (*y-z*) plane. Following observations can be made from Fig. 2.11: (a) response in orthogonal plane, i.e., $\Delta(\lambda_4-\lambda_3)$ is again found to be zero as predicted by

Eq. (2.2). (b) sensor response, $\Delta(\lambda_1-\lambda_2)$, is linear again in the 0^o-(-10^o) and (-10^o)-0^o tilt angle variations; (c) measured linear sensitivities for forward and reverse directions are once again found to be 0.0626nm/^{o} and 0.0624nm/^{o}, respectively. Linear response with identical sensitivity during the complete cycle of applied tilt (0^o-10^o-0^o and then 0^o-(-10^o)-0^o) manifests a highly reversible nature of the sensor.

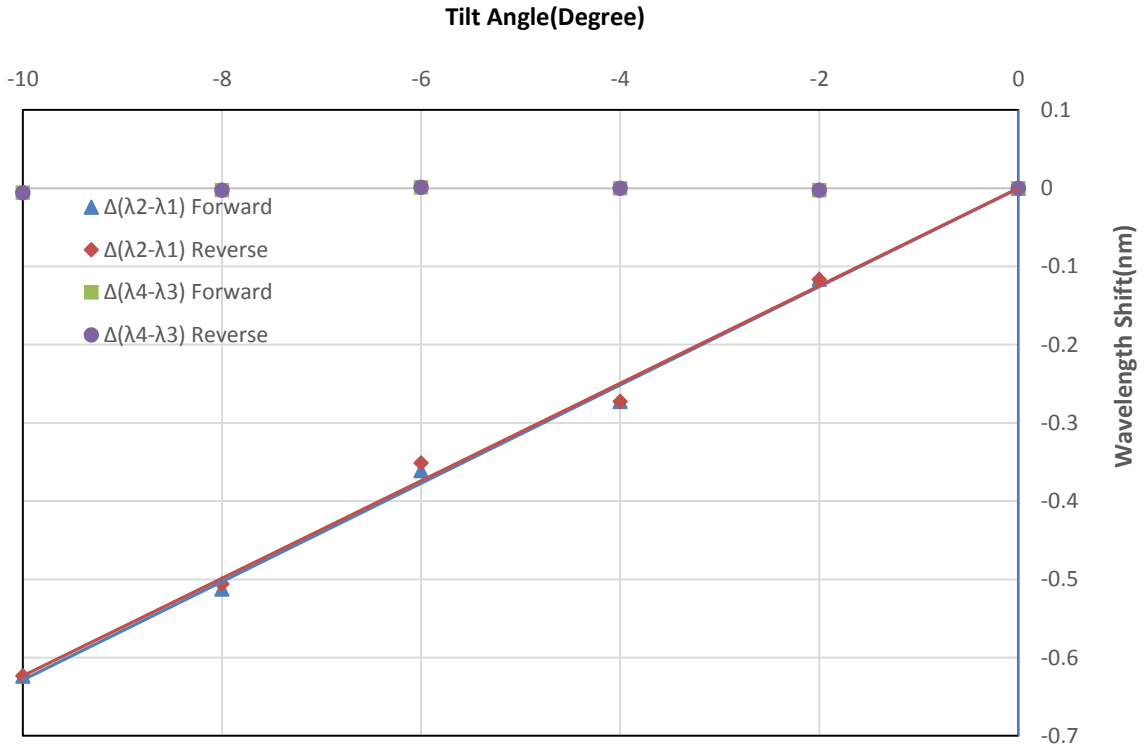

Figure 2.11: *Variation of $\Delta(\lambda_2-\lambda_1)$ for the -ve forward & reverse tilt in the y-z plane where the sensor employed higher mass. $\Delta(\lambda_4-\lambda_3)$ shows the cross axis response.*

Identical response was observed when the tilt angle in the *x-z* plane was varied from 0° to 10° to 0° and then from 0° to -10° to 0°. In order to analyze the sensor performance critically, sensor's response during the forward and reverse tilt variations in all the three sets were considered again for this sensor employing larger mass. A maximum discrepancy across all the experimental sets (for both the planes, *y-z* and *x-z*) is observed to be less than ±0.0231nm with corresponding maximum angular uncertainty of ±0.3403^o for both forward as well as

reverse directions of applied tilt. Average discrepancy is observed to be less than ±0.00016nm. Angular resolution of 0.0080^o along with an accuracy of tilt angle measurement is observed to be ±0.36^o. All the performance characteristics of the developed sensor are summarized in Table 2.1 for easy reference.

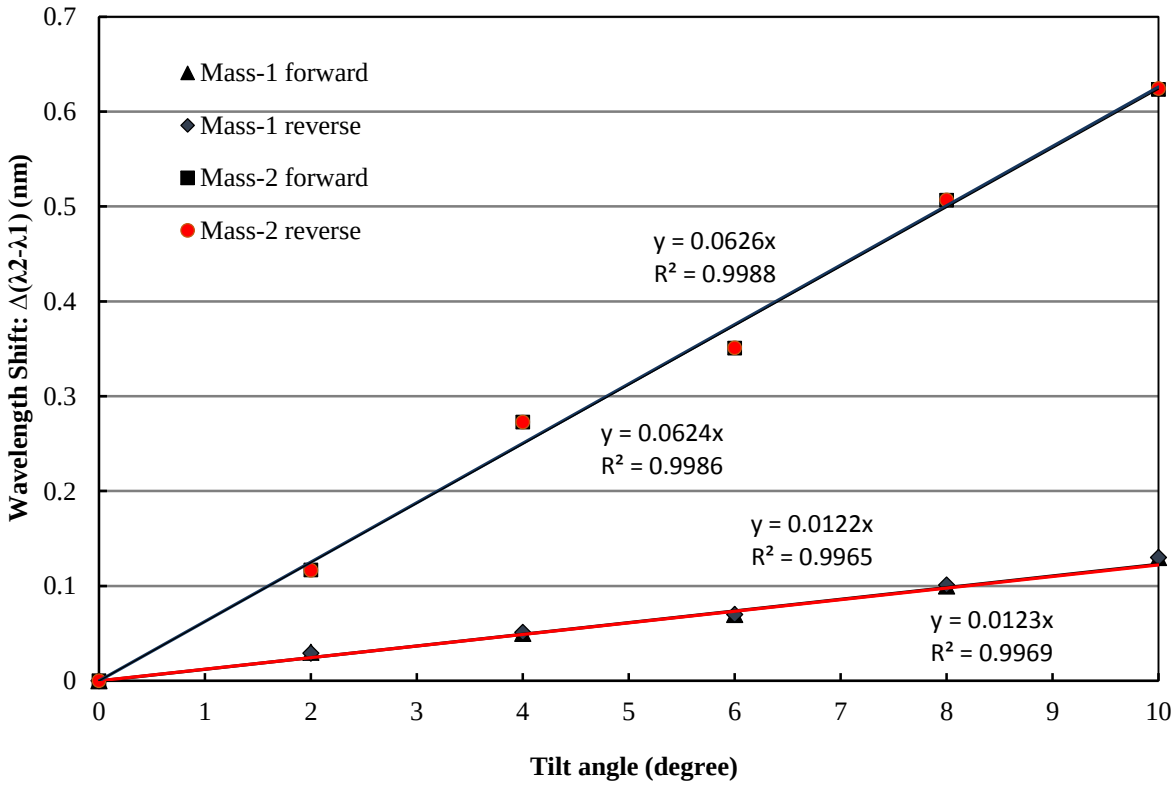

Figure 2.12: *Experimentally observed sensor responses with two different masses for the +ve tilt (0^o to 10^o).*

In order to have a comparative analysis of the sensor response along with the effect of varying mass on the observed sensitivity, responses of the sensor comprising mass-1 as well as mass-2 are plotted together in Fig. 2.12 for +ve and Fig. 2.13 for –ve forward and reverse tilts respectively. A remarkable feature of the proposed sensor that can be observed from Table 2.1 (or from Fig. 2.12/Fig. 2.13) is that, an increase in the mass of the bob from 67g (mass-1) to 110g (mass-2) which is 1.64 times increase, results in a 5.1 times increase in the

sensitivity. Such a manifold (nonlinear) sensitivity enhancing/tuning capability is achieved for the first time to the best of author's knowledge. Further, the observed resolution (0.0080^o) as well as the measurement accuracy (±0.36^o) both improved substantially employing higher

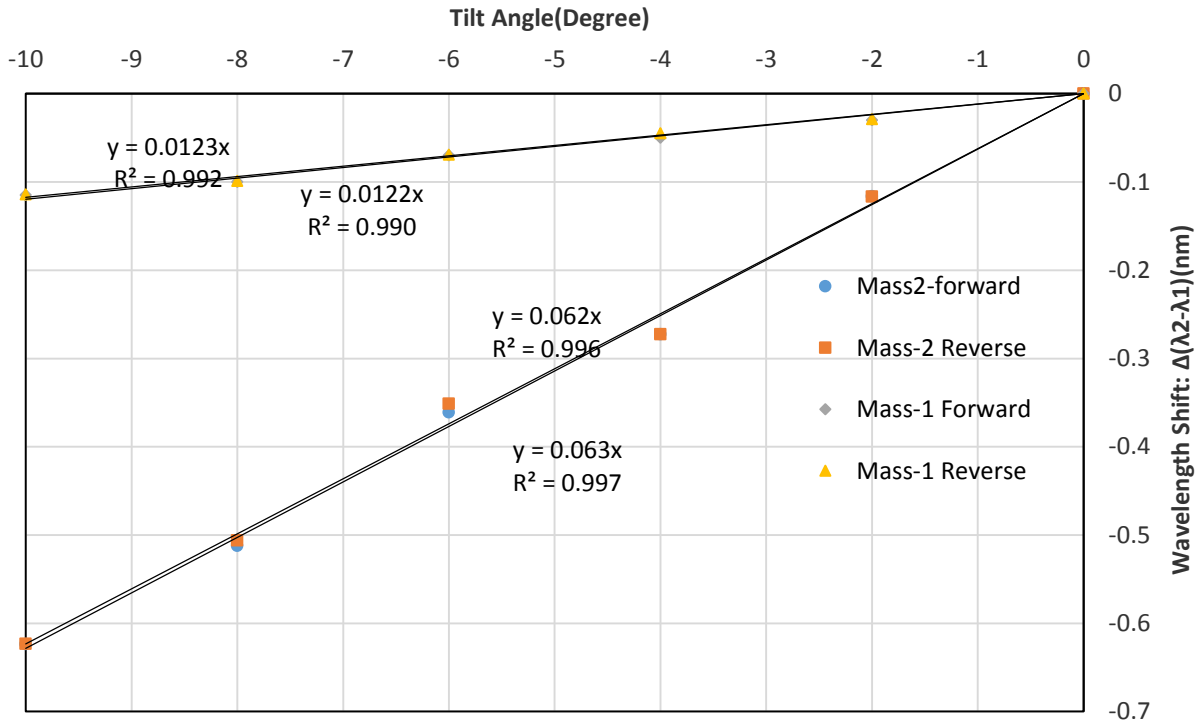

Figure 2.13: *Experimentally observed sensor responses with two different masses for the –ve tilt (0^o to -10^o).*

mass in the sensor as against the observed resolution (0.0407^o) and the measurement accuracy (±0.56^o) observed when sensor employed a lesser mass.

Table 2.1: Summary of performance characteristics of the proposed sensor

Mass (g)	Sensitivity		Resolution	Max. Discrepancy (nm)	Average Discrepancy (nm)	Accuracy of tilt measurement
	Forward	Reverse				
67	0.0123	0.0122	0.0407°	<±0.0069	±0.0008	~±0.56°
110.3	0.0626	0.0624	0.0080°	<±0.0231	±0.00016	~±0.36°

Next, we compared the performance characteristics of the proposed sensor with the other FBG based tilt sensors reported in the literature. Table 2.2 lists a few important features of these sensors for comparison. As can be observed from the Table 2.2, highest sensitivity of 0.192nm/^{o} was reported by He et.al. [71] within the dynamic range of -12° to +12°. However, mass of the bob used in [71] was 200g, which is 1.8 times higher than the mass (mass-2) used in the reported sensor. If the mass in the present sensor is increased to the mass used in [71], and if we still assume a 5.1 times increase in the sensitivity (which actually corresponds to 1.64 times increase in mass), the expected sensitivity would be of the order of 0.319 nm/^{o}. This is much higher than the reported sensitivity in [71]. It's worth mentioning again that the measured tilt range for the proposed sensor was limited to the maximum tilt span (±10^o) of the available goniometer in the laboratory, and we could not execute experiments to the designed range of ±45^o.

Table 2.2: Comparison of the sensor response

Author	Mass of bob (g)	Sensitivity (nm/^{o})	Accuracy	Resolution	Dynamic range
Guan et al. [67]	344	0.0752	±0.1^o	0.007^o	-09^o to +03^o
Chen et al. [69]	357	0.0600	±0.167^o	0.0067^o	-15^o to +15^o
Bao et al. [70]	500	0.096	±0.2^o	0.013^o	-40^o to +40^o
He et al. [71]	200	0.192	±0.1^o	0.005^o	-12^o to +12^o
Ni et al. [72]	100	0.0537	–	0.009^o	-10^o to +10^o
Au et al. [45]	170	0.0395	±0.051^o	0.013^o	-07^o to +07^o
Reported sensor	110	0.0626	±0.36^o	0.008^o	-10^o to +10^o

Finally, long-term repeatability and reliability of the performance characteristic for any sensor system is another critical and desirable feature for its real-field practical application. As mentioned earlier, a total of three sets of experiments each comprising +ve and –ve forward/reverse tilt variations were performed on three different days with an interval of one week each. It is these data, which are used to examine long-term repeatability and reliability criteria for the developed sensor. Sensor outputs corresponding to the four different tilt angles (2^o, 4^o, 6^o and 8^o) as an example for the sensor comprising larger mass are shown in Fig. 2.14. As can be observed, sensor output is almost constant over a span of two weeks. Compared to day 1, a maximum variation in the sensor output at the four different tilt values (2^o, 4^o, 6^o and 8^o) is observed to be of the order of 10^{-4} nm. This shows a good reliability and repeatability of the proposed sensor. Thus, the proposed FBG based tilt sensor with the inherent nonlinear tunability of its sensitivity along with highly reversible and reliable performance characteristics is of great importance for various real-field engineering applications.

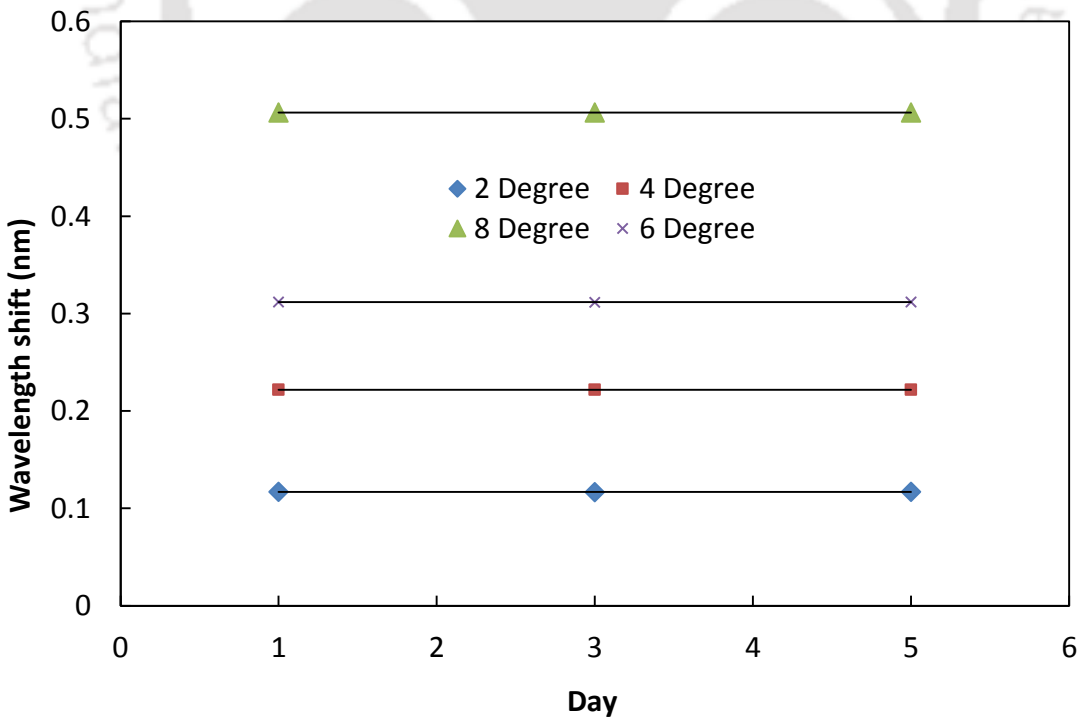

Figure 2.14: *Repeatability and reliability test: FBG tilt sensor output on the three different days for 2^o, 4^o, 6^o and 8^o tilts.*

2.4 Conclusion

This chapter described the development of a novel optical fiber tilt sensor employing very strategically four FBGs for capturing the applied tilt with a nonlinearly enhanced sensitivity. With the employed mechanical strategy, proposed sensor is free from the design constraints of other reported sensors in the literature. This sensor is capable of measuring the magnitude as well as the direction of the inclination from the horizontal direction. A remarkable feature of the proposed sensor is the provision to increase the sensitivity manifold by simply increasing the mass of the bob. Sensor's response is investigated with two different masses in a tilt measurement range of -10^{o}–10^{o} (limited by the measurement range of the available goniometer). Its important to mention that this sensor is designed and capable to measuring tilt over the dynamic range of -45^{o} to $+45^{o}$. For both masses, sensor responses are observed to be linear and highly reversible. With higher mass, measured sensitivity is found to be 0.0626nm/^{o} for forward direction and 0.0624nm/^{o} for reverse direction in *y-z* plane with tilt angle measurement accuracy of $\pm 0.36^{o}$, resolution of 0.008^{o}, maximum discrepancy less than ±0.0231 nm and maximum angular uncertainty of $\sim\pm 0.34^{o}$. Identical response was observed in *x-z* plane also. The major limitation associated with FBG based sensor is the temperature cross sensitivity. However, as the developed sensor measures tilt angle by measuring the difference in wavelength shifts of two FBGs, it is free from temperature cross-sensitivity. Hence, it can be used for real-field industrial/engineering applications. Next chapter of the thesis is devoted to improve further the performance characteristics for a FBG based all-optical tilt sensor.

Chapter 3

Stable and Effective Temperature Insensitive Fiber Bragg Grating Based Tilt Sensor Employing Non-pendulum Type Design Strategy

3.1 Introduction

Last chapter described the development of fiber Bragg grating (FBG) based tilt sensor with a focus to achieve inherent enhanced tuning capability for the sensitivity. As observed, nonlinearly enhanced sensitivity tunability was realized by varying only one sensor parameter, which was the mass of employed bob. From the point of view of structural-health-monitoring and real-field applications, though, a reasonably good sensitivity is required; the tilt sensor is simultaneously desired to have an ability to capture the tilt perturbations strategically very effectively and without any inherent instability. Measure sources of the inherent instabilities in capturing the applied tilt for all the reported sensors in the literature lie with (a) the hanging strategy of the bob (either in cantilever form [67, 68, 70, 45] or with the fiber [71, 72]), which also leads to the cross sensitivity towards unwanted perturbations; and (b) the rotational/mechanical frictions within the sensor design [67, 68, 70, 45]. Further, for the sensor design with inherent instabilities, any unwanted add-on oscillation is expected to create noise in the tilt measurement through (a) the random vibration/oscillation of the hanging pendulum systems and (b) the slackening of fibers. Relatively smaller discrepancy as well as uncertainty and a better angular resolution along with accuracy in the tilt measurement manifest a stable and effective sensing mechanism.

The objective of research reported in this chapter is to develop a design strategy that negates internal instabilities along with constraints imposed by inherent rotational/mechanical frictions in better ways while enabling tilt measurement more effectively and accurately in the optical domain. A very simple non-pendulum type design strategy, which is theoretically capable of monitoring tilt/inclination from horizontal in a dynamic range of ±45^o, is employed in order to develop an all-optical FBG based tilt sensor for the first time to the best of author's knowledge. Non-pendulum mechanism inherits a better design and working stability in comparison to the pendulum based mechanism. Also, a non-pendulum design strategy is free from any mechanical joints and inherent frictions while in application. Further, in the present scheme, imprinting of the inclination/tilt angle variations in optical domain is achieved by decoding the inclination/tilt angle information from the peak wavelength separation between two FBGs. This optical diagnostic mechanism makes the proposed sensor temperature-insensitive. Experimental results show that a maximum discrepancy of ±0.001 nm with a tilt angle measurement accuracy of ~ ±0.05^o, a tilt angle resolution better than 0.0041^o and the sensitivity of the order of ~0.012 nm/^{o} is achieved. Experimental results also depict a highly reliable and reversible nature of the sensor's response characteristics.

3.2 Experimental

3.2.1 Sensor Design and Construction

Two rectangular plates (6.0×1.2×1.0 cm^3) are rigidly joined by two identical vertical brass rods of diameter 0.6 cm and length 9 cm as shown in Figure 3.1 (a). A *circular disc* (1 cm inner and 2.83cm outer diameter, thickness 1 cm) is fixed at the upper surface of the top rectangular plate; whereas, a *circular plate* (2.83cm diameter, thickness 1 cm) is fixed at the lower surface of the bottom rectangular plate. While fixing the *circular disc* and the *plate*,

proper care is taken in order to maintain their centres on the vertical axis of this structure. A *small circular plate* (1 cm diameter) is inserted into the central part of the *circular disc*. A hole of diameter 0.5 mm is drilled along the vertical axis of this structure; i.e., through the centre of *small circular plate*, top rectangular plate as well of the bottom rectangular plate. A hole of identical diameter is also drilled separately along the diameter of a steel bob (dia 2.83

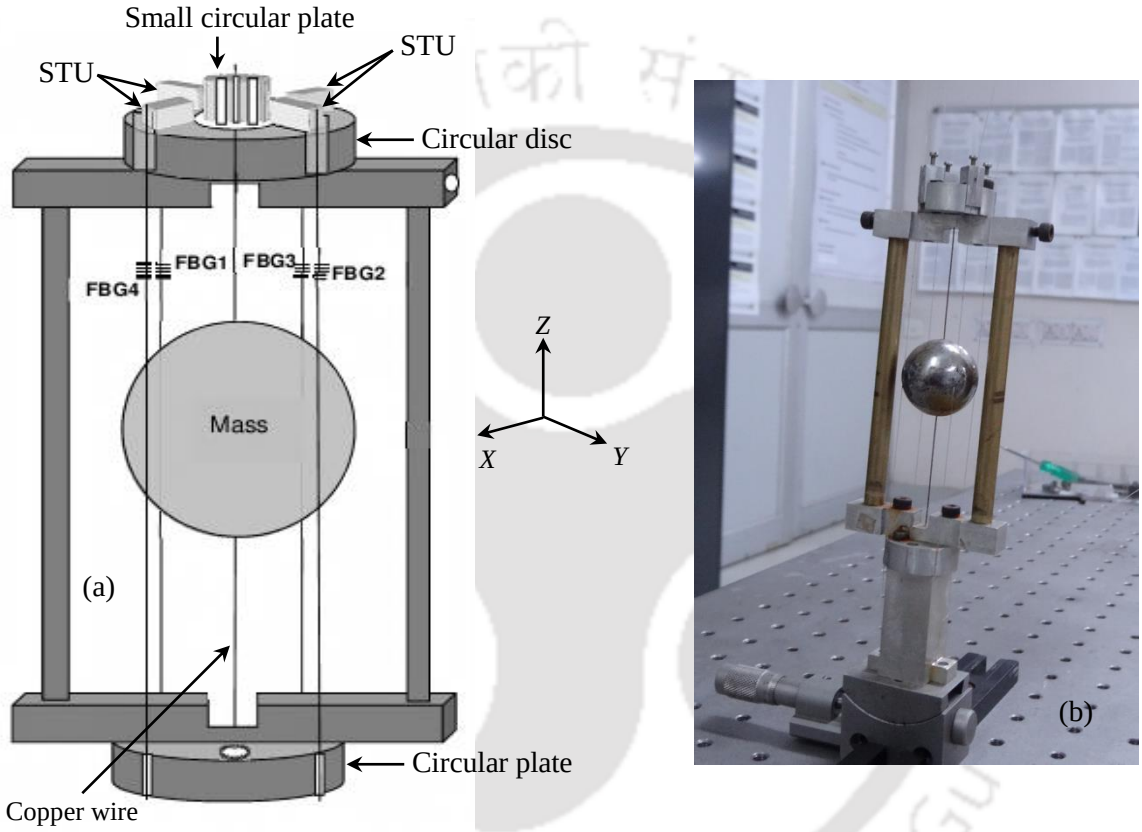

Figure 3.1: (a) *Schematic diagram of the proposed FBG based tilt sensor and (b) photograph of the sensor.*

cm, mass ~90g). A copper wire of diameter 0.45mm is inserted into the hole and is rigidly fixed to the bob first. The two open ends of the copper wires are then fixed to the *small circular plate* at the top and the rectangular plate at the bottom. In this arrangement, copper wire coincides with the vertical axis of the structure; whereas bob remains at the vertical centre of the structure. Also, *small circular plate* inside the *circular disc* rests on the top

rectangular plate in the sensor design. In order to tune strain in the copper wire, two holes with M2 threading are drilled into the *small circular plate* and M2 screws are fixed in it. Turning the M2 screws moves *small circular plate* along the upward direction w.r.t. the top rectangular plate and thus allows strain tuning in the copper wire.

Two pairs of vertical grooves (~0.5 mm depth each) are made along the diagonally opposite points on the side cylindrical surface of the *circular plate* (fixed at the lower surface of the bottom rectangular plate). The two diagonals carrying the pair of vertical grooves are orthogonal to each other (see Fig. 3.1(a)). On the other hand, two pairs of vertical channels (2 mm width each) are made along the diagonally opposite points on the side cylindrical surface of the *circular disc* (fixed to the rectangular plate at the top). The two diagonals carrying the pair of vertical channels are orthogonal to each other (see Fig. 3.1(a)) and parallel to the diagonals used in *circular plate* at the bottom of the design. Four Π-shaped metallic strain tuning units (STUs) are designed. Length and width of the vertical legs of Π-shaped STUs are 10 mm and 2 mm respectively. Separation between the two vertical legs is 6 mm. Total breadth of STUs is 5 mm. These STUs are fixed onto the *circular disc* such that one vertical leg rests inside the channel whereas the other inside a hole drilled on the *circular disc* (hole diameter and depth were 2 mm and 5 mm, respectively) (Fig. 3.1(a)). Each STUs carries a vertical groove (~0.5 mm depth) on the outer surface of that leg which rests inside the channel. Each STUs also carries holes with M2 threading having M2 screws fixed in it. In the sensor design, four grooves on the STUs attached to the *circular disc* (on the top) and the four grooves on the cylindrical surface of the *circular plate* (at the bottom) are collinear.

Four FBGs are written onto a single fiber such that the distance between FBG1 and FBG2 as well as between FBG3 and FBG4 are kept identical. Starting from one groove (say, 1) on the

lower *circular plate*, this fiber is then glued at the tangential point of the bob (say, T1), to the groove on the STU at the upper *circular disc* (say, 1), to the diagonally opposite groove on the STU at the upper *circular disc* (say, 3), at the tangential point of the bob (say, T3), to the groove (say, 3) on the lower *circular plate*, to the adjacent groove (say, 2) on the lower *circular plate*, at the tangential point of the bob (say, T2), to the groove on the STU at the upper *circular disc* (say, 2), to the diagonally opposite groove on the STU at the upper *circular disc* (say, 4), at the tangential point of the bob (say, T4) and finally to the groove (say, 4) on the lower *circular plate*. In this arrangement, all the four FBGs are in the middle of the length between the tangential points on the bob and the STUs. Further, FBG1 and FBG2 are in the same vertical plane (say, *y*-*z* plane) whereas FBG3 and FBG4 are in another vertical plane (*x*-*z* plane) which is normal to the plane carrying FBG1 and FBG2. As STUs rest on the *circular disc*, turning the M2 screw fixed in it results in an upward movement of these units w.r.t. the *circular disc*. This facilitates strain tuning in each fiber arms. Photograph of the developed sensor is shown in Fig. 3.1(b).

3.2.2 Sensing Principle

As the sensor is tilted in one vertical plane, theoretically the two FBGs in that plane are loaded unequally; and the other two FBGs in the plane, perpendicular to the tilt plane, are loaded equally. A detailed theoretical analysis of the sensor response shows that, when the sensor is inclined by an angle φ, say in the *y*-*z* plane keeping inclination in *x*-*z* plane zero, strain in the gratings gets redistributed; and the corresponding wavelength difference in *y*-*z* and *x*-*z* plane is given by

$$\Delta(\lambda_2 - \lambda_1) = \frac{mg}{2AE}\lambda_1(1 - P_e)\sin\phi \tag{3.1}$$

$$\Delta(\lambda_4 - \lambda_3) = 0 \tag{3.2}$$

Identically, when the sensor is inclined by an angle φ in the *x*-*z* plane keeping inclination in *y*-*z* plane zero, the strain in the gratings gets redistributed; and the corresponding wavelength difference in *x*-*z* and *y*-*z* plane is given by

$$\Delta(\lambda_4 - \lambda_3) = \frac{mg}{2AE}\lambda_3(1 - P_e)\sin\phi \tag{3.3}$$

$$\Delta(\lambda_2\text{-}\lambda_1) = 0 \tag{3.4}$$

Here m is the mass of the bob used in the sensor design, g is the acceleration due to gravity, P_e is the photoelastic constant of the fiber, A is the area of cross-section of the fiber and E is the Young's modulus of the material of the fiber. Referring to Eq. (3.1) and (3.3), following features of the proposed sensor are worth mentioning: (a) for small tilt angle variations, wavelength separations, $\Delta(\lambda_2 - \lambda_1)$ and $\Delta(\lambda_4 - \lambda_3)$, are linearly proportional to φ; (b) sensitivity of the sensor, which is fractional change in the wavelength difference for an applied tilt, is linearly proportional to $m/2$; (c) sensitivity can be tuned to the desired value by suitably changing the mass of the bob (m); and (d) temperature-change during the experiment shifts each FBG's wavelength in the same direction. As the wavelength difference of the pair of FBGs would be measured against the suitably applied tilt, temperature cross-talk in the final measurement would automatically be eliminated; making the sensor's response temperature independent.

3.2.3 Sensor characterization

Four FBGs were written onto a single fiber using phase-mask technique. Hydrogen-loaded single-mode optical fiber with characteristic parameters given by 7.27×10^{10} N/m^2 as Young's modulus of the host material (E); 1.2266×10^{-8} m^2 as the cross section area of the fiber (A) and 0.22 as the photoelastic coefficient of the optical fiber (P_e) was used for FBG writing. FBGs were written on this fiber such that the distance between FBG1 and FBG2 as well as between

FBG3 and FBG4 were kept identical. The peak reflection wavelengths of the FBGs were 1540.01 nm (FBG1, λ_1), 1543.75 nm (FBG2, λ_2), 1554.871 nm (FBG3, λ_3) and 1559.21 nm (FBG4, λ_4). Fiber carrying four FBGs was glued at two sets of diametrically opposite STUs on the top circular disc and at the corresponding two sets of diametrically opposite STUs on the bottom circular plate via tangential points of the bob as explained in the previous section. All the four FBGs remained equidistant from the top circular disc in the corresponding fiber arms. These gratings were then equally pre-strained by a pre-determined value (1750 με) through the four STUs. The one end of the fiber carrying four FBGs was connected to FBG interrogator (Micron Optics, SM130-700, resolution 0.05 pm). Sensor was then mounted on the available tilt stage (goniometer), which had a provision to turn the sensor within $\pm 10^o$ range only. This was the laboratory constraints. It is important to mention that, though the experiment was performed within the maximum tilt limit of the available goniometer, i.e., within the tilt range of $\pm 10^o$, sensor is actually designed for a $\pm 45^o$ applied tilt. To carry out the experiment, the sensor was first tilted in the plane of FBG3 and FBG4 (*x*-*z* plane), keeping the tilt in the plane of FBG1 and FBG2 (*y*-*z* plane) zero. The tilt angle was varied from -10^o to 10^o (forward) and then back to -10^o (reverse) in a suitable minimum steps allowed by the goniometer. During the experiment, reflection spectra of four FBGs against the applied tilt angle (ϕ) were monitored using the interrogator.

3.3 Results and Discussion

Proposed sensor was mounted on the available tilt stage (goniometer) in order to investigate its response characteristics. The sensor was first tilted in the plane of FBG3 and FBG4 (*x*-*z* plane), keeping the tilt in the plane of FBG1 and FBG2 (*y*-*z* plane) zero. During the experiment, reflection spectra of four FBGs (FBG3 and FBG4 in the plane of inclination,

whereas FBG1 and FBG2 in a plane perpendicular to that of the inclination) against the applied tilt angle (ϕ) were monitored using an FBG interrogator. Experiment was repeated afterwards by applying tilt variations to the sensor in *y-z* plane (plane carrying FBG1 and FBG2). Figure 3.2 depicts, as an example, wavelength response of individual FBG employed in the sensor during tilt variations from -10° to +10° (forward tilt) in *x-z* plane. A similar wavelength response was observed during the reverse tilt in *x-z* plane as well as for the tilt variations in *y-z* plane. Following observations can be made from Fig. 3.2: (a) wavelength response of all individual FBG is not symmetrical about zero tilt position while tilting the sensor in ±10° range. Ideally, response characteristics should be symmetrical about zero tilt position; (b) FBG1 and FBG2 responded identically while applying tilt; (c) FBG3 and FBG4 responded differently and almost oppositely while applying tilt; (d) wavelength response of all individual FBG is nonlinear while tilting the sensor in ±10° range. Ideally

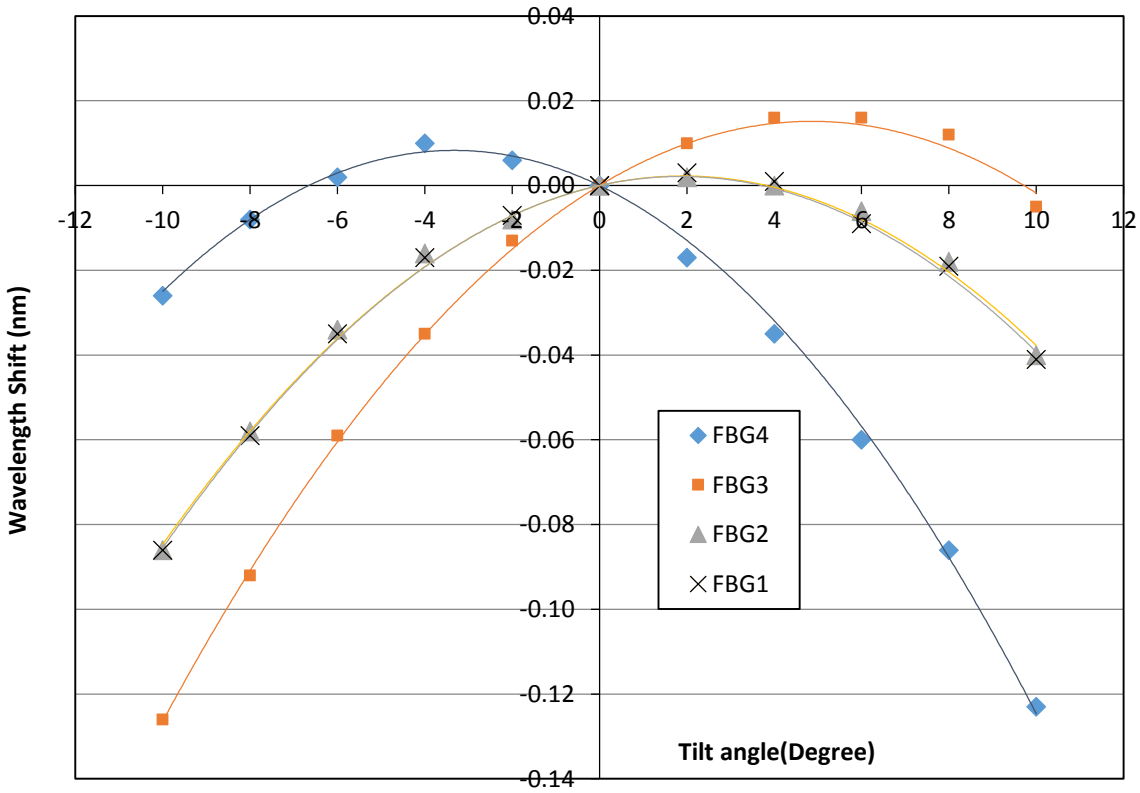

Figure 3.2: *Individual responses of four FBGs with respect to tilt.*

response of FBGs should have a linear relationship with the applied tilt. A nonlinear relationship indicates that the actual strain induced on FBG 1 and FBG 2 or FBG 3 and FBG 4 is not equal. In other ways, this means that one FBG bears much larger strain than the other. A possible reason for the nonlinear response could be a minor deviation of the vertical plane carrying FBG3 & FBG4 from the vertical plane in which tilt is applied; and hence an unequal & complex strain distribution across all FBGs. Nevertheless, actual response characteristics of the proposed sensor is manifested by wavelength differences, $\Delta(\lambda_4 - \lambda_3)$ and $\Delta(\lambda_2-\lambda_1)$ as defined by Eqs (3.1) & (3.2) for *x*-*z* plane and by Eqs (3.3) & (3.4) for *y*-*z* plane. In order to investigate response characteristics of the sensor, experimentally observed $\Delta(\lambda_4 - \lambda_3)$ for 0^o-10^o (forward) and 10^o-0^o (reverse) tilt is plotted in Fig. 3.3 (tilted square for the forward and square for the reverse tilt). Sensor's response $\Delta(\lambda_2-\lambda_1)$ in the plane normal to the one in which tilt is applied, i.e., plane carrying FBG1 and FBG2 is also shown in the same figure (triangle for the forward and cross for the reverse tilt). Following observations can be made from Fig. 3.3: (a) sensor response, $\Delta(\lambda_4-\lambda_3)$, is linear in the 0^o-10^o and 10^o-0^o tilt angle variations; (b) measured linear sensitivities for forward (0^o-10^o) and reverse (10^o-0^o) directions are found to be exactly identical, having value equal to 0.012nm/^{o}. This manifests a highly reversible nature of the sensor; (c) response in orthogonal plane, i.e., $\Delta(\lambda_2-\lambda_1)$ was found to be zero as predicted by Eq. (3.4). Further, the maximum discrepancy is observed to be less than ±0.001nm with corresponding angular uncertainty of ~$\pm0.05^o$ for forward as well as the reverse directions in both the planes. The resolution of the sensor completely depends on the resolution of the interrogating device. An angular resolution as small as 0.0041^o is observed in this case. Afterwards, tilt was applied in the opposite direction: 0^o-(-10^o) (forward) and (-10^o)-0^o (reverse). Fig. 3.4 shows the sensor response, $\Delta(\lambda_4-\lambda_3)$ as well as $\Delta(\lambda_2-\lambda_1)$, against the tilt, which is applied to the plane carrying FBG3 and FBG4 (*x*-*z* plane). Following

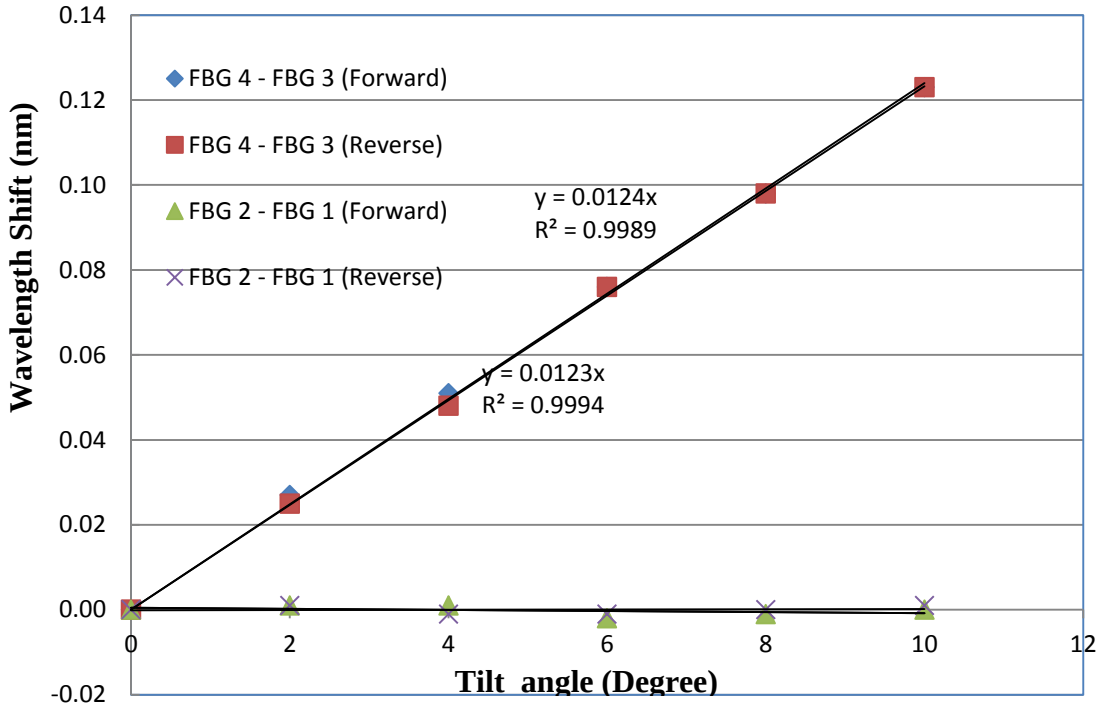

Figure 3.3: *Sensor response $\Delta(\lambda_4-\lambda_3)$ for the +ve forward and reverse tilt in the plane on FBG4 and FBG3. $\Delta(\lambda_1-\lambda_2)$ shows the cross axis response.*

can be made from Fig. 3.4: (a) sensor response, $\Delta(\lambda_4-\lambda_3)$, is linear again in the 0^o-(-10^o) and (-10^o)-0^o tilt angle variations; (b) measured linear sensitivities for forward and reverse directions are found to be exactly identical, having value equal to 0.011nm/^{o}. This manifests a highly reversible nature of the sensor. It's important to mention that the sensitivity should ideally not depend whether the tilt is applied in 0^o-10^o-0^o or 0^o-(-10^o)-0^o cycle; (c) response in orthogonal plane, i.e., $\Delta(\lambda_2-\lambda_1)$ was again found to be zero as predicted by Eq. (3.4). Maximum discrepancy, corresponding angular uncertainty and the angular resolution are observed to be the same as for the tilt variations in 0^o-10^o-0^o range. Responses, similar to the one depicted in Fig. 3.3 and 3.4, was observed when the sensor was tilted in the orthogonal plane of FBG1 and FBG2 (*y*-*z* plane) keeping the tilt in the plane of FBG3 and FBG4 (*x*-*z* plane) zero for both forward and the reverse directions.

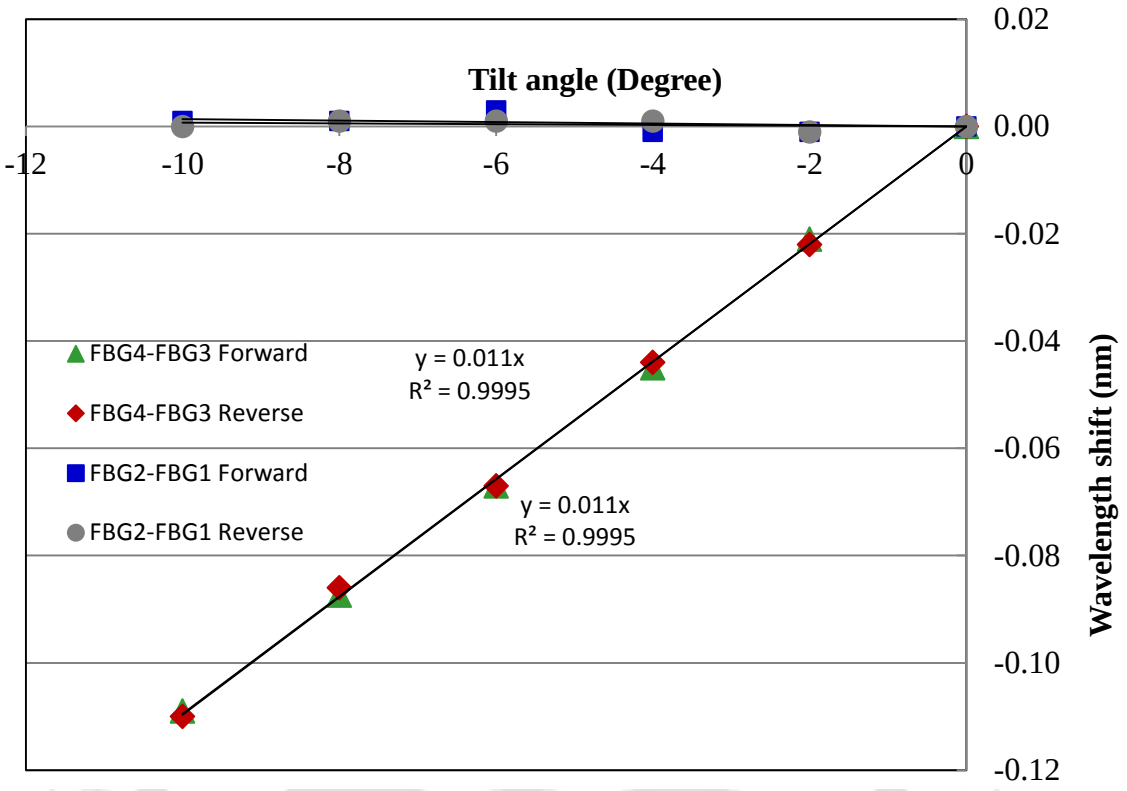

Figure 3.4*: Sensor response $\Delta(\lambda_4-\lambda_3)$ for the -ve forward and reverse tilt in the plane on FBG4 and FBG3. $\Delta(\lambda_1-\lambda_2)$ shows the cross axis response.*

Next, the performance characteristics of the proposed FBG based non-pendulum-type sensor is compared with the other FBG based tilt sensors that employed pendulum suspension mechanism. Table 3.1 lists, for comparison, the most important parameters (such as measurement accuracy, maximum discrepancy in the measurement etc, in addition to the sensitivity) those are required for estimating/analyzing stable and effective sensing capabilities of a given sensor. The value of the mass of the bob (m) that is used for the development of these pendulum type FBG sensors (listed in the Table 3.1) and the sensitivity dependence on this mass for these sensors are also summarized in the same table. As can be observed from the Table 3.1, best tilt angle measurement accuracy and the lowest maximum discrepancy in the measurement is achieved in the present work. On the other hand, at the

first sight, sensitivity of the proposed sensor appeared to be the lowest among the other sensors tabulated here. However, mass of the bob used in all the other studies tabulated here

Table 3.1: Comparison of the performance characteristics of the developed sensor

Author	Sensitivity dependence on the mass of the bob	Mass of bob (*m*)	Sensitivity (nm/°)	Accuracy	Maximum discrepancy (nm)	Angular resolution
Guan et al. [67]	*m*	344	0.0752	±0.1°	±0.008	0.007°
Bao et al. [70]	8*m*	500	0.096	±0.2°	–	0.013°
Au et al. [45]	*m*	170	0.0395	±0.051°	±0.002	0.013°
Ni et al. [72]	*m*	100	0.0537	–	±0.015	0.009°
Chen et al. [69]	*m*	357	0.06	±0.167°	–	0.0067°
Reported sensor	*m*/2	90	0.012	±0.05°	±0.001	0.0041°

were higher than the one used in the present study. As already stated in the previous section, sensitivity of the tilt measurement is defined by fractional change in the wavelength difference for an applied tilt. As depicted by Equations (3.1) and (3.3), sensitivity varies in linear proportion to *m*/2 for the reported sensor. This means, the effective mass is half of the employed mass in the proposed design. Analyzing relations for sensitivity (i.e., relation for fractional change in the wavelength difference for an applied tilt) for the tilt sensors that employed pendulum suspension mechanism and listed in Table 3.1, it is important to mention that sensitivity varies in all these sensors in linear proportion to either *m* or to 8*m*. This means, effective mass is either the employed mass itself (which is double in comparison to

the effective mass in the proposed sensor) or eight times the employed mass (which is sixteen times in comparison to the effective mass in the proposed sensor) in these sensor designs. Highest tilt angle measurement sensitivity of 0.096nm/^{o} was reported by Bao et.al. [70] within the dynamic range of -12^o to +12^o. Here, the employed mass of the bob was 500g (5.56 times of 90g, the mass used in the present study) and sensitivity varied as eight times of this mass. Incorporating equivalently these two features of [70], namely eight times dependence of sensitivity on the mass and a mass 5.56 times high, the expected sensitivity of the proposed sensor in the present study would be of the order of 1.07 nm/^{o}. This is much higher than the sensitivity reported in [70]. It's worth mentioning again that the measured tilt range for the proposed sensor was limited to the maximum tilt span of the available goniometer in the laboratory (±10^o); and hence, experiments could not be executed to the designed range of ±45^o. Further, while comparing the response characteristics of this sensor with the one reported in Chapter 2, it's important to mention that interrogators used for studying the response characteristics of sensors reported in this chapter and in the previous chapter are different having different resolutions. As pointed out earlier, sensor resolution depends upon the resolution of the interrogator. Nevertheless, maximum discrepancy, measurement accuracy and the sensitivity do not depend on the resolution of the interrogator; and are simply the characteristics of the sensor. As mentioned in the previous section, an effective and stable tilt measurement without any inherent instability is manifested, as an example, by improved discrepancy and accuracy. In comparison to the maximum discrepancy of ±0.0231nm and tilt measurement accuracy of ±0.36^o observed for the sensor implying higher mass that resulted with higher sensitivity in the previous chapter, maximum discrepancy as low as ±0.001nm and tilt measurement accuracy as better as ±0.05^o is observed for the sensor reported in this chapter. These characteristics depict a successful realization of the objectives laid down for the sensor development carried out in this chapter.

In the next and important step, repeatability and reliability tests are carried out to rigorously analyze the sensor performance. For this, experiments were repeated on 3 different days with an interval of a week. Sensor outputs corresponding to the four different tilt angles (2º, 4º, 6º and 8º) as an example are shown in Fig. 3.5. As can be observed, sensor output is almost constant over a span of 2 weeks. Compared to day 1, a maximum variation in the sensor output at the four different tilt values (2º, 4º, 6º and 8º) is observed to be of the order of 10^{-3} nm. This shows a good reliability and repeatability of the proposed sensor. Finally, as mentioned earlier, proposed sensor exploits peak wavelength difference measurement between a pair of FBG against an applied perturbation rather than a measurement of absolute shift in peak wavelength of a given FBG for an applied perturbation. In this strategy, the cross-talk resulting from ambient temperature fluctuations is automatically eliminated. Nevertheless, it is very important to investigate the response characteristics of the developed

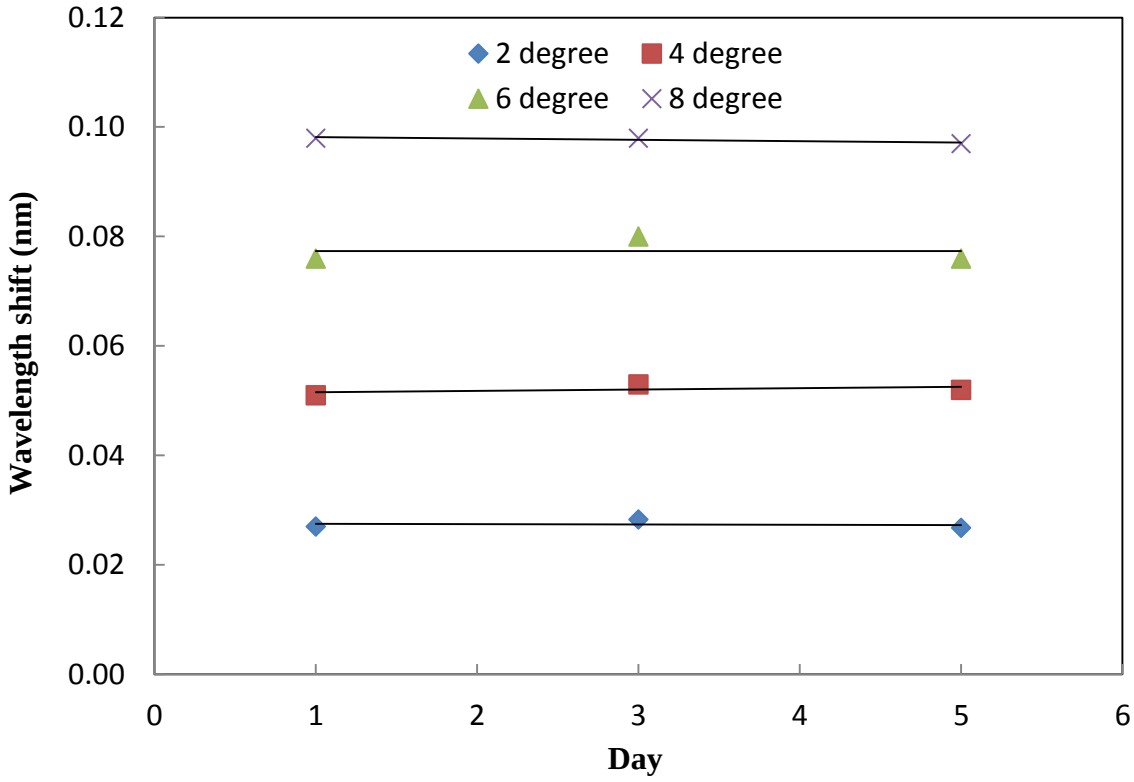

Figure 3.5: *Repeatability and reliability test: FBG tilt sensor output on the three different days for 2º, 4º, 6º and 8º tilts.*

sensor against the ambient temperature variations to justify the theoretically predicted temperature independency in its characteristics. This is critical for the practical deployment of the sensor in real field applications. Hence, the proposed sensor was first fixed inside a water-tank made by Perspex sheet. Water was poured inside the water-tank to the level to ensure that the sensor remained completely immersed in it throughout the execution of the experiment. Water-tank and the tilt sensor were fixed at a constant inclination of 6° in the *x-z* plane during the test. Temperature of the water inside the bath was first raised to 56°C. Water was then allowed to cool down to the room temperature (19°C). The wavelength separations, $\Delta(\lambda_2-\lambda_1)$ and $\Delta(\lambda_4-\lambda_3)$ were measured at regular intervals during the water cooling process. Figure 3.6 shows the thermal response of the sensor. As can be seen from the experimental

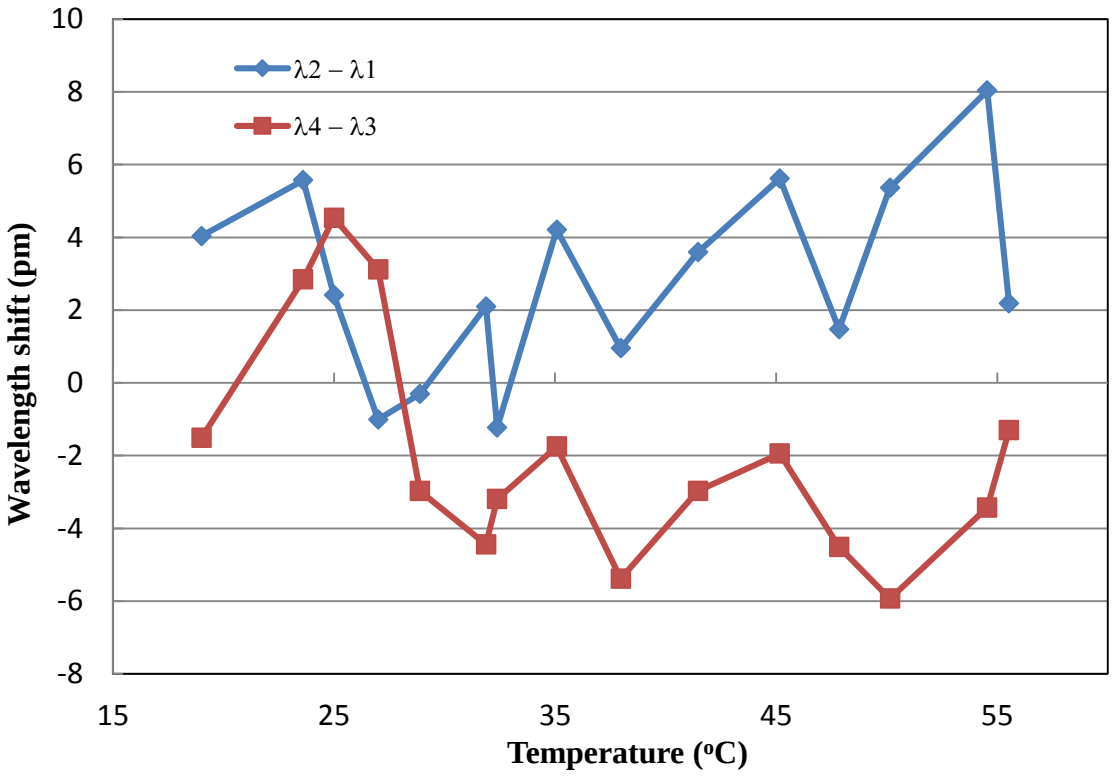

Figure 3.6: *Thermal response of the tilt sensor depicting the change in the wavelength separation of the FBG tilt sensor when it is fixed at a constant inclination of 6° in the x-z plane.*

results in Fig. 3.6, observed maximum discrepancy in the wavelength shift is less than 9.2 pm. This discrepancy is observed to be much smaller (46 times less) than the absolute wavelength shift of a single FBG under an identical temperature variation conditions. A very low temperature cross sensitivity establishes the fact that the proposed tilt sensor methodology eliminates the temperature cross talks substantially, and thus, results in a temperature independent tilt measurement. Owing to this feature, proposed sensor qualifies suitably for a real field application where temperature fluctuations cannot be avoided. In addition, an effective and stable sensing capability of the proposed non-pendulum type all-optical tilt sensor depicted by its relatively better accuracy, maximum discrepancy and angular resolution; along with good sensitivity and reversible as well as very reliable response characteristics make the proposed sensor of great practical importance.

3.4 Conclusion

This chapter described the development of FBG based tilt sensor employing a non-pendulum type design strategy. Employing this design strategy to map tilt in strain domain negates the possibility of any inherent friction and the limiting effects within mechanical structures. Sensor is observed to be capable of resolving magnitude as well as the direction of inclination from horizontal strategically more effectively and without any inherent instability. This is reflected in a relatively better resolution (better than 0.004^{o}), a better accuracy (~ $\pm 0.05^{o}$) and least maximum discrepancy (~ ±0.001 nm) during the forward as well as the reverse tilt. Theoretically, the sensitivity of the proposed sensor is observed to be proportional to the half of the mass employed in the sensor design. Sensitivity of the order of 0.012 nm/^{o} is achieved while employing a comparatively smaller mass. It is observed that a far better sensitivity, in comparison to the highest sensitivity reported in the literature, can be achieved by suitably employing an equivalent mass in the proposed design. Importantly, sensor response is

characterized with a very high degree of reversibility and repeatability over the experimentally exploited dynamic range of -10º to 10º (limited by the range of available goniometer); nevertheless, sensor is capable to measure tilt in the range of -45º to +45º. After successful development of FBG based tilt sensors, addressing various challenges towards its response characteristics, next chapter of the thesis explores the possibility of developing FBG based sensor to monitor vibration – another very important parameter in SHM.

Chapter 4

Temperature Insensitive Fiber Bragg Grating Based Two Dimensional Vibration Sensor For Structural Health Monitoring

4.1 Introduction

Measurement of structural vibrations induced by instantaneous impacts or natural environmental perturbations is a critical issue, particularly in civil engineering applications and rail transport network to name a few. Response of any given structure to such vibrational perturbations depends on the natural frequency of such structures, which is dictated by their physical properties. Often, a decrease in its value results in a damage proliferation [73]. Damage identification and prevention of its evolution in any civil engineering infrastructure, thus, becomes an integral part of structural-health-monitoring (SHM). Vibration measurement analysis is a vital approach to implement SHM strategies. Vibration sensors such as accelerometers are one of the key smart-diagnostic systems to study the impact of vibration perturbations in this strategy. Realizing low-cost and reliable vibration sensor system is quite challenging. A temperature insensitive, simple, compact, highly sensitive vibration sensor with a capability to resolve any arbitrarily directed vibration perturbation would be of extreme importance. Conventional vibration sensors are electronic in nature as they exploit either piezoelectric or capacitive effects. However, inherent limitations such as vulnerability towards electromagnetic/radio-frequency interference (EMI/RFI) and inability towards multiplexing and remote-sensing make such sensors impractical for real-field applications. On the other hand, optical fiber sensing technology has shown great potential to overcome the difficulties associated

with these conventional sensors. Owing to their inherent merits several kinds of optical fiber sensors have been developed over the last two decades for many real-field applications and especially for SHM [127]. In particular, several research efforts have been made to develop optical fiber vibration sensors. These efforts mainly employed cantilever based mechanism where the vibration is encoded in terms of uniaxial misalignment between two similar or different kinds of optical fiber [76, 77, 128]. A more complicated sensing scheme that integrated Moiré fringe with fiber optics is reported in [78]. Recently, a variety of optical fiber vibration sensors exploiting interferometric techniques have been reported [79, 80]. However, performance of all these optical fiber vibration sensors which are based on the intensity modulated scheme suffers from the source power fluctuations. Also, these sensors are unfit for multiplexing and distributed sensing. Importantly, being one-dimensional, they are unable of resolve arbitrary vibrations. On the other hand, optical fiber Bragg gratings (FBGs) have attracted considerable amount of research interests over the past few years. A range of FBG sensors have been reported for monitoring various parameters of practical importance and interest for science/engineering applications such as strain, pressure, displacement, curvature, tilt etc. [127]. Some attempts have also been made to develop FBG based vibration sensors. For example, Berkoff et al. in [82] embedded FBG element into a thin layer of elastomer between a rigid base and a seismic mass. Sensor suffered seriously from the cross-axis response. Zhou et al. in [84] employed vibration induced chirping mechanism of a surface loaded FBG. Such power-referenced sensing scheme suffers from light source power fluctuations and is unsuitable for distributed sensing. Weng et al. in [85] employed a very complicated sensing structure based on a U-shaped rigid cantilever beam, a diaphragm and a FBG fixed between the two legs of the cantilever beam. Researcher in [86] reported another diaphragm based sensor employing a

centrally attached inertial mass and the FBG. Another sensor design based on a tapered fiber and tilted FBG was employed in [87]. In another attempt, Stefani et al. employed microstructured polymer optical fiber Bragg grating to capture vibration/acceleration [89]. Temperature cross-talk, cross-axis sensitivity and complexity in designing remained some of the serious issues with all these sensors reported in the literature. Importantly, being uniaxial, they are incapable of resolving the impact to two-dimensional vibration perturbations. In order to address the later issue and to develop two-axial sensor, Fender et al. employed mass loaded multicore optical fiber carrying FBG in all the four cores of the fiber [90]. However, fabrication of such complicated structure required high level of sophistication and increased the experimental difficulty.

The objective of the research reported in this chapter is to design and construct a simple, compact, all-optical FBG based two-dimensional temperature-insensitive vibration sensor by employing chirp-free strain tuning mechanism. Sensor design employs four FBGs that are fixed onto the two sets of a pair of thin parallel plates, each carrying centrally fixed concentrated mass element. Design strategy insures a chirp-free Bragg grating response. Performance characteristics for the design strategy of the proposed sensor are first modeled using a 3-D CAD model and finite element analysis using ANSYS software. Afterwards, a rigorous experimental investigation is carried out to characterize the sensor. Sensor is excited with an electromechanical shaker over a frequency band ranging from 10Hz to 350Hz with varying accelerations from 0.65m/s^2 to ~70m/s^2. The response of the reported sensor is observed to be in good agreement with the applied signal with an excellent capability of successfully resolving the impact to two-dimensional vibration perturbations. Frequency response of the sensor is also analyzed to determine the natural frequency of the sensor. Further, in the proposed scheme, imprinting of the vibration perturbations in the optical domain is achieved by decoding the

vibration information from the peak wavelength separation between the two FBGs. This wavelength based optical diagnosing mechanism makes the proposed sensor temperature insensitive.

4.2 Experimental

4.2.1 Sensor Design and Construction

The design strategy of the proposed sensor is depicted in Fig. 4.1. The design consists of two identical trapezoidal units A & B, four identical flexural beams and two identical seismic masses

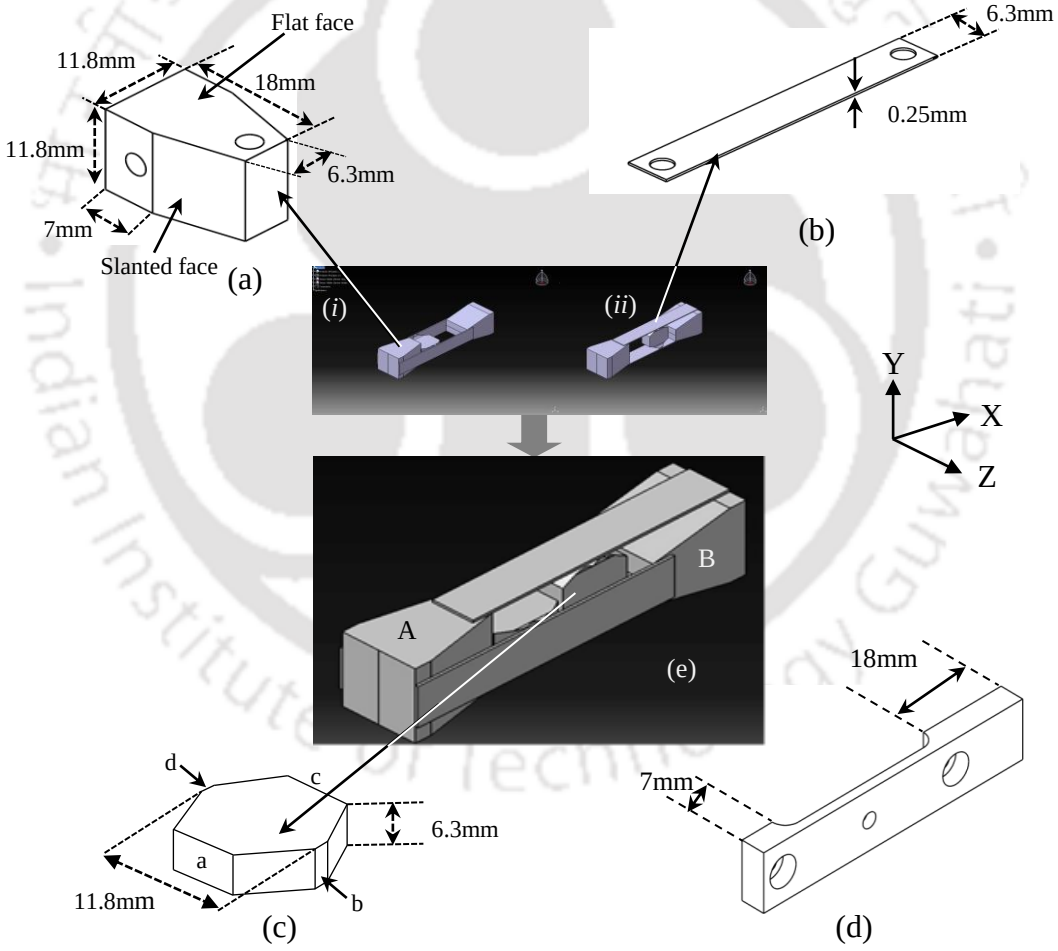

Figure 4.1: *Design strategy of the proposed sensor: (a) trapezoidal unit, (b) sensing plate (c) seismic mass, (d) casing and (e) complete sensor structure.*

along with the casings. In order to make the trapezoidal units, two rectangular blocks of brass having the dimensions as 18mm×11.8mm×11.8mm were used. Two prism shaped portions (height 11mm, base 2.75mm and width 11.8mm) were removed from the two parallel faces of these blocks, leaving a flat surface of height 7mm and a slanted surface of height 11mm as shown in Fig. 4.1(a). Four identical stainless steel (SS304 grade) flexural beams (Fig. 4.1(b)) of elsewhere [88] optimized dimensions 45mm×6.3mm×0.4mm were machined afterwards. Further, to design the seismic mass, two hexagonal shaped blocks of brass with a height of 12mm and thickness of 6.3mm were used. Sharp edges at the two diagonally opposite points were polished to make 0.3mm flat surfaces (b & d). In its final shape depicted in Fig 4.1(c), height between "b" and "d" points is 11.8mm. In this design, the width of the seismic mass matches the width of the flexural beams. Owing to this dimensional constraint, the maximum mass possible for this design was restricted to 3.358gm. Afterwards, each seismic mass was rigidly fixed between the two pairs of parallel flexural beams separately. While fixing the seismic mass in between the two parallel flexural beams, proper care was taken to match the width of the seismic mass with the width of the flexural beam. Also, hexagonal faces of the seismic mass (and hence, the two surfaces "a" and "c") were kept exactly perpendicular to the flexural beams with the two opposite edges (b & d) residing exactly in the middle of the beam's length. In order to rigidly fix two sets of flexural beam & seismic mass combinations to the trapezoidal units, four stainless steel casing units (Fig. 4.1 (d)) of dimensions 60mm×11.8mm×5mm, having 6mm threading hole at the centre along with the two other 3 mm holes, were machined. Next, the free end at one side of one set of the flexural beam & seismic mass combination was inserted along the slanted faces of the trapezoidal unit 'A' and rigidly fixed to it using the two casing units and 3mm screws. In this arrangement two flexural beams were in vertical plane (X-Y plane) and the hexagonal mass

was in horizontal plane (X-Z plane). In an identical ways, the free end at one side of the other set of the flexural beam & seismic mass combination was rigidly fixed to the trapezoidal unit 'B'. Now, structure with unit "B" was kept to the right side of the structure with unit "A" such that the free end of the flexural beams of both the unit faced each other. Importantly, structure with unit "B" here was oriented in a way that the two flexural beams were in the horizontal plane (X-Z plane) leaving the hexagonal mass in the vertical plane (X-Y plane). In this way, two trapezoidal units "A" & "B" were oriented normal to each other and so were the two seismic masses (Fig 4.1 (i) & (ii)). The two structures were then inserted into each other and joined together to form a closed structure by rigidly fixing the free ends of the flexural beams to the flat faces of other trapezoidal unit (Fig 4.1 (e)/inset of Fig (4.4)). In this arrangement, (a) the free length of the flexural beam between the two clamping points was 35mm, (b) seismic masses remained at the center of the free length of the flexural beams and (d) a pre-calculated gap was maintained between the two seismic masses. Importantly, the proposed sensor design offers the flexibility of varying the aspect ratio and/or the stiffness of the flexural beams in order to vary the natural frequency of the vibration sensor, thus tuning the sensitivity and frequency response ranges to suit a particular application.

Afterwards, four FBGs were to be fixed onto the outer surfaces of the four flexural beams. Before doing so, it's important to analyse the behaviour of the developed structure. Exposing this mechanical structure to the outside sinusoidal vibrations along Z-axis/Y-axis, sets the seismic mass confined in X-Z/X-Y plane in oscillation along the direction of vibration, whereas the seismic mass confined in X-Y/X-Z plane (normal to the direction of vibration) remains static. The oscillating seismic mass exerts a synchronized force in the perpendicular direction on the

pair of beams which are attached to it. As a consequence, beams in this pair will get bent. This leads to a varying strain distribution across the surface of each of the beam. In this synchronized oscillating pair of beams, at a given instant the outer surface of the one beam is elongated, whereas the outer surface of the other beam is compressed. Generated strain profile on the outer surfaces of the flexural beams gets transferred to the FBGs that are to be fixed onto these surfaces in the proposed design. In order to insure a chirp free sensing mechanism, peak wavelength of the reflection spectra of the FBGs should get tuned in accordance to the oscillation against the applied vibration perturbation, keeping the full-width-at-half-maximum (FWHM) constant. To realize this, varying strain generated over the surface of the oscillating beams must always remain uniform across the location of the FBG. To investigate the strain profile along the flexural beams for various amplitudes of vibration, a 3-D CAD model for the proposed sensor was built in ANSYS software. The model was simulated numerically using finite element (FE) based software ANSYS 13.0. While modeling the mechanical behavior of the vibration sensor, characteristic material parameters were required for each constituting elements of the sensor. For the trapezoidal units and seismic masses, which were made up of brass material, values of density, Young's Modulus and Poisson's ratio were 8.5 g/cm^3, 100×10^{10} Pascal and 0.34 respectively. For the flexural beams, which were made up of stainless steel, values of these parameters used were 8.0 g/cm^3, 193×10^{10} Pascal, and 0.29 respectively. Since the design was irregular, free meshing operation was selected. The suitable element type such as solid187 is assigned for modeling of the finite element irregular mesh. The generated mesh for the 3-D model is shown in Fig. 4.2. The element size is 0.2mm and the total number of elements in mesh is 271843. Once the meshing was done, sinusoidal force was applied along the Y-axis on the developed model. This force displaced the hexagonal mass from its mean position, which in

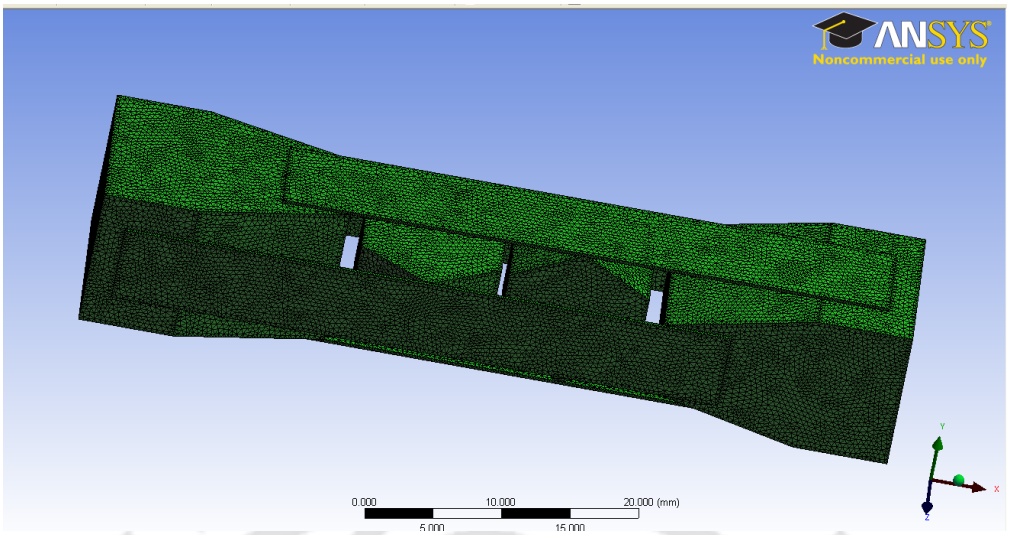

Figure 4.2: *Generated Mesh for the 3-D ANSYS model.*

turn, exerted force and varied strain along the attached beams. Strain profile on the beams was investigated by applying different magnitudes of force. Each case was solved in ANSYS for 10 iterations. As an example, simulated strain profile along the flexural beams that is confined in X-Z plane and attached to the seismic mass is shown in the Fig. 4.3 for an applied Y-directional vibration force of 20N. Blue color zone depicts the region of zero strain whereas the red color zone depicts the region of maximum strain. As observed from the simulated strain profile, strain is maximum at the center of the pairs of the flexural beams. Further, it's the central region of ~2.424mm length (red colored region in Fig. 4.3) along the beam surface where the strain is uniform across. Strain response across the surfaces of cross axis pairs of flexural beams (confined along X-Y plane) was observed to be zero. Entire process was repeated afterwards for the vibration force confined along the Z-axis. Similar observations were made for this case too. Thus, to insure a chirp-free sensing mechanism, (a) FBG length should not exceed the length of the uniform and maximum strain distribution across the flexural beam, and (b) FBGs should be

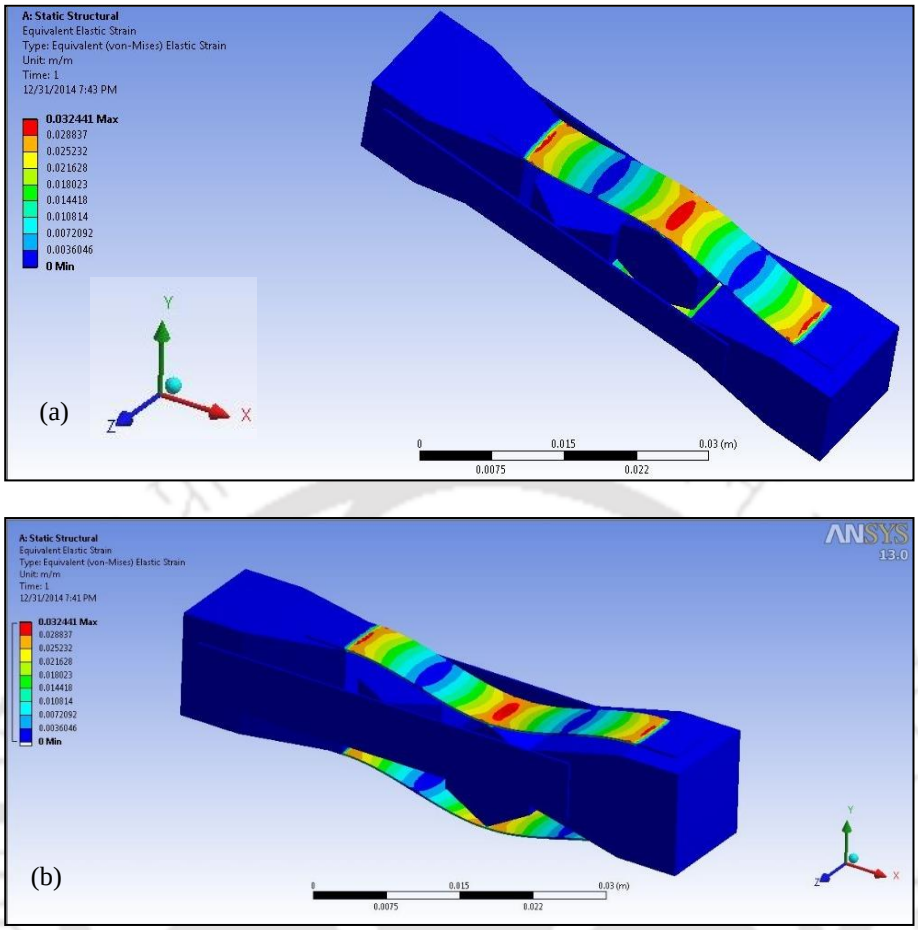

Figure 4.3: *Results of finite element strain analysis by ANSYS for the pair of flexural beams when force is applied along the Y-axis (a) top view and (b) side view*

fixed onto the flexural beams at this central region of length ~2.424mm where the strain is uniform and maximum [129].

4.2.2 Sensor characterization

Four FBGs, each of 3mm length and written onto a hydrogen-loaded single-mode optical fibers using phase-mask technique were used in the sensor strategy. Owing to the laboratory constraint, FBG with a length shorter than 3 mm could not be written. The peak reflection wavelengths of

these FBGs were 1550.172 nm (FBG1, λ_1), 1550.235 nm (FBG2, λ_2), 1554.071 nm (FBG3, λ_3)

Figure 4.4: *Experimental set-up for the characterization of proposed optical fiber vibration sensor. Inset shows the proposed sensor.*

and 1554.134 nm (FBG4, λ_4). These four FBGs were fixed by epoxy resin onto the outer surface of the four flexural beams of the sensor structure at the location which was expected to have uniform strain profile. In this arrangement, FBG1 and FBG2 were with the flexural beams confined in the X-Y plane, whereas FBG3 and FBG4 were with the flexural beams confined in the X-Z plane. The sensor was mounted on a vibration shaker (PM Vibration Exciter Type 4808 from Brüel & Kjær) as shown in Fig. 4.4. Brüel & Kjær generator module (Type 3107) was interfaced with a computer via PULSE software (Brüel & Kjær Noise and Vibration Analysis Type 7700). The signal from generator module was fed to the power amplifier (Brüel & Kjær Type 2712). The amplified signal was then fed to the shaker. A standard reference accelerometer (Deltatron Accelerometer Type 4396) attached to the shaker was connected to a computer

through a PULSE analyzer software (Brüel & Kjær Type 3560D). A sine wave signal with varying frequencies and accelerations were applied to the shaker during the characterization process, and the response of the proposed FBG sensor was then recorded. To enable this, fibers carrying FBG were connected to a high speed interrogation system (Micron Optics, SM-130). This system converted the optical signal (instantaneous Bragg wavelengths) to electrical signal and transferred it to the computer for data processing. The entire set-up is shown in Fig. 4.4.

4.3 RESULTS AND DISCUSSION

If the proposed vibration sensor is subjected to the sinusoidal oscillations in one direction (say, along Z-axis) the pair of flexural beams which are perpendicular to the plane of vibration (X-Y plane) will start oscillating. Both the plates of this pair will oscillate in the same phase due to the force generated by the inertial mass. This causes bending of the beams and in terns, strain variation across the surface of the flexural beam. Set in oscillation (and hence, bent), the outer surface of one of the beam gets elongated whereas the outer surface of the other beam in this pair gets compressed. As the FBGs are fixed on the outer surfaces of the beams in this pair, one FBG gets elongated whereas the other FBG gets compressed. This causes a drift of the individual central wavelengths in the opposite direction for both the FBGs. It is this wavelength shift in the reflection spectra of FBGs which is instantly, independently and dynamically monitored through the interrogating system. Importantly, taking the wavelength difference of these two FBGs makes sensor temperature insensitive. Other two beams, parallel to the plane of vibration (in X-Z plane), will not be deflected. Thus, Bragg wavelength difference of the corresponding two FBGs defining the cross axis response would be zero. Same is true when the proposed sensor is subjected to the sinusoidal oscillations in other orthogonal direction (Y-axis).

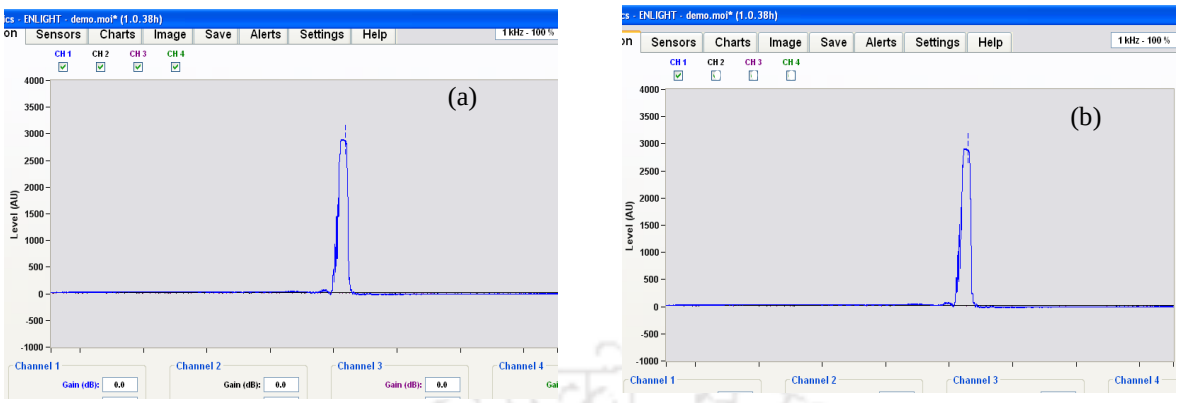

Figure 4.5: *Measured reflection spectra of FBG1 (λ_1) when pair of flexural beams experiences (a) zero force and (b) a finite force.*

Before characterizing the response of the sensor, experimental verification of chirp-free mechanism was carried out. For this, one pair of beams carrying seismic mass at the center and fixed at one end to the trapezoidal unit with FBGs glued on the outer surfaces was used. Bending force was manually applied at the free end of the beams in this pair. Reflection spectra of the FBGs were then recorded. As an example, Fig. 4.5(a) and 4.4(b) depict the reflection spectra of one of the FBG (λ_1) before and after the application of the force. As can be observed from these figures, FWHM remained almost unchanged, which endorses the realization of chirp-free wavelength tuning mechanism.

Next, the dynamic characteristic of the FBG based vibration sensor was examined through a series of shake-table tests by exposing the proposed sensor to sinusoidal vibrations at different frequencies and varying accelerations (maximum and minimum values for both were limited by the electronic shaker). For this, pure sine wave is selected as the input signal for testing the sensor performance, where the excitation amplitude (acceleration) of the applied sinusoidal

signal varied from 0.65 m/sec^2 to ~70 m/sec^2 (which is captured by piezo-electronic accelerometer) and the frequency varied from 10Hz to 350Hz. Wavelength response of the four FBGs were recorded at a full-speed sampling rate of 2 kHz. In the first part of the performance characterization, proposed sensor was subjected to the sinusoidal vibrations in the vertical plane (X-Y plane). Keeping the frequency of the applied signal fixed at 10Hz, amplitude (acceleration) of the sinusoidal signal was varied from 0.65m/sec^2 to ~70 m/sec^2. Sensor response was recorded for every amplitude-frequency combinations. Experiment was repeated afterwards for other fixed frequencies such as 30Hz, 50Hz,…, 350Hz etc. where amplitude (acceleration) of the signal was varied once again in the range described above. It's important to mention here that owing to the limitation of the shaker (vibration exciter Type 4808), experiments with acceleration greater than 50m/sec^2 could not be performed for the higher frequency range (above 100Hz). In the other part of characterization, experiments were repeated while subjecting the sensor to the sinusoidal vibrations in the horizontal plane (X-Z plane).

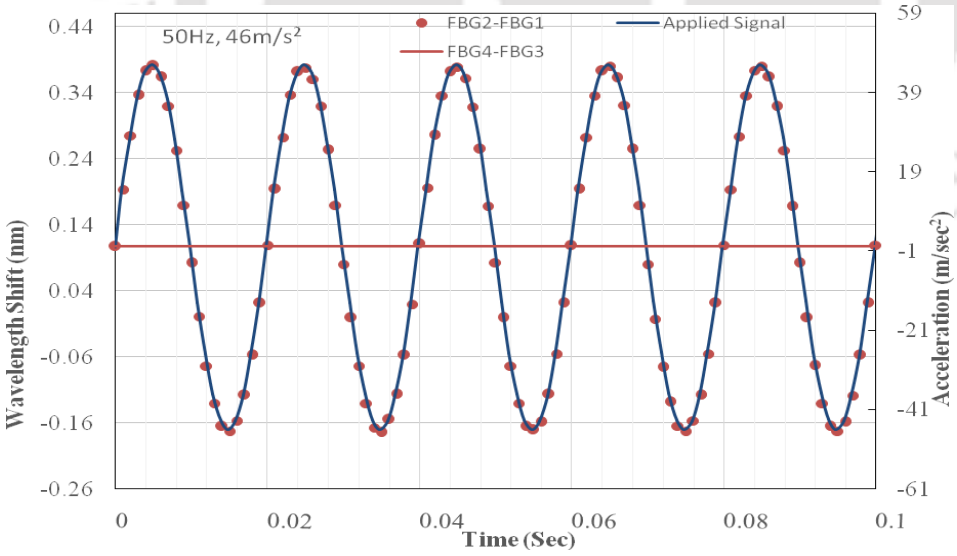

Figure 4.6: *Typical time response of the vibration sensor for acceleration-frequency combination of 50Hz-46m/s^2.*

A typical temperature compensated response $\Delta(\lambda_2 - \lambda_1)$ (dots in the figure) and the corresponding cross axis response $\Delta(\lambda_4 - \lambda_3)$ (red continuous line in the figure) is depicted in Fig. 4.6 as an example, when a signal of 50Hz–46m/s^2 frequency–acceleration combination is applied to the proposed FBG sensor in X-Y plane. In order to investigate the response of the proposed FBG sensor more thoroughly, applied sinusoidal signal is also plotted in Fig. 4.6 (blue continuous line), which corresponds to the vertical axis that is in the right side of the plot. As can be observed from this figure, proposed prototype FBG sensor followed the applied signal extremely well, depicting a great capability of sensing vibrations at this frequency–acceleration combination. Further, shift in the Bragg wavelength difference, $\Delta(\lambda_4 - \lambda_3)$, for the cross-axis response is observed to be zero, which is in accordance to the ANSYS analysis. In order to rigorously investigate the response of the proposed sensor, time response at other frequency–acceleration combinations must also be analyzed. Fig. 4.7 depicts typical temperature compensated responses, $\Delta(\lambda_2 - \lambda_1)$ (blue color), along with the corresponding cross axis response, $\Delta(\lambda_4 - \lambda_3)$ (red color), for the signals of varying frequency–acceleration combination that are applied in the X-Y plane. In this figure, horizontal graphs depict the sensor response for varying accelerations at constant frequency, whereas vertical graphs in each column depict the sensor response for varying signal frequencies at different accelerations. Following observations can be made from these figures: (a) proposed prototype sensor responds very well for all the frequency–acceleration combinations, with acceleration as low as 0.695 m/s^2 to as high as 71.4m/s^2 while frequency varying in 10Hz–250Hz range; thus, depicts a great capability of sensing vibrations at various externally applied signal frequencies and amplitudes (accelerations), irrespective of the fact whether they are low or high; (b) at a fixed acceleration

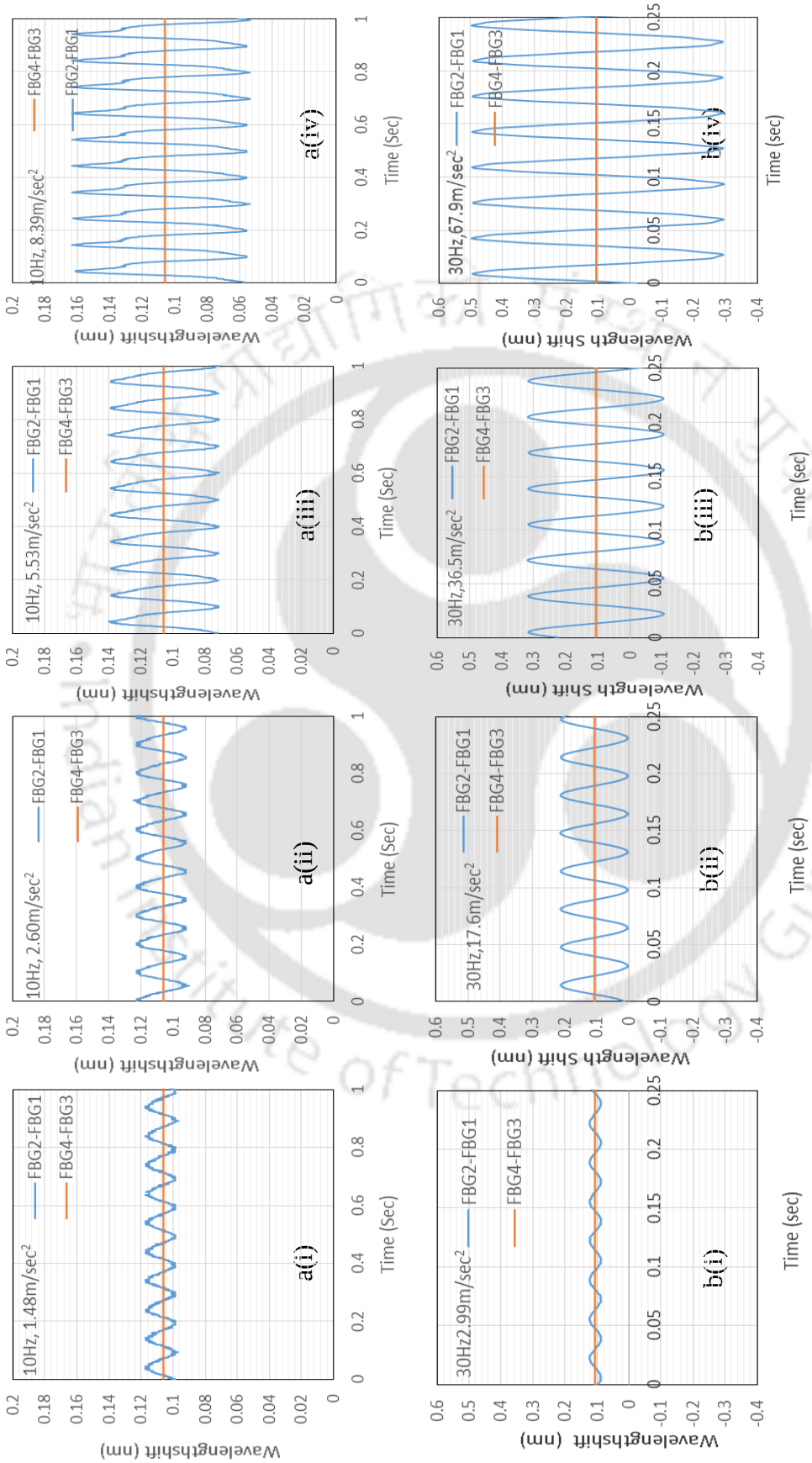

Figure 4.7: *The time response of the vibration sensor for varying acceleration-frequency combinations. Frequency varied as (a) 10Hz, (b) 30Hz, (c) 50Hz, (d) 75Hz, (e) 100Hz, (f) 125Hz, (g) 150Hz, (h) 175Hz, (i) 200Hz, and (j) 250Hz in each, whereas acceleration varied in (i), (ii), (iii), and (iv) as depicted in the figure.*

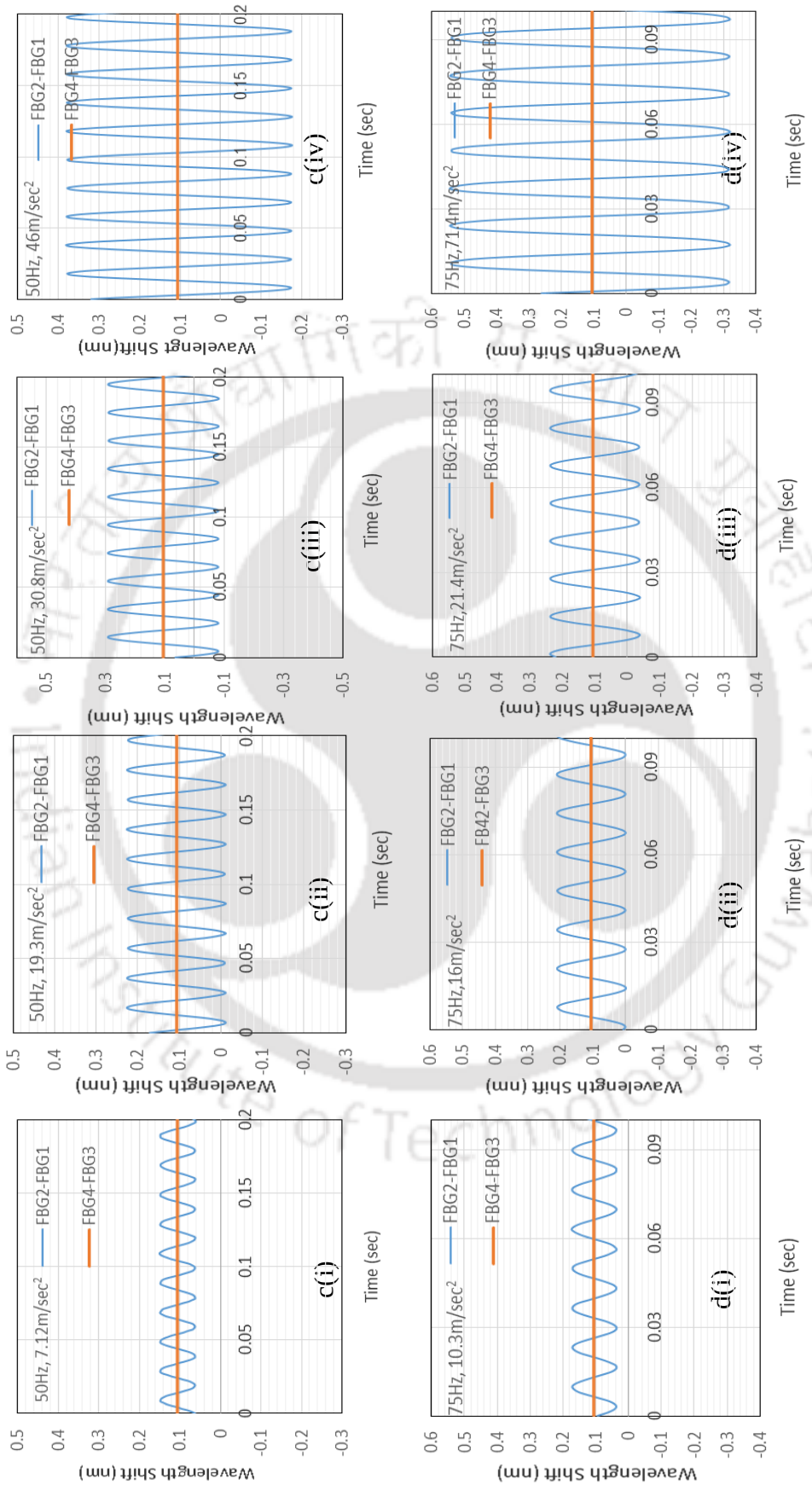

Figure 4.7: *Continued…*

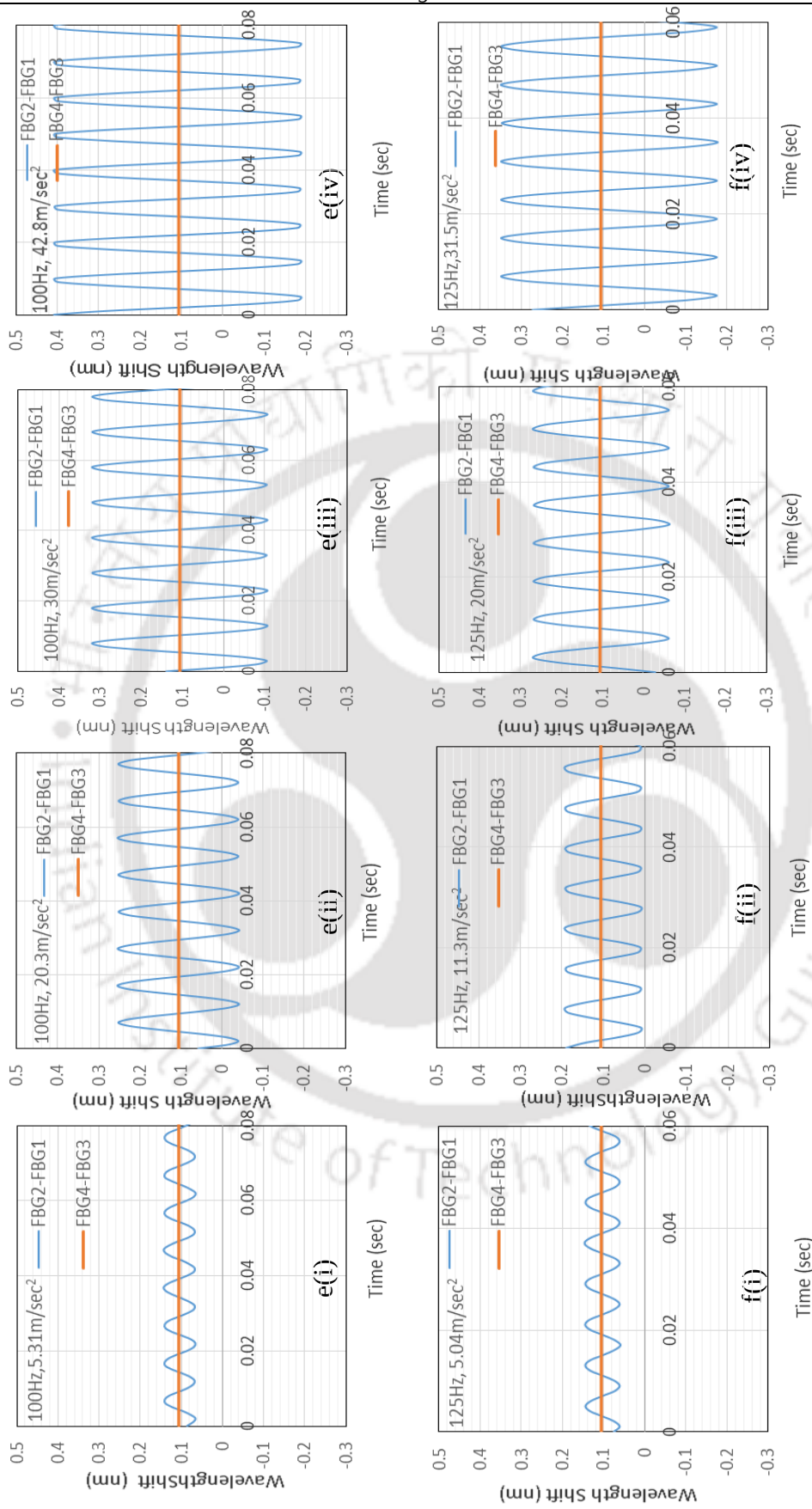

Figure 4.7: *Continued…*

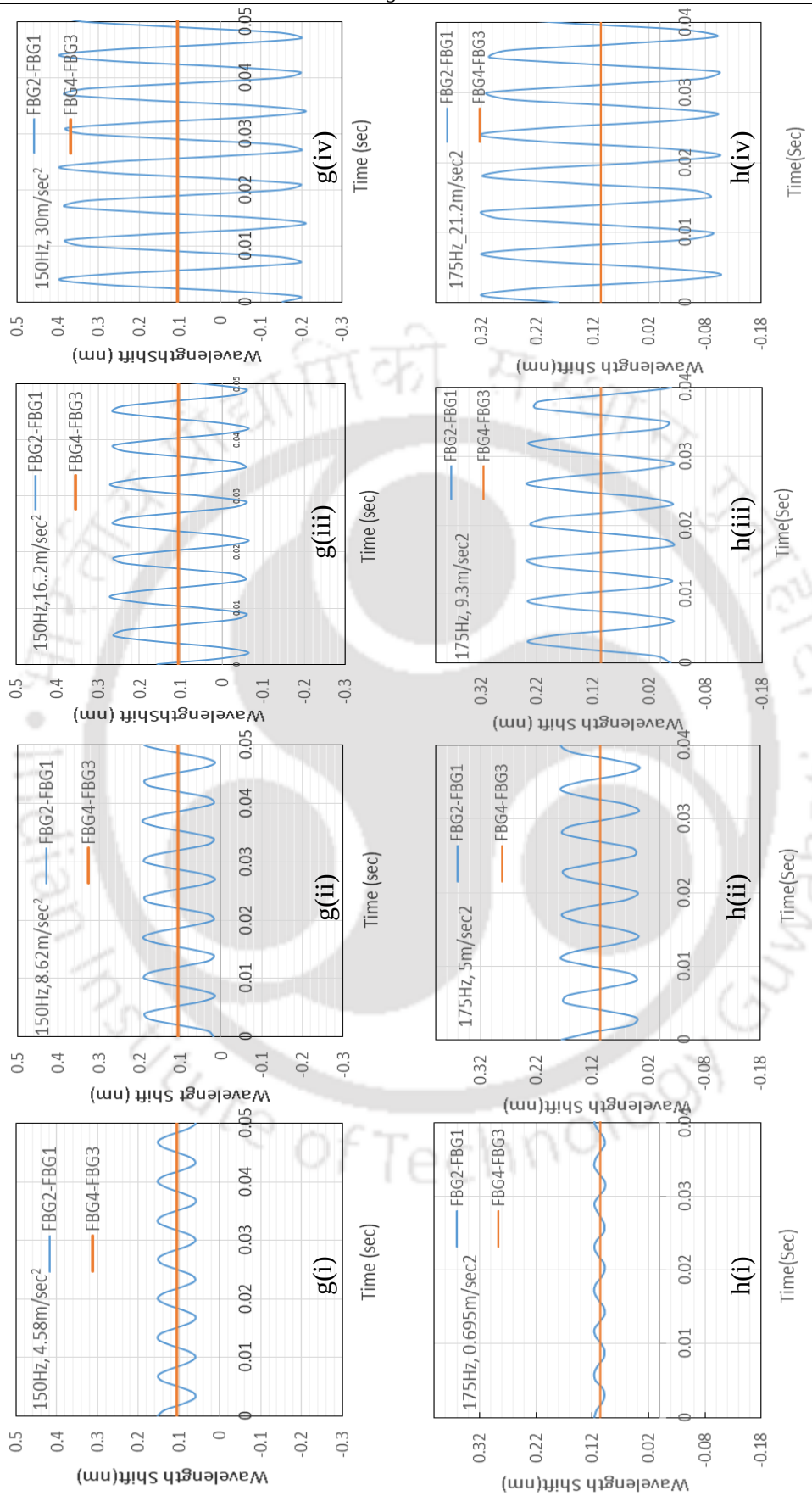

Figure 4.7: *Continued…*

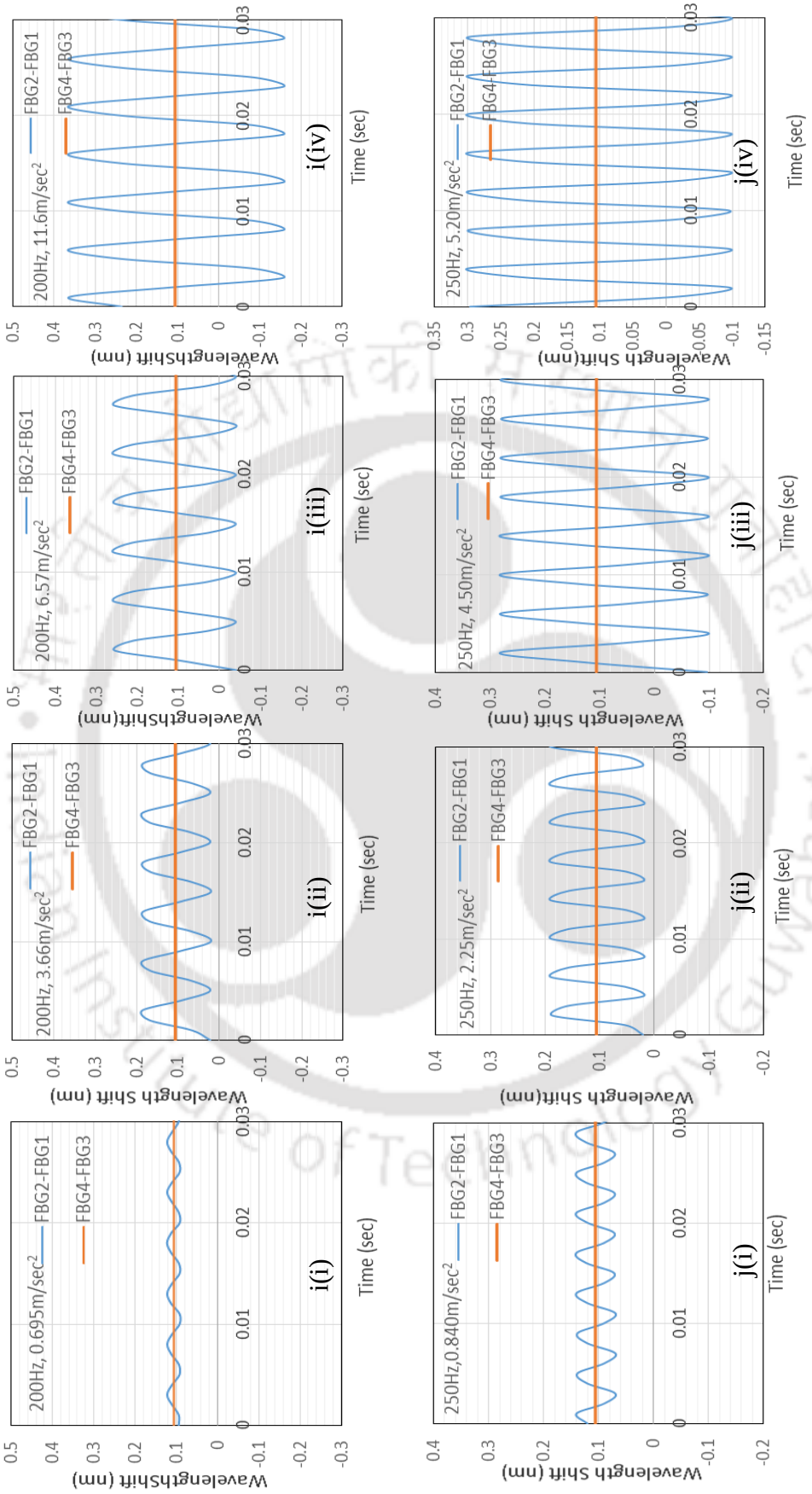

Figure 4.7: *Continued…*

(as an example of, say ~5m/s^2) sensor response was little distorted for low frequency signal (10Hz); (c) increasing the frequency of the applied signal beyond 25Hz, sensor captures the applied vibration perturbations extremely well without any significant distortion from sinusoid response characteristics for all frequency–acceleration combinations, irrespective of the fact whether acceleration is low or high; (d) shift in the Bragg wavelength difference, $\Delta(\lambda_4 - \lambda_3)$, for the cross-axis response is observed to be zero for all these cases, which is, as mentioned earlier, in accordance to the ANSYS analysis. Similar results are obtained for the vibration perturbations in the horizontal (X-Z) plane.

Before the response characteristics of the sensor is further analyzed, it's important to find out the natural frequency of the proposed FBG accelerometer. In order to find the natural frequency (and the frequency response) of the accelerometer, the signal generator that drives the shaker was set to frequencies continuously varying between 10Hz to 350Hz while vibration amplitude (acceleration) kept at a constant magnitude. As an example, Fig. 4.8 (a) shows the time domain response of the FBG based accelerometer over the frequency variations from 10Hz to 350Hz at a fixed acceleration of 0.0418 m/sec^2. Vertical axis depicts peak-to-peak Bragg wavelength shifts, $\Delta(\lambda_2 - \lambda_1)$. Though, frequency of the applied signal information cannot be observed from Fig 4.8. (a), it is continuously increasing from 10Hz to 350Hz with respect to the time. As can be observed from this figure, peak-to-peak Bragg wavelength shift is almost constant up to a certain frequency. Beyond, it increases and reaches to a maximum at a particular frequency of the applied signal. Afterwards, it decreases and attains once again the same constant value. The frequency at which peak-to-peak Bragg wavelength shift attains its maximum value is the natural (resonant) frequency of the sensor. In order to find the resonance frequency information from

Fig. 4.8 (a), the Fast–Fourier–Transform (FFT) for this signal was extracted using MATLAB. Figure 4.8 (b) shows the extracted FFT spectrum. As can be observed from Fig. 4.8 (b), peak-to-peak Bragg wavelength shift remains almost constant till ~150Hz, increases afterwards and over 225Hz starts increasing sharply and attains maximum. Afterwards, this shift decreases rapidly.

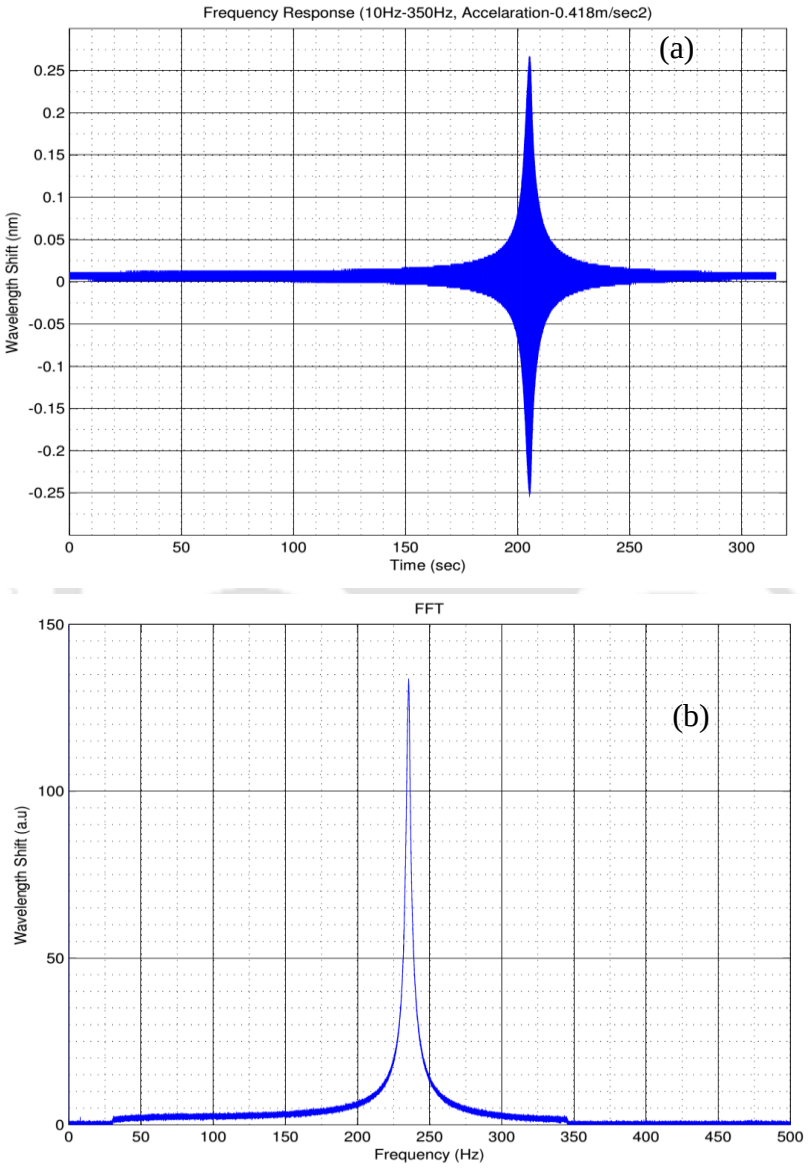

Figure 4.8: *(a) Time domain record of sensor, where frequency is varied from 10Hz to 350Hz at a constant acceleration; (b) Fast Fourier Transform (FFT) of the recorded signal.*

From the FFT spectrum, resonant frequency for the sensor that corresponds to the maximum peak-to-peak wavelength shift is observed to be 235.5Hz.

Coming back, in order to have deeper understanding of the response characteristics of the proposed FBG based accelerometer, peak-to-peak Bragg wavelength shifts, $\Delta(\lambda_2 - \lambda_1)$, for all frequency–acceleration combinations are obtained from Fig. 4.7. Keeping the frequency of the applied signal fixed, these experimentally observed peak-to-peak Bragg wavelength shifts are then plotted against the applied accelerations, which is depicted in Fig. 4.9. Following observations can be made from these results: (a) sensor shows linear response where maximum peak-to-peak wavelength shift, $\Delta(\lambda_2 - \lambda_1)$, increases linearly with the increasing amplitudes (accelerations) at all the frequencies of the applied signal; (b) sensitivity of the sensor remains

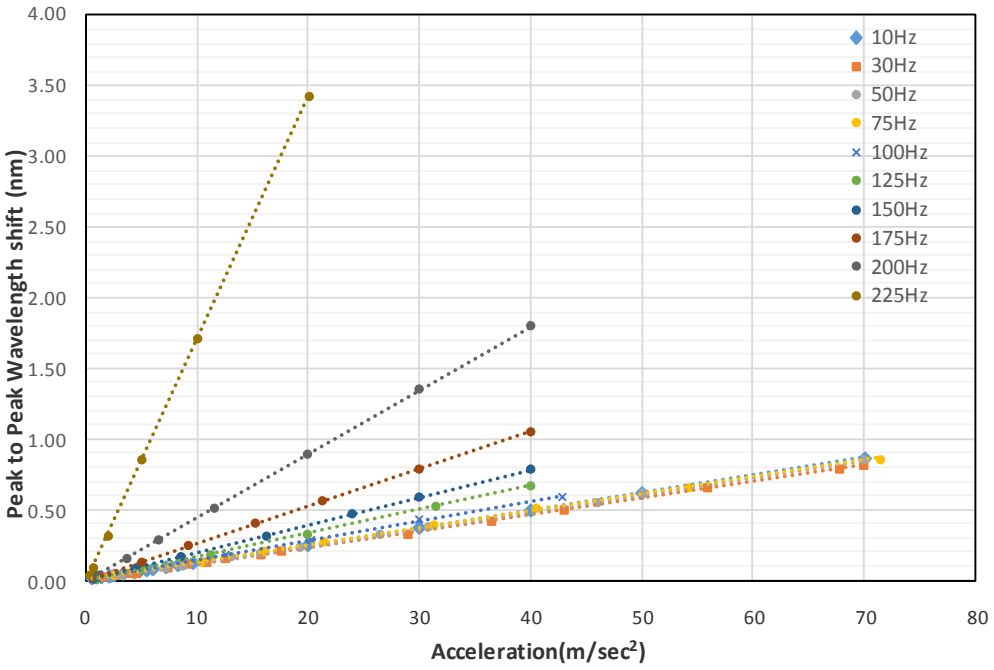

Figure 4.9: *Peak to peak Bragg wavelength response against applied acceleration for different frequency signals.*

almost constant for the excitation frequency range of 10Hz to 100Hz; (c) as the frequency of the applied signal approaches to the resonant frequency, peak-to-peak Bragg wavelength shift increases and the plot against the applied accelerations becomes steeper and steeper, resulting in a higher sensitivity. The reason for this behaviour is as follows: when the applied signal frequency is close to or equal to resonance frequency (235.5Hz) of the proposed sensor, even the small applied input acceleration gets coupled strongly with the mass. This results in the maximum bending of the flexural beams with greater strain localization in the FBG region and hence, maximum changes in the Bragg wavelength shifts. In the next part of analysis, the sensitivity of the accelerometer measured from Fig. 4.9 is plotted against applied frequencies in Fig. 4.10. As can be observed from Fig. 4.10, experimentally observed flat response range

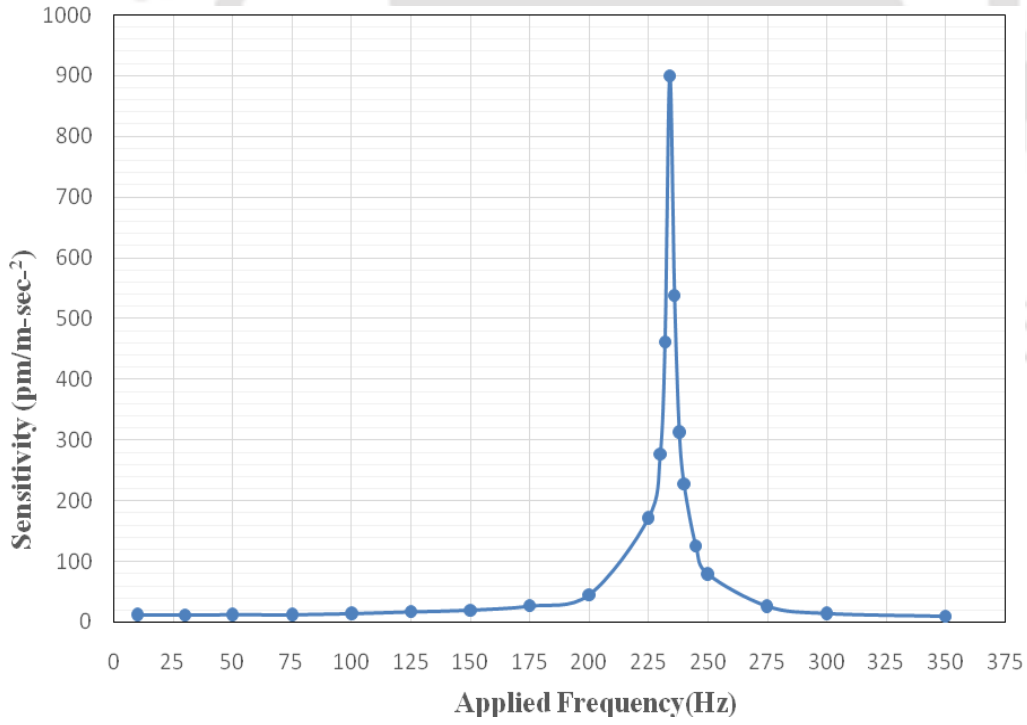

Figure 4.10: *Sensitivity characteristics of the proposed FBG accelerometer.*

(effective frequency measurement range) for the proposed FBG accelerometer is from 10Hz to 200Hz. Finally, it is important to mention that, the proposed sensor utilizes a very low seismic mass (3.358gm) in comparison to the one used in the literature that ranges from 20gm to 100gm. Use of a heavier seismic mass will increase the bending moment of the flexural beams, and that ways, will result in a large Bragg wavelength shift and a better sensor characteristics in terms of it's sensitivity, resolution etc. Thus, owing to the features such as simple in construction, compact (6cm×2cm×2cm with casing), temperature insensitive, all-optical, two-dimensional resolution ability with a very high capability of sensing an externally applied signal at various frequency–amplitude combinations with a frequency and acceleration as low as 10Hz and 0.695m/s^2 or as high as 350Hz and ~70m/s^2 respectively, proposed FBG based sensor is of great importance and a good candidate for real-field applications.

4.4 CONCLUSION

A simple, compact, temperature insensitive, two-axial all-optical vibration sensor employing four FBGs fixed over the two pairs of flexural beams that are joined together through the seismic mass is designed and demonstrated in the present work. 3-D CAD modeling and finite element analysis using ANSYS software are carried out to analyze the strain variation across the flexural beam and that ways, to analyze the response of the sensor against the applied vibration perturbations. Chirp-free strain tuning mechanism is exploited, which insures a proper execution of wavelength modulation scheme while characterizing the dynamic response of the sensor. A series of shake-table tests are conducted while varying the frequency from 10Hz to 350Hz and the amplitude from 0.65m/sec^2 to 70m/sec^2. Resonance frequency of the sensor is observed to be 235.5Hz. Proposed sensor exhibits an excellent capability of responding to the externally applied

signal at various amplitude and frequency combinations irrespective of the fact whether it is low or high with a very good sensitivity. After successful development of a temperature-insensitive FBG based vibration sensor, next chapter of the thesis explores the possibility of enhancing the strain sensitivity of FBG which would not only help to resolve strain in better ways but will also improve the response characteristics of all FBG based sensor that utilize the mapping of a given measurand in strain domain.

Chapter 5

Corrugated Fiber Bragg Grating Structure: Strain Sensitivity Enhancement

5.1 Introduction

With the diverse advancements in the global human civilization as well as in the science and technology that led to an unimaginable growth of civil infrastructures, synchronized structural-health-monitoring (SHM) becomes a serious issue to deal with. Any reason among (a) possible errors in design and construction, (b) overload, (c) environmental degradation and (d) nature's impact such as earthquakes imposes serious threat and induces adverse changes (damage/deterioration) in the health condition of various civil infrastructures such as bridges, dams, tunnels, high-rise buildings etc. A serious outcome of these reasons/effects is the accumulation of unwanted strain distribution across certain locations of the structures, termed as defect centers, which may finally lead to the collapse of such structures and hence, casualty to human lives. Thus, an accurate measurement of strain with a better strain resolution plays a crucial role in determining crack, damage, fatigue, vibration etc. during structural-health-monitoring [52]. In particular, a strain monitoring system with high sensitivity in addition to a high accuracy and optimum strain resolution is best suited to mitigate risks and prevents disasters at a very early stage of degradation. Conventional strain sensors as well as electronic strain gauges are based on the electrical properties of the sensing material, which transfer induced strain information into an electric signal [91, 92]. A reasonably good sensitivity can be achieved using such conventional sensors. Nevertheless, it's impossible to employ, in particular, the

immunity towards electromagnetic/radio-frequency interference, flexibility of multiplexing and remote sensing – essential features required for SHM. Optical fiber sensors not only overcome these disadvantages, but also offer a very high sensitivity towards an applied perturbation. Hence, optical fiber sensors have been extensively exploited for the measurement of various parameters of interest spanning a very wide range that includes but not limited to physical, chemical and biochemical parameters, to name a few [123]. Even being not very popular from the point of view of real–field application, a few optical fiber strain sensors have been reported in the literature. As an example, Arregui et al. in [93] reported an optical fiber strain gauge employing intensity modulation through the bending of a bi-conically tapered single-mode fiber. A sensitivity of ~0.02dB/με was achieved; however, intensity fluctuation of the optical source posed a challenging limitation. In another attempt to enhance the strain sensitivity, Li in [94] reported a fiber optic strain senor employing multimode interference in single mode–multimode–single mode fiber structure. Observed strain sensitivity was roughly 1.92 times the strain sensitivity of fiber Bragg grating (FBG).

A major thrust to all-optical sensing technology is witnessed with the invention of FBG [34]. Being inherently self-referencing with a capability of multiplexing large number of FBG sensors over a single fiber network, FBG sensors have emerged as a most viable and integral solution for SHM [130]. Owing to strain-optic/thermo-optic effects, FBG is inherently sensitive to temperature and strain perturbations both. One needs to device a smart mechanism to decouple strain or temperature information. Further, apart from strain and temperature, various other parameters (e.g., pressure, tilt, vibration, torsion, acceleration, displacement, flow etc.) are also required to be monitored in SHM as well as in other engineering applications and processes. In

order to develop FBG based sensors, these other parameters that are to be monitored are preferably mapped in strain domain. FBG fabricated in a standard telecom fiber offers a limited strain sensitivity of ~1.2 pm/με around 1550 nm wavelength. Limited (small) strain sensitivity of FBG not only affects an early prediction of the degradation of civil infrastructures but also dictates a limited sensitivity to FBG sensors for other parameters. Hence, devising a mechanism that can increase the strain sensitivity of FBG will not only meet the requirement of early prediction of degradation in SHM as mentioned above, will also increase the overall sensitivity of all FBG sensors employing strain-based mechanism. Recently, few attempts have been made to realize FBG strain sensor with enhanced strain sensitivity. For example, James et al. in [95] employed two slightly different FBGs on either side of the splice between two fibers of different diameters. While applying strain to this structure, FBG in reduced fiber diameter displayed greater strain sensitivity than the FBG in normal fiber diameter. A maximum strain sensitivity of 0.81 pm/με was achieved. Modifying the sensing structure of [95], Mondal et al. in [96] designed FBG strain sensor employing single FBG with a reduced fiber diameter over half of the length of the FBG. In agreement with [9], a strain sensitivity enhancement was observed with a very limited dynamic range of ~200 με. On the other hand, Fraz et al. in [97] devised a strain sensor formed by a single FBG in series with a fused fiber taper. Authors successfully demonstrated strain sensitivity tuning below the standard strain sensitivity of normal FBG. In another attempt to enhance the sensitivity, Ren et al. in [98] devised a strain sensor employing a single FBG with a specific gripper tube. A strain sensitivity enhancement by a factor of two in comparison to the strain sensitivity of normal FBG was achieved. Xu et al. in [99] employed chirped FBG in a tapered optical fiber to devise another strain sensor. A little better sensitivity in comparison to the normal FBG was observed. In another work, Gu et al. [100] devised a strain sensor

employing micro/nano Bragg grating structure in a polymer fiber, where a strain sensitivity of –2.5 pm/με (roughly double of the silica FBG) was achieved. On the other hand, specialty fibers are also exploited in order to design an all-optical strain sensor to improve the sensitivity. Dong et al. in [101] reported a temperature insensitive strain sensor based on Sagnac interferometer that employed 86mm long polarization-maintaining photonic crystal fiber (PCF). Observed strain sensitivity was 0.23 pm/με. In another attempt, a PCF Mach-Zehnder interferometer was realized inscribing pair of LPGs directly on a PCF [102]. A maximum strain sensitivity of –2.6 pm/με was achieved. However, in comparison to FBG based strain sensors, PCF interferometers are not competitive due to several centimeters length of the PCF and a high splice loss between Hi-Bi PCF and standard fiber. In order to increase the strain sensitivity, novel grating structures imprinted on a PCF were also exploited. For example, [102] also reported PCF based strain and temperature sensors, which were devised by fabricating long period gratings (LPGs) of different structural parameters in different types of PCF. Comparing the response characteristics of these different LPG-PCF based strain sensors, highest strain sensitivity observed was –7.6 pm/με. However, performance of these sensors was limited by power losses due to CO_2 laser induced collapse of air holes, non-periodicity and disorder of the refractive index modulation. Also, the feasibility of distributed sensing as well as simultaneous multi-parameter sensing with such PCF based sensors are yet to be investigated; whereas FBG sensors have also shown the advantage of multi-parameter sensing with a short length single FBG [103]. Thus, in all the attempts to enhance the strain sensitivity of FBG sensors, a maximum sensitivity that was roughly double of the standard FBG was achieved or otherwise, the dynamic range was very limited. Employing LPG–PCF sensing structure, though resulted in a good sensitivity, but had its own inherent limitations.

The main aim of the research reported in this chapter is to design a highly reliable optical fiber strain sensor employing a unique FBG sensing structure, which would not only be capable of enhancing strain-sensitivity manifold, but would also facilitate single FBG to act as multiple independent sensors. To achieve this objective, a specific corrugated structure is carefully carved out over an otherwise uniform FBG using controlled etching process. This structure is exposed to the applied strain perturbations. Employed design strategy facilitates a single FBG to split into multiple independent FBG sensing elements. Most striking feature of this study is a manifold strain-sensitivity enhancement. Strain sensitivity of a particular section of the corrugated structured fiber in the FBG region, which acts as an independent sensor, is observed to be over 10.5 times higher than the sensitivity of an unetched (uniform) FBG region. This is a remarkable enhancement of strain sensitivity and is achieved for the first time to the best of author's knowledge. Further, a maximum discrepancy of ±0.019 nm, strain resolution better than 0.0057με and a strain measurement accuracy of ~ ±2.15με are observed for this sensing structure. Experimental results also depict a highly reliable and reversible response characteristic for the proposed sensor.

5.2 Experimental

5.2.1 Sensor Design and Construction

The primary objective of the research reported in this work is to develop a reliable FBG based strain sensor with manifold enhanced strain sensitivity. To achieve this, FBG sensor with a corrugated geometrical configuration, as depicted in Fig. 5.1 (a), is structured and experimentally analyzed. In order to carry out a comprehensive comparative analysis, two

more geometrical configurations reported in the literature and depicted in Fig. 5.1 (b) and (c), are also structured. To develop these strain sensors, four Bragg gratings written in a

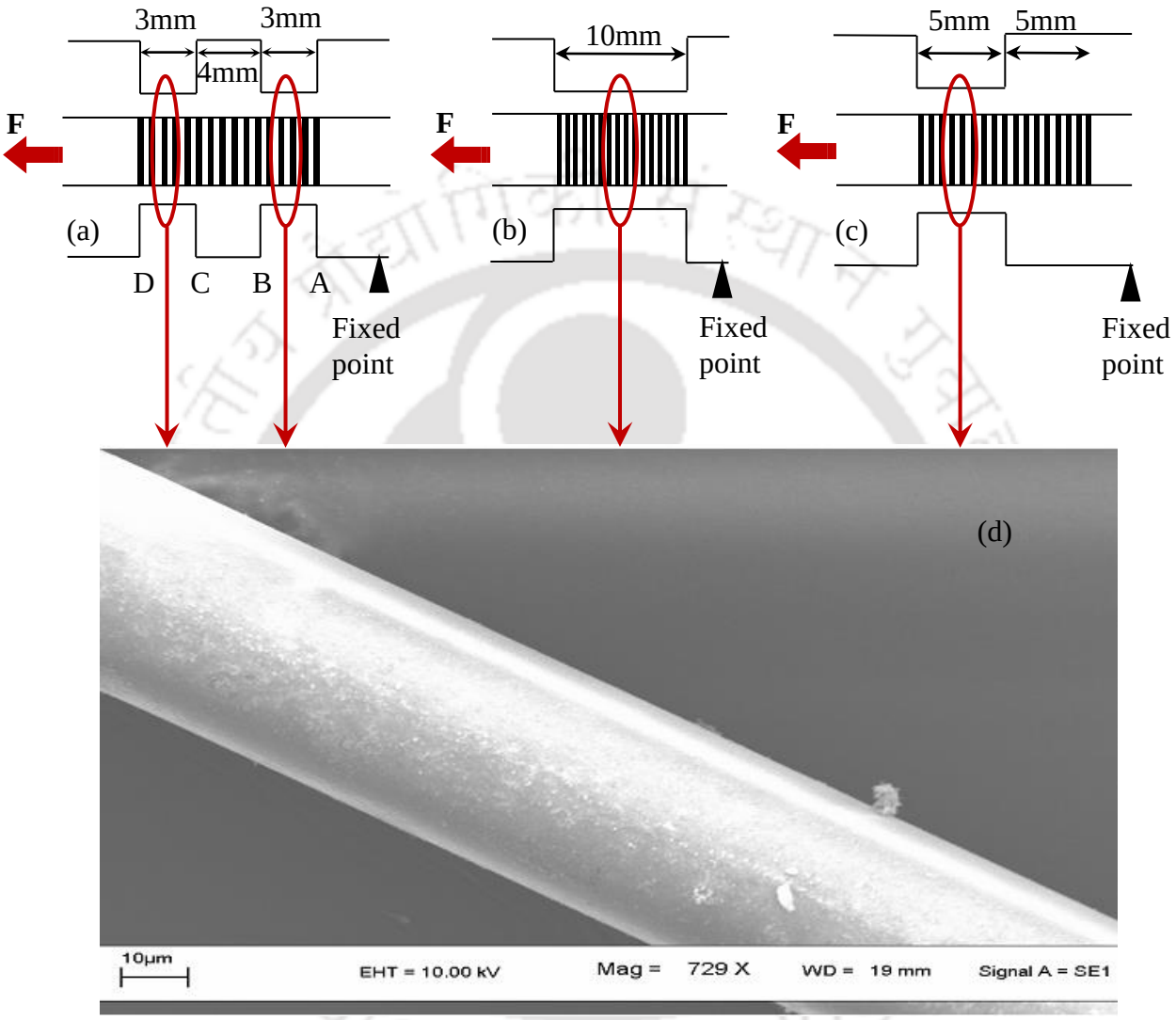

Figure 5.1: *FBG sensing configurations: (a) corrugated etched (b) fully etched & (c) half etched FBG along with schematics of applied strain perturbations, (d) FE-SEM image of the section of fiber, which was etched for 45 minutes.*

germanium doped silica single mode fibers (125 μm diameter, $E \approx 7.2\times10^{10}$ N/m^2, $A = 1.23\times10^{-8}$ m^2, $p_e \approx 0.22$) using phase mask technique were used. All FBGs were 10 mm long and had a peak wavelength of 1545 nm. As depicted in Fig. 5.1, geometrical configuration for the proposed sensor along with the other two configurations on the part of fiber carrying FBG was structured by the sequential reduction of cladding diameter. Cladding reduction was achieved using standard chemical etching procedure that employed 45% HF solution. Special etching chambers of perspex sheets were designed in order to realize the three sensing geometries. Portion of the fiber carrying FBG was inserted inside a chamber suitable to realize a particular structure of proposed sensing configurations. Inserted fiber was exposed to HF solution with a careful protection at locations employing suitable epoxy resin. While etching, diameter of the fiber was monitored with an observed etching rate of ~1.6μm/min. Fiber etching, carried out at room temperature (20 ^{o}C), was stopped after about 45 minutes. Afterwards, fiber diameter in the etched portion was examined by a field emission scanning electron microscope (FE-SEM). A uniform fiber diameter with a reduced value of ~42 μm was observed for the etched portion of the fiber in all the three sensing configurations. That is, fiber was etched to a depth of ~83μm in the cladding region, thus making the cladding in the etched part thinner by roughly 66%. As depicted in Fig.5.1 (a), fiber was etched in such a way that a 4 mm length of the fiber in the central part of FBG remained unetched; whereas the 3 mm length of the fiber on both the ends of this 4 mm central region of FBG existed in the etched portion for the proposed sensing configuration. Bragg wavelength of this structure was observed to be 1544.09 nm. For the two other configurations structured for comparative analysis, entire grating length of 10 mm existed in the etched portion of the fiber in one configuration (Fig.5.1 (b)) with a Bragg wavelength of 1543.93 nm; whereas fiber was etched in a way that half of the grating length (5 mm) existed in

the etched portion of the fiber and the other half remained unetched in the other configuration (Fig.5.1 (c)) with a Bragg wavelength of 1544.01 nm. For each of the configurations, diameter of the fiber in unetched part was 125 µm whereas the fiber diameter in etched part was ~42 µm.

5.2.2 Sensor characterization

In order to analyze the strain response of proposed sensors (FBG carrying core with differently etched cladding structures), a strain applying setup was developed. Figure 5.2 shows the schematics of experimental set-up.

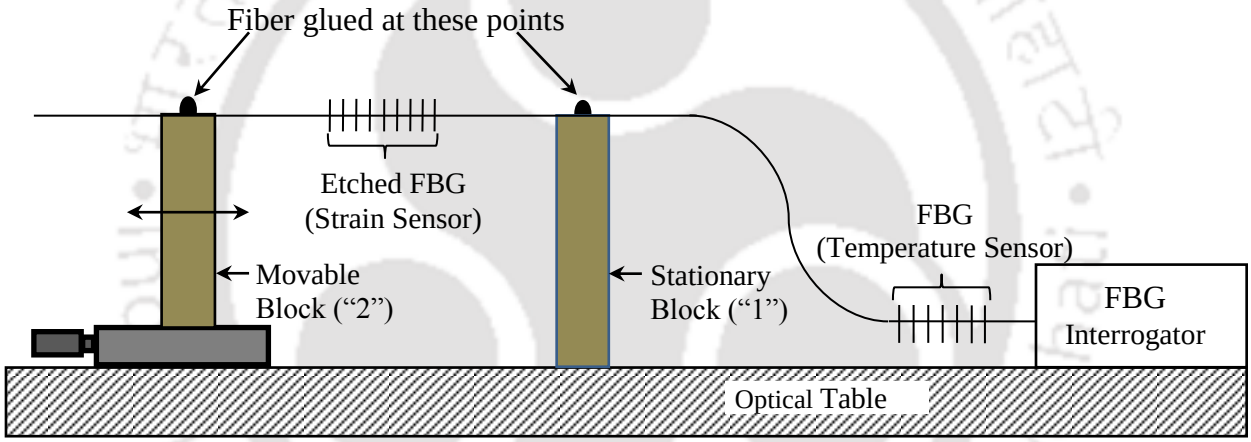

Figure 5.2: *Experimental set-up for strain sensor.*

Out of two vertical blocks used in this set-up, block '1' was rigidly fixed to an optical table, whereas block '2' was rigidly fixed over a one-dimensional translation stage. This translation stage was fixed to the optical table. Heights of the blocks were properly chosen in order to keep the top of both the blocks in the same horizontal plane. Distance between the two blocks in this arrangement was 20 cm. Translational stage was fixed in a way to have one degree of freedom - moving towards or away from the block '1'. The three differently etched FBG structures (Fig. 5.1) were separately spliced with another unetched FBG, making three sets of single fiber line

having two sensors each – etched FBG structure as sensor 1 and unetched FBG as sensor 2. The unetched FBG was identical (central wavelength 1558.62nm) in all the three sets and was used to monitor temperature variations during the experiment. In order to investigate the response characteristics of the proposed sensor, fiber carrying corrugated etched FBG structure (Fig. 5.1(a)) and unetched FBG was fixed onto the blocks in such a way that the corrugated etched FBG was exactly in the middle of blocks '1' and '2'. The part of the fiber carrying unetched FBG was in the right side of block '1'. Fiber end in this side was connected to FBG interrogator (Micron Optics, SM130-700, resolution 0.05pm). Fiber carrying corrugated etched FBG structure was replaced by the fiber carrying etched FBG structures of Fig. 1(b) and 1(c) respectively for the experiments carried out for comparative analysis. Before starting the experiment, portion of the fiber in between blocks '1' and '2' was ensured to be straight and then was suitably pre-strained in order to avoid any infinitesimal amount of slacking. At this pre-strained level, the applied strain was calibrated as zero. After words, block '2' was slowly moved towards left in order to apply forward (increasing) strain perturbations to the etched FBG structures in all the three experiments. After reaching to the maximum sustainable strain perturbation, block '2' was then slowly brought back to the calibrated zero strain position (reverse strain perturbations). Corresponding Bragg wavelength shifts of these strain sensing structures for forward as well as reverse strain perturbations along with the wavelength response of the multiplexed unetched FBG were then recorded through the interrogator. As no strain perturbation was applied to the unetched FBG, its wavelength response simply manifested the temperature variations. Wavelength response of unetched FBG was subtracted from the wavelength response of etched FBG structure in order to compensate the effect of temperature

variations during a particular experiment. It is this temperature insensitive response for the strain sensor (etched FBG structures) which was then analyzed.

5.3 RESULTS AND DISCUSSION

Before studying the response characteristics of the proposed sensor, information for response characteristics was gather for the FBG structures of Fig. 5.1(b) and Fig. 5.1(c) to facilitate a comparative analysis. To do so, FBG structure of Fig. 5.1(b) fixed between blocks "1" and "2" was suitably pre-strained in order to avoid any infinitesimal amount of fiber slacking. This strain was calibrated to zero and the Bragg wavelength ($\lambda_{B|etched}$) of this FBG structure (acting as strain sensor) at pre-strain stage was recorded as 1544.21 nm. The peak wavelength of unetched FBG (acting as temperature sensor) spliced to the same fiber was recorded as 1558.62 nm. It is the 1544.21 nm FBG (fully etched) that was exposed to increasing (forward) as well as decreasing (reverse) applied strain perturbations. Figure 5.3(a), as an example, shows the peak wavelength for two FBGs at a given applied strain during the increasing strain perturbations. Temperature compensated wavelength response of the fully etched FBG is depicted in Fig. 5.3 (b). Here, "tilted squares (triangles)" depict the wavelength response as against certain applied strain perturbations while increasing (decreasing) the strain. In order to establish the effect of reduced cladding in FBG region on the strain sensitivity, a separate experiment was carried out where an unetched (normal) FBG (peak wavelength, $\lambda_{B|unetched}$, 1543.90 nm) was used as a strain sensor. In order to monitor temperature, once again, this strain sensing unetched FBG was spliced with another unetched FBG (peak wavelength 1558.62 nm). Fiber carrying two FBGs was fixed on the two blocks as explained earlier. Strain sensing unetched (normal) FBG was again suitably pre- strained, with this applied pre-strain calibrated to zero. At this stage, Bragg wavelength for

this FBG was observed to be 1545.7 nm. Temperature compensated strain response of normal FBG is also plotted in the same graph shown in Fig 5.3(b). Here, "squares (crosses)" depict the wavelength response as against certain applied strain perturbations while

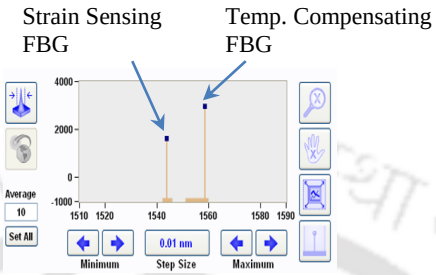

Figure 5.3 (a): *Peak wavelengths of fully etched FBG (strain sensor) and a separate normal (unetched) FBG (temperature sensor).*

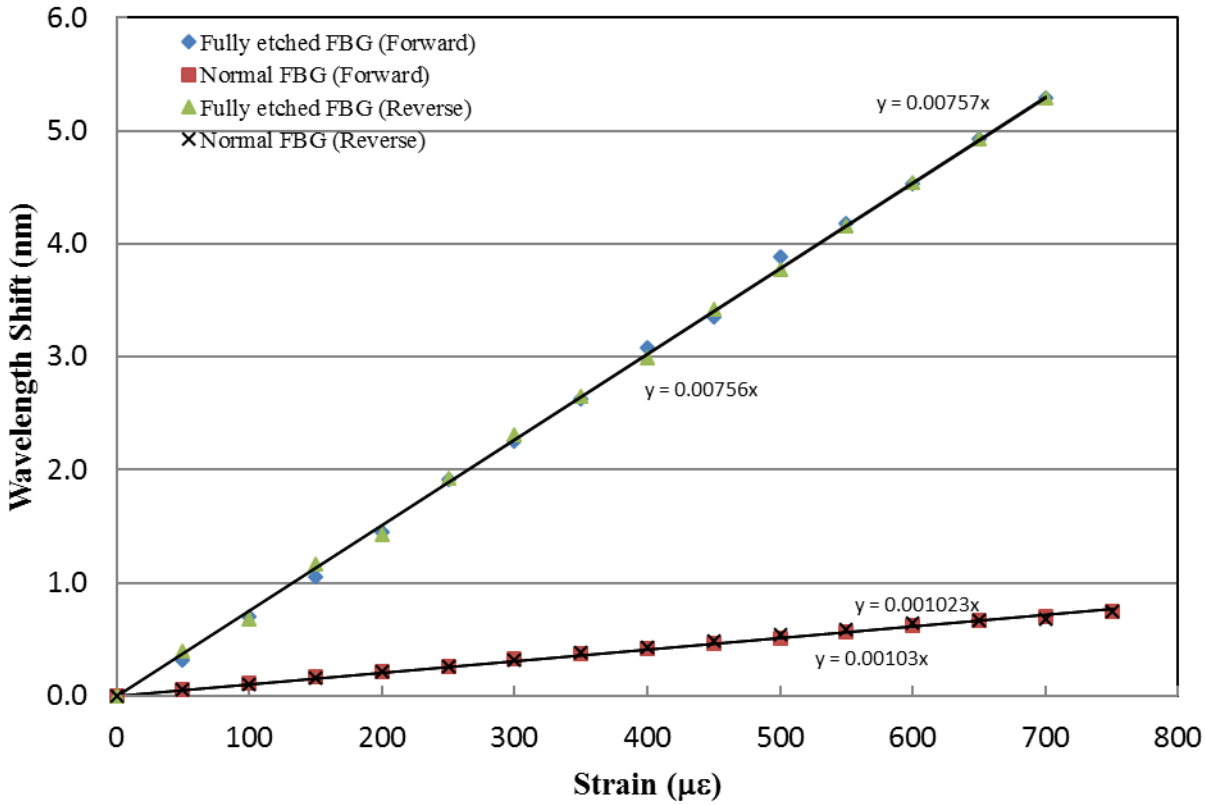

Figure 5.3 (b): *Wavelength response against applied strain for fully etched FBG (tilted squares and triangles) and normal FBG (squares and crosses).*

increasing (decreasing) the strain. Following observations can be made from this plot: (a) dynamic range of fully etched FBG and normal (unetched) FBG strain sensors is almost the same; (b) sensor response is linear for forward as well as reverse strain variations for both the sensors; (c) fully-etched FBG exhibits far better strain sensitivity as compared to the normal (unetched) FBG. The observed strain sensitivity of etched FBG was 7.57 pm/με as against the observed strain sensitivity of 1.02 pm/με for normal (unetched) FBG; (d) measured linear sensitivities for forward and reverse strain variations for both the sensing structures are found to be almost identical. This manifests a highly reversible nature of the sensor. Strain sensitivity is theoretically defined as the ratio of wavelength shift per unit applied strain:

$$\Delta\lambda_B/\Delta\varepsilon = (1 - \rho_\varepsilon)\lambda_B \tag{5.1}$$

With the fiber and FBG parameters mentioned earlier, experimentally observed strain sensitivity of normal (unetched) FBG is found to be in accordance with the theoretically predicted strain sensitivity as dictated by Eq. 5.1. This shows that reducing the cladding in the FBG region by ~66%, increases the strain sensitivity of FBG by a factor of over 7.4. In fact, when the block '2' is moved during the experiment, a tensile strain ($\Delta\varepsilon = \Delta L/L$) is induced to the fiber length (L) fixed between blocks '1' and '2'. ΔL is the total elongation over the fiber length L. Under mechanical equilibrium and certain conditions, this induced tensile strain is inversely proportional to the cross-sectional area of the fiber, which leads to:

$$\Delta\varepsilon_{etched} = \Delta\varepsilon_{unetched} \times (r_{unetched}/r_{etched})^2 \tag{5.2}$$

where $\Delta\varepsilon_{etched}$ is the strain in the etched part of the fiber carrying FBG, $\Delta\varepsilon_{unetched}$ is the strain in the normal fiber carrying FBG, r_{etched} is the radius of the fiber in the etched region and $r_{unetched}$ is the radius of the normal (unetched) fiber. Eq. (5.1) and Eq. (5.2) lead to the following relation

$$(\Delta\lambda_B|_{etched})/(\Delta\lambda_B|_{unetched}) = (\lambda_B|_{etched})/(\lambda_B|_{unetched})\times(r_{unetched}/r_{etched})^2 \quad (5.3)$$

Eq. (5.3) predicts a strain sensitivity enhancement ratio of ~8. Experimentally observed sensitivity enhancement factor is close to this value. Further, for this FBG structure (Fig. 5.1(b)), maximum discrepancy is observed to be less than ±0.092nm with corresponding strain measurement accuracy of ~±12.15με for forward as well as the reverse directions of applied strain perturbations. The resolution of the sensor completely depends on the resolution of the interrogating device. Strain resolution as small as 0.0066με is observed in this case.

Afterwards, fully-etched FBG between blocks '1' and '2' was replaced by half etched–half unetched geometry shown in Fig. 5.1(c). Fiber between the blocks was again suitably pre-strained. This pre-strain was calibrated to zero. Figure 5.4(a-i) shows the response of this structure at the beginning (pre-strain stage) of the experiment, where half etched–half unetched FBG structure is depicted by a single wavelength peak at 1544.19 nm and the unetched FBG (temperature sensor) is depicted by a peak at 1558.62 nm. Nevertheless, while carrying out the experiment by applying additional slowly varying strain perturbations, the strain response of this half etched–half unetched FBG structure is observed to be quite different as compared to the previous experiment. While applying strain, the length of FBG carrying complete cladding over it and the length of FBG carrying reduced cladding over it respond as two separate and

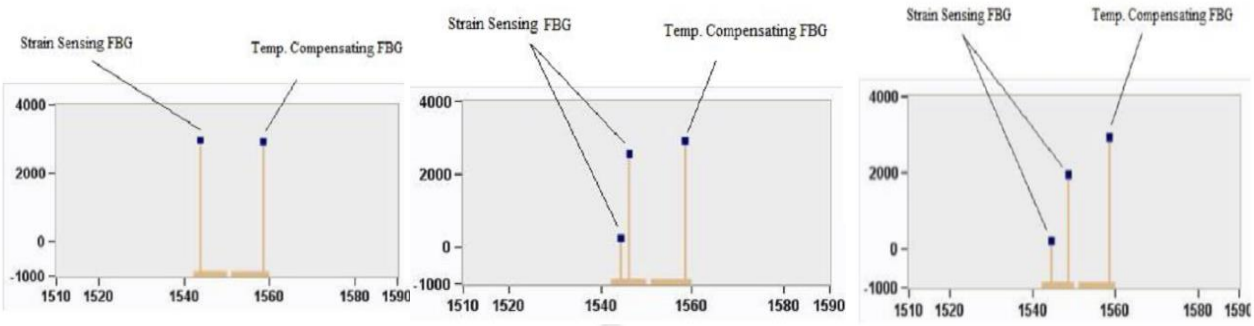

(i) (ii) (iii)

Figure 5.4 (a): *Response of etched-half and unetched-half FBG sections of FBG against applying strain at three stages, (i) at pre-strain stage with no applied strain, (ii) and (iii) at two different stages during increasing applied strain.*

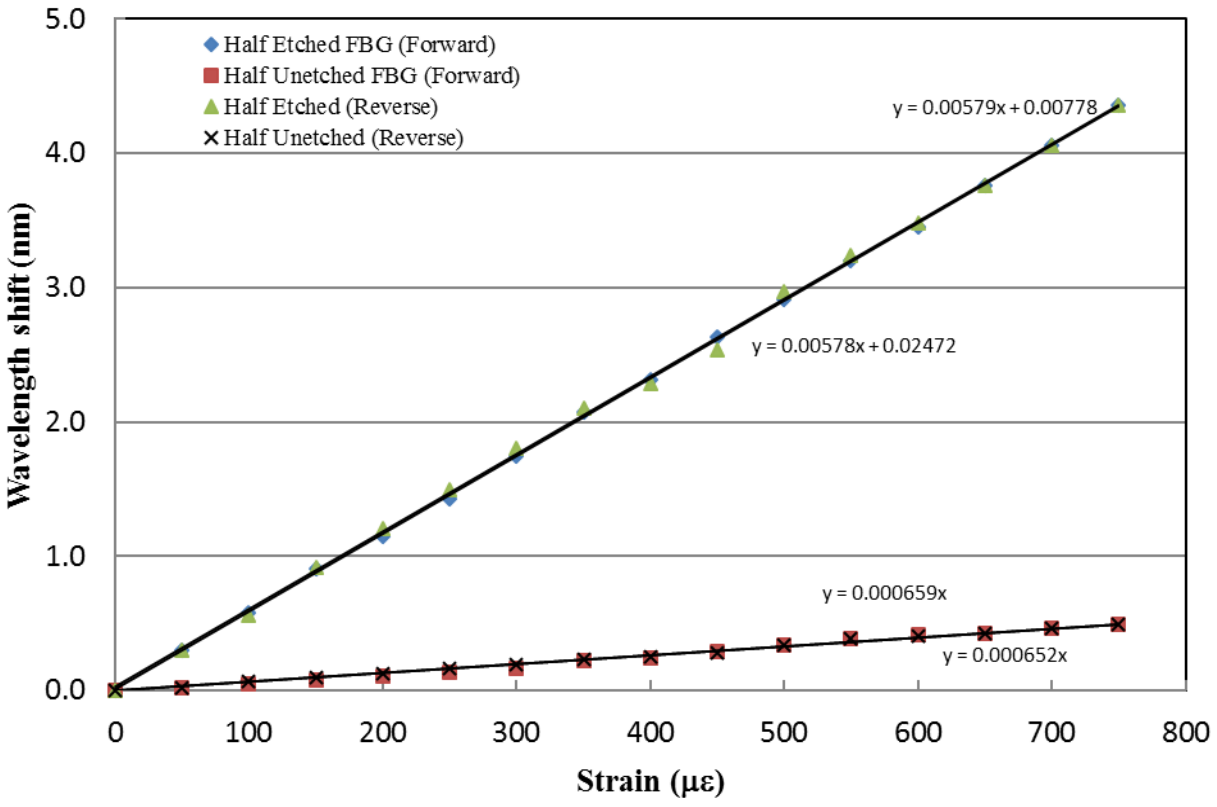

Figure 5.4 (b): *Wavelength response against applied strain for half etched – half unetched FBG.*

independent FBGs depicted by two wavelength peaks around 1544.19 nm in Fig. 5.4(a-ii). While increasing the applied strain, separation between the peak wavelengths of two structures (etched half–unetched half) of a single FBG acting as two independent FBG sensors increases as depicted in Fig. 5.4(a-iii). A complete temperature compensated wavelength response of these two parts of single FBG is plotted in Fig 5.4(b). "Tilted squares"/"triangles" depict the wavelength response of the etched part of FBG whereas "squares"/"crosses" depict the wavelength response of the unetched part of FBG as against certain applied strain perturbations while increasing/decreasing the strain. Following observations can be made from this figure: (a) a single FBG strain sensor splits into two separate and independent FBG sensors; (b) the response of both of these splitted, separate and independent sensors is linear to applied strain for forward as well as reverse strain variations; (c) the dynamic range is observed to be up to ~750 με. This is almost same as the one observed in the previous experiment for the FBG structure of Fig. 5.1(b); (d) the strain sensitivity of etched–half section of FBG is observed to be 5.79 pm/με whereas the strain sensitivity of unetched–half section of FBG is observed to be 0.66 pm/με; (e) measured linear sensitivities during forward and reverse strain variations for both the sections of the single FBG are found to be almost identical. This manifests a highly reversible nature of the sensor. These sensitivities are compiled in Table 5.1 for easy reference and comparison. The sensitivity of unetched part of FBG in this geometry (0.66 pm/με) is less than the strain sensitivity of the normal (unetched) FBG of previous experiment. The strain sensitivity of etched–half section of this FBG structure, which also acts as an independent strain sensor, is now compared with the strain sensitivities of (i) normal (unetched) FBG used in the previous experiment and (ii) the unetched–half section of the same FBG structure. As can be observed from Table 5.1, the strain sensitivity of etched–half section of FBG of this second FBG structure

(5.79 pm/με) is quite high (5.7 times) as compared to the strain sensitivity of the normal (unetched) FBG (1.02 pm/με); and very high (~8.8 times) as compared to the strain sensitivity of unetched–half section of same structure. As the two sections of present structure are derived initially from the same FBG, initial peak wavelength for both sections of FBG is identical. Further, both sections that are structured on the same fiber have identical fiber parameters except the cross sectional area. In this situation, while being in mechanical equilibrium, the tensile strain experienced by the two sections of the sensing structure would be modified from Eq. (5.3) to the following:

$$(\Delta\lambda_B|_{etched})/(\Delta\lambda_B|_{unetched}) = (r_{unetched}/r_{etched})^2 \quad (5.4)$$

Equation (5.4) predicts that the strain sensitivity of etched–half section must increase by ~8.9 times in comparison to the strain sensitivity of unetched–half section of this FBG structure. Experimentally observed sensitivity enhancement ratio of ~8.8 is very close to the theoretically predicted ratio. Further, for the etched–half section of this half etched–half unetched FBG structure, maximum discrepancy is observed to be less than ±0.035nm with corresponding strain measurement accuracy of ~±6.05με and strain resolution of ~0.0086με for forward as well as the reverse directions of applied strain perturbations. Importantly, an immediate advantage of this structure is that one can use this single FBG structure for designing a temperature independent sensor with enhanced sensitivity. The parameter to be monitored can be mapped in strain domain and be applied to the etched part of this structure.

Finally, the response characteristics of the proposed sensor corrugated FBG structure were experimentally investigated. During this, FBG configuration in Fig. 5.1(a) (etched–unetched–etched leading to corrugated structure over a single FBG) existed between blocks ‘1’ and ‘2’.

Fiber between the blocks was again suitably pre-strained. This pre-strain was calibrated to zero. Figure 5.4(a-i) shows the response of this structure at the beginning (pre-strain stage) of the experiment, where etched–unetched–etched FBG structure is depicted by a single wavelength peak at 1544.15 nm and unetched FBG (temperature sensor) is depicted by a peak at 1558.62 nm. Nevertheless, while carrying out the experiment, the strain response of this etched–unetched–etched (corrugated) FBG structure was observed to be quite different. Unetched section "CB" responds as a separate and independent FBG sensor (as observed in the previous experiment also); whereas the two etched sections of this structure ("DC" and "BA") do not respond to applied strain identically. These two sections ("DC" and "BA") act as two additional, separate and independent FBGs. Thus, while applying strain perturbations, this FBG structure acts as a total of three separate and independent FBGs depicted by three wavelength peaks around 1544.15 nm in Fig 5.5(a-ii). While increasing applied strain, separation between the peak wavelengths of the three sections (etched–unetched–etched) of a single FBG acting as three independent FBG sensors increases as depicted in Fig. 5.5(a-iii). A complete temperature compensated wavelength response of these three parts of single FBG is plotted in Fig. 5.5 (b) for increasing (forward) as well as decreasing (reverse) applied strain perturbations. "Triangles" and "crosses" depict the wavelength response of one 3mm etched FBG section as against certain applied strain perturbations during increasing and decreasing strain perturbations respectively. "Squares" and "filled circles" depict the wavelength response of other 3mm etched FBG region for increasing and decreasing strain perturbations respectively. On the other hand, "tilted squares" and "pluses" depict the wavelength response of 4mm unetched part of FBG during increasing and decreasing strain perturbations respectively. Following observations can be made from this figure: (a) a single FBG strain sensor splits into three separate and independent FBG

sensors; (b) the response of all the three splitted, separate and independent sensors is linear to the applied strain

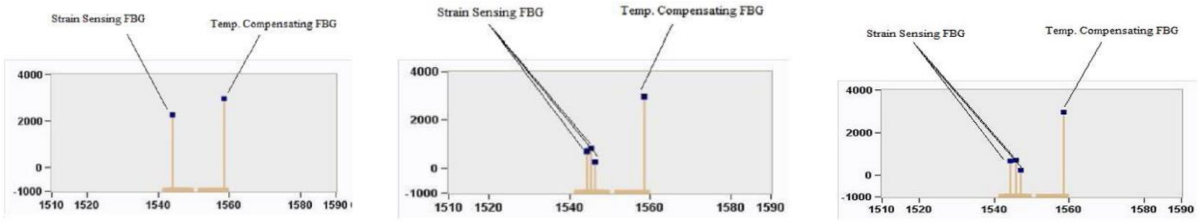

(i) (ii) (iii)

Figure 5.5 (a): *Response of etched-unetched-etched (corrugated) sections of FBG against applying strain at three stages, (i) at pre-strain stage with no applied strain, (ii) and (iii) at two different stages during increasing applied strain.*

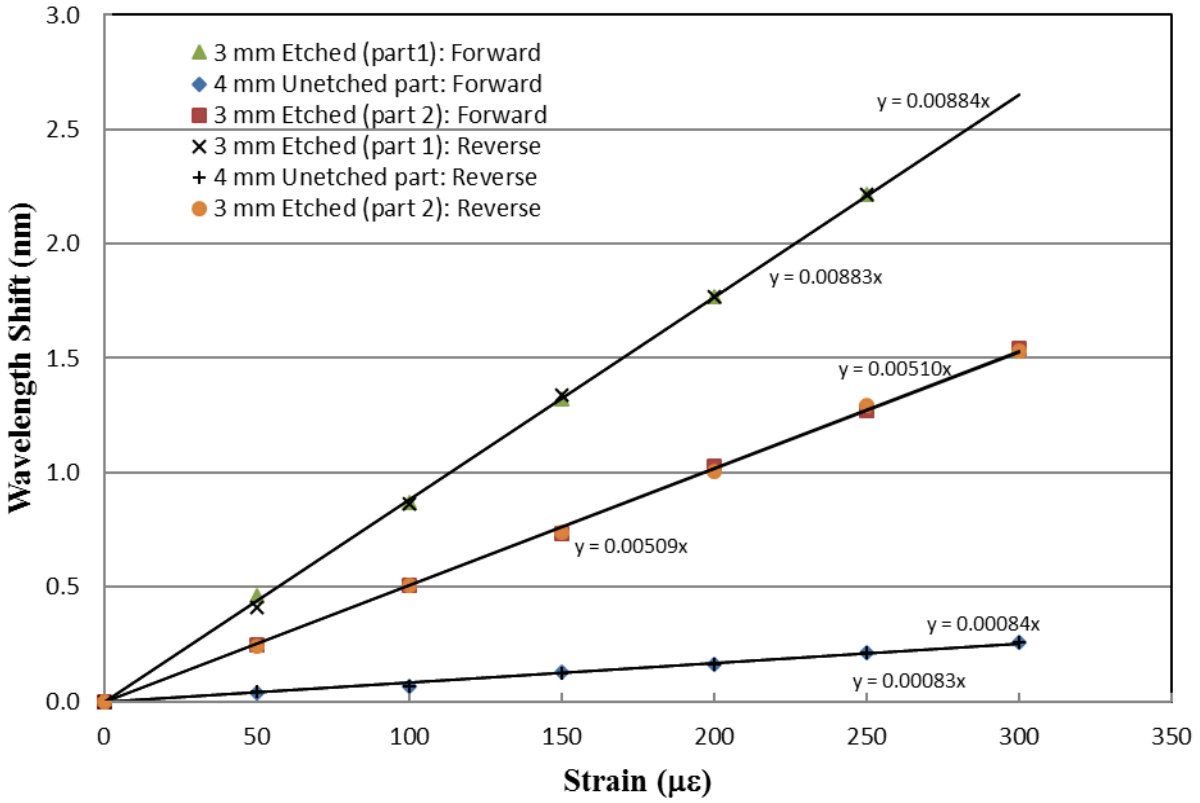

Figure 5.5 (b): *Wavelength response against applied strain for etched-unetched-etched (corrugated) FBG.*

for forward as well as reverse strain variations; (c) the dynamic range is limited in this case to ~300 με, which is quite less than the dynamic range observed for the two other FBG structures developed and experimentally investigated in the previous sections. The reason is attributed to the fragility of the etched parts of the fiber and the sustainability limit towards higher strain perturbations; (d) the strain sensitivity of the one 3mm etched FBG section is observed to be 5.10 pm/με whereas that of the other 3mm etched FBG section is observed to be 8.84 pm/με. Additionally, the strain sensitivity of unetched section of this FBG structure is observed to be 0.84 pm/με; (e) measured linear sensitivities during forward and reverse strain variations for the three sensing structures of the single FBG are found to be almost identical. This manifests a highly reversible nature of the sensor. These sensitivities are also compiled in Table 5.1. As can be observed from this Table, the sensitivity of unetched section of this FBG structure is quite close to the strain sensitivity observed for the normal (unetched) FBG in the first experiment. On the other hand, the strain sensitivity of one of the 3mm etched section of this corrugated FBG structure (5.10 pm/με) is 5 times greater than the strain sensitivity of normal (unetched) FBG (1.02 pm/με); is little less than the strain sensitivity of fully-etched FBG structure of Fig. 5.1 (b) (7.57 pm/με); is almost same as the maximum strain sensitivity observed for half etched–half unetched FBG structure of Fig. 5.1 (c) (5.79 pm/με); and is over 6 times greater than the strain sensitivity of un–etched section of the same FBG structure. Strikingly, the strain sensitivity of other 3mm etched section of corrugated FBG structure (8.84 pm/με) is quite high (~8.7 times) as compared to the strain sensitivity of 1.02 pm/με observed for the normal (unetched) FBG; is 1.2 times higher in comparison to the strain sensitivity of 7.57 pm/με observed for the fully-etched FBG structure of Fig. 5.1 (b); is 1.5 times higher in comparison to the maximum strain

sensitivity of 5.79 pm/με observed for the etched–half section of Fig. 5.1 (c); and very high (>10.5 times) as compared to the strain sensitivity of 0.84 pm/με observed for the 4mm unetched FBG section of the same geometry. Over 10.5 times strain sensitivity enhancement is a remarkable achievement, never observed so far to the best of author' knowledge. It's worth mentioning that the three sections of present structure are derived initially from the same FBG, having identical initial peak wavelengths and same fiber parameters. However, the cross sectional area varies across the structure for the three sections. Response of this corrugated FBG structure can be explained employing the dynamic analysis model. If the fiber is pulled by a force "*F*", different sections of the corrugated structures will experience different forces. Further, the force experienced by various sections will decrease while moving from section "DC" to "CB" and to "BA". This will lead to different strain distribution across different sections of this structure. Ratio of the strain in the two consecutive sections of the corrugated structure, DC to CB and CB to BA, can be given by

$$\frac{\Delta\varepsilon|_{\text{etched,DC}}}{\Delta\varepsilon|_{\text{unetched,CB}}} = \frac{F|_{\text{etched,DC}}}{F|_{\text{unetched,CB}}} \times \left(\frac{r|_{\text{unetched,CB}}}{r|_{\text{etched,DC}}}\right)^2 \tag{5.5}$$

and

$$\frac{\Delta\varepsilon|_{\text{unetched,CB}}}{\Delta\varepsilon|_{\text{etched,BA}}} = \frac{F|_{\text{unetched,CB}}}{F|_{\text{etched,BA}}} \times \left(\frac{r|_{\text{etched,BA}}}{r|_{\text{unetched,CB}}}\right)^2 \tag{5.6}$$

Above analysis depicts that $\Delta\varepsilon|_{\text{etched,DC}}$ is greater than $\Delta\varepsilon|_{\text{etched,BA}}$, leading to a higher Bragg wavelength shift ($\Delta\lambda_B \propto \Delta\varepsilon$) for the section "DC"; and that ways, a higher strain sensitivity for one of the etched section in comparison to the other etched section of this corrugated structure as observed experimentally. Further, for the etched section of this FBG structure that gives maximum strain sensitivity enhancement, maximum discrepancy is observed to be less than ±0.019nm with corresponding strain measurement accuracy of ±2.15με and strain resolution of

~0.0057με for forward as well as the reverse directions of applied strain perturbations. Comparing the response characteristics of all the three sensor configurations, it's the sensing configuration derived from a single FBG for the proposed sensor that is characterized with highest stain measurement sensitivity, lowest maximum discrepancy and best accuracy with a capability to resolve minimum strain in nano-scale strain (nε) range.

TABLE 5.1: Summary of performance characteristics of various FBG structures.

FBG Structure	Description of FBG Structure	Section of FBG	Observed Sensitivity (pm/με)	Strain Resolution	Maximum discrepancy	Accuracy (με)
1	Corrugated FBG	Etched part-1	8.84	0.0098 με		
		Etched part-2	5.10	0.0057 με	±0.019 nm	±2.15
		Unetched part	0.84	0.0595 με		
2	Normal FBG		1.02	0.0490 με		
3	Fully Etched FBG		7.57	0.0066 με	±0.092 nm	±12.15
4	Half Etched-Half Unetched FBG	Etched Half	5.79	0.0086 με	±0.035 nm	±6.05
		Un-Etched Half	0.66	0.0806 με		

In the next step, repeatability and reliability tests are carried out to rigorously analyze the sensor performance. For this, experiments with the proposed corrugated FBG structures were repeated on 3 different days with an interval of a week. As an example, response of the three sections of etched–unetched–etched (corrugated) FBG structure corresponding to an applied strain perturbation of 250 με is depicted in Fig. 5.6. As can be observed, sensor output is almost constant over a span of 2 weeks. Compared to day 1, a maximum variation in the response of the

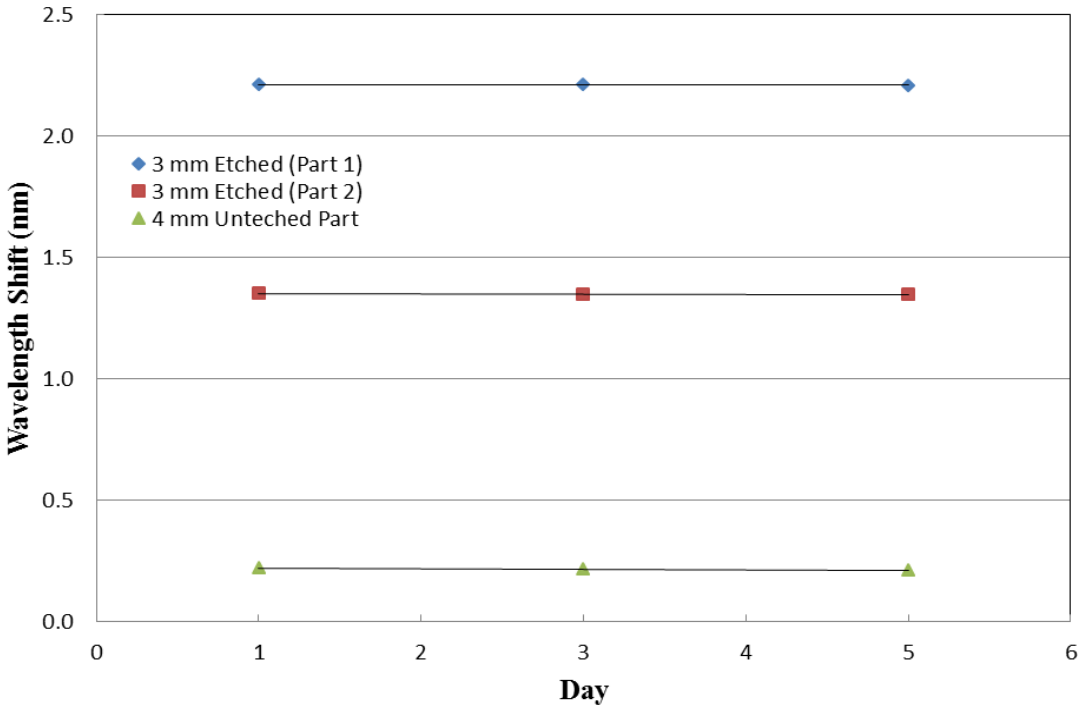

Figure 5.6: *Repeatability and reliability test: Response of different sections of etched-unetched-etched FBG structure on the three different days for an applied strain of 250 με.*

three sections, acting as three independent sensors, is observed to be of the order of $\pm 10^{-3}$ nm. Similar responses are observed at other strain perturbations. This shows a good reliability and repeatability of the proposed sensor configurations, qualifying them suitably for real-field applications. Thus, the proposed etched–unetched–etched (corrugated) structure derived from a

single FBG is of extreme practical importance not only for an effective and stable sensing capabilities reflected by facilitating remarkably high strain sensitivity, completely reversible and very reliable response characteristics, good accuracy, low maximum discrepancy and nano-scale strain (nε) resolution, but also for a possibility of designing/devising multi-parameter sensing employing the three sections that act as three separate and independent sensors. If the parameter of interest is mapped suitably over one of the two etched sections, the resulting sensor is bound to have high sensitivity as compared to a separate sensor that employs a normal FBG.

5.4. CONCLUSION

A novel design strategy in terms of corrugated cladding structure over a FBG carrying core is proposed and experimentally investigated, predominantly to achieve strain sensitivity enhancement and a possibility of deriving multiple independent sensors from a single FBG. Two more cladding structures are carved out from a single FBG for exhaustive and comparative analysis. Proposed sensor splits into multiple and independent FBG sensors according to the employed cladding structure. Strikingly, a remarkably high strain sensitivity enhancement is observed with the sensing configuration that employed a corrugated cladding structure. Strain sensitivity of one of the etched section is observed to be over 10.5 times in comparison to the strain sensitivity of unetched section of this structure. It's impossible to realize such a high sensitivity employing normal FBG. Further, this sensing structure is characterized with a good strain measurement accuracy (±2.15με), low maximum discrepancy (±0.019nm), nano-scale strain resolution (~5.7nε), completely reversible and reliable linear response characteristics. All these features, in particular, a remarkably high strain measurement sensitivity enhancement,

nano-scale strain resolution and single FBG structure acting as three separate and independent sensors, make the proposed sensor of extreme practical importance.

Chapter 6

Fiber Bragg Grating Based Humidity Sensor Employing Effective Refractive Index Modulation Technique

6.1 Introduction

Precise monitoring of relative humidity (RH) is of extreme importance in number of applications such as semiconductor manufacturing processes, structural-health-monitoring, chemical/biochemical/food processing industries and air-conditioning to name a few [104]. There exist a number of conventional RH sensors with a characteristically good sensitivity. However, such sensors find limited place in real-field applications because of their critical and inherent limitations [105]. Owing to numerous but distinct inherent advantages over the conventional/optical sensors and related technological advancements, optical fiber based sensors have convincingly established themselves as an alternate to the traditional sensing schemes. Numerous attempts have been made to realize optical fiber RH sensors [131,106-110]. Predominantly, these sensors exploit evanescent wave absorption model employing straight and uniform/U-bent/tapered/side-polished fiber structure. Some of such attempts also employed an interferometric model. Irrespective of the employed methodologies, nonlinearity in the response characteristics, limited dynamic range and piece-wise sensitivity variation remain the matter of great concern for almost all these reported optical fiber based humidity sensors barring a few. On the other hand, since its invention and successive advancements, in-fiber Bragg gratings (FBGs) have become synonym to the optical sensing technology as for as real-field applications are concerned. The class of optical fiber sensors, which are based on wavelength modulation scheme, dominantly uses in-fiber gratings (FBG/long period gratings (LPG)) as the constituting sensing element. RH sensors are no exception; various

attempts have also been made to realize in-fiber grating based RH sensors. In order to develop FBG based RH sensor, RH is preferably and strategically mapped in strain domain. This strain mapping is achieved as following: a suitable thermoplastic/polyimide material that is coated on the FBG swells in accordance when exposed to the humid vapours. This leads to a strain variation across FBG, which ultimately results in a wavelength modulation, exactly a signature of RH variations, in the response characteristics of FBG. As an example, Kronenberg et al. in [111], Yeo et al. in [112] and Huang et al. in [113] employed polyimide coated FBG structure for humidity detection. A linear response over a limited dynamic range with a sensitivity of ~3.4 pm/%RH is observed in [111]. Comparatively, researcher in [112] succeeded in improving the sensitivity to a maximum value of 5.6 pm/%RH for the observed dynamic range of 23-97%RH; whereas in [113], succeeded in extending the linear dynamic range to 11-98%RH at the expense of sensitivity. In contrast, water affinity of certain polymer facilitates swelling as well as an increase of the refractive-index (RI) of the material. Owing to these two effects, FBGs written in such polymer optical fibers (POF) are observed to be appreciably more sensitive to RH exposure. Exploiting these effects, Zhang et al. [114] have reported POFBG based RH sensor. In another attempt, Rajan et al. have reported etched POFBG based RH sensor [115]. Sensitivity improved as expected. However, response characteristic is observed to be nonlinear with dynamic range limited and sensitivity varying piece-wise across. On the other hand, being inherently sensitive to the ambient RI, structures such as long-period-gratings (LPGs) [116-119] and tilted FBGs [120] in conjugation with a suitable polymer (gelatin/hygrogel/SiO_2/TiO_2/PVA) sensing film are also exploited to realize RH sensor. For LPG based RH sensors, highest dynamic range of 33–97%RH is observed in [116], but the sensor response was nonlinear throughout. For tilted FBG based RH sensor, a piecewise linear response in the RH range of 20-74% and 74-98% is observed. Recently, an RH sensor based on a polymer-infiltrated photonic crystal fiber interferometer has also been

reported in [121]. A nonlinear response across the reported dynamic range is observed. Further, realization of a reversible and repeatable response with this scheme remains a challenge.

Bragg wavelength of an in-fiber grating depends on the effective-refractive-index (n_{eff}) and the grating-pitch (Λ). For a standard optical fiber, effective-refractive-index can only be modulated by applying strain/temperature perturbations through strain-optic/thermo-optics effects; and remains independent to the ambient RI variations. This results in FBGs being inherently sensitive to strain/temperature variations through the modulations of effective-refractive-index as well as the grating-pitch; and insensitive to ambient refractive-indices. However, if the cladding diameter in the FBG region is reduced, effective-refractive-index of the fiber gets significantly affected by the ambient refractive-indices, whereas pitch of the grating remains unaffected. Importantly, the reduction of the cladding diameter in the grating region results in a stronger interaction of the evanescent tail of the fundamental guided mode of the fiber with the surrounding medium. These effects lead to the modulation of Bragg wavelength and the amplitude of the reflected wavelength due to the ambient RI variations. Thus, a FBG with thinned cladding in its region becomes an inherent sensor for not only strain and temperature but also to the ambient refractive-indices. A few RI sensors exploiting this technique are reported in [132-134]. Recently, this technique is extended to realize CO_2 and bio sensors where etched cladding in FBG region was coated with carbon nanotube and Graphene [135, 136]. However, to the best of the author's knowledge, this technique is not extended to realize a relative humidity (RH) sensor.

The main objective of the research reported in this chapter is to develop a temperature independent FBG based RH sensor employing effective-index modulation induced Bragg

wavelength shift scheme for the first time to the best of author's knowledge, rather than the traditional strain induced Bragg wavelength shift scheme reported in the literature. Sensor development is focused to achieve a throughout linear response over a wide dynamic RH range and an optimum sensitivity. To design the sensor, FBG structure is suitably modified by reducing fiber diameter in the grating region to a lowest possible working limit (~ a few microns). Response characteristic of the sensor against ambient environmental parameter, resulting from RH variations, is theoretically investigated. Afterwards, sensor is experimentally investigated by exposing it to the repeat cycles of increasing and decreasing RH variations over a sufficiently long time period. A linear response over a dynamic range as wide as ~3 – 94% RH with a good sensitivity of ~ 0.08 pm/%RH during increasing as well as decreasing humidity is observed. Proposed sensor is more than ten times faster than the commercial sensor. Maximum fiber output variation is observed to be of the order of only 10^{-4} during the repeatability and reversibility tests. Importantly, experimental response characteristic of the sensor is observed to be in accordance to the theoretical analysis. In addition, a relatively better resolution (~ 0.6%RH), accuracy (~ ±2.5%RH), average discrepancy (~ ±0.2 pm) and response time (~ 0.2s) is observed during humidification and dessication cycles.

6.2 Theoretical Analysis

Bragg condition manifests the condition for strong coupling between identical or nearly identical forward- and counter-propagating modes in a fiber grating inscribed in a single-mode-fiber (SMF). The wavelength that satisfies this condition (termed as Bragg wavelength, λ_B) in a uniform fiber grating depends on the effective-refractive-index (n_{eff}) of the mode and the grating-pitch (Λ) through $\lambda_B = 2\Lambda n_{eff}$. Grating-pitch is dictated by the phase-mask used for inscribing the FBG and has nothing to do with the RI of the surrounding medium (n_{out}).

Effective-refractive-index of the fundamental mode in a standard uniform SMF is also independent of the RI of the medium surrounding the fiber cladding. However, if the refractive-index is varied in the medium surrounding the fiber cladding at a constant temperature and without straining the fiber, as is the case of varying RH from lowest to the highest possible values in the present case, and if the fiber diameter in the cladding region is sufficiently reduced, n_{eff}, and hence, λ_B will get modulated accordingly. In this way, the resulting Bragg wavelength modulation would be a direct consequence of effective-index-variation as dictated by the RH variation. This is the principle exploited for developing RH sensor in the present work. In order to theoretically study the response characteristics of FBG that exits in a fiber of reduced cladding diameter and is exposed to the refractive-index variations corresponding to 0% RH (dry air with refractive index 1) to an RH value close to 99%, doubly-clad fiber model reported in [137] is employed. This model is best suited for the present case to find a distinct relationship between the modal propagation constant β and n_{out}. Once β is known for a given n_{out}, λ_B can be easily calculated through $\lambda_B = 2\Lambda n_{eff} = 2\Lambda(\beta/k_0)$, where k_0 is free space wave number. Simulated fiber structure under doubly-clad fiber model for thinned FBG is depicted in the inset of Fig. 6.1. Here a and b are the core and inner-cladding radii respectively, whereas n_{co}, n_{cl}, and n_{out} are the refractive indices of core, inner-cladding and the surrounding medium (outer cladding) respectively. For the azimuthal order m, the radial dependence $\psi(r)$ of the axial field components are expressed as [137]

$$\psi = A'_0 J_m(u\frac{r}{a}) \quad \text{For} \quad r \le a \tag{6.1}$$

$$\psi = A'_1 I_m\left(v'\frac{r}{b}\right) + A'_2 K_m\left(v'\frac{r}{b}\right) \quad \text{For } a \le r \le b \text{ if } \beta > k_0 n_2 \tag{6.2}$$

$$\psi = A'_3 K_m(v\frac{r}{b}) \quad \text{For} \quad r \ge b \tag{6.3}$$

where J_m are ordinary Bessel functions, K_m and I_m are modified Bessel functions; β is the propagation constant, which is greater than $k_0 n_{cl}$ for guided modes; $u = a(k_0^2 n_{co}^2 - \beta^2)^{1/2}$, v =

$b(\beta^2 - k_0^2 n_{out}^2)^{1/2}$, and $v' = b(\beta^2 - k_0^2 n_{cl}^2)^{1/2}$. A'_0 is a normalization coefficient which is determined by applying the boundary conditions. Under the weekly-guiding approximation, continuity of the transverse field components across the two interfaces (between core and inner cladding, and between inner and outer cladding) leads to a set of four equations:

$$A'_0 J_m(u) - A'_1 I_m(v'c) - A'_2 K_m(v'c) = 0 \tag{6.4}$$

$$uA'_0 J'_m(u) - v'cA'_1 I'_m(v'c) - v'cA'_2 K'_m(v'c) = 0 \tag{6.5}$$

$$A'_1 I_m(v') + A'_2 K_m(v') - A'_3 K_m(v) = 0 \tag{6.6}$$

$$v'A'_1 I'_m(v') + v'A'_2 K'_m(v') - vA'_3 K'_m(v) = 0 \tag{6.7}$$

where $Z' = dZ/dr$ (Z is Bessel function: J_m, I_m or K_m) and $c = a/b$. Equating the determinant of 4×4 coefficient matrix of these equations to zero (to ensure a nontrivial solution) leads to the dispersion equation for the guided mode ($\beta > k_0 n_{cl}$) of the doubly-clad fiber as following

$$\frac{[\hat{J}_m(u) - \hat{K}_m(v'c)][\hat{K}_m(v) + \hat{I}_m(v')]}{[\hat{J}_m(u) + \hat{I}_m(v'c)][\hat{K}_m(v) - \hat{K}_m(v')]} = \frac{[\hat{I}_{m+1}(v'c)\hat{K}_{m+1}(v')]}{[\hat{I}_{m+1}(v')\hat{K}_{m+1}(v'c)]} \tag{6.8}$$

where $\hat{Z}_m(x) = \frac{Z_m(x)}{xZ_{m+1}(x)}$ and x is $u/v'c/v'$. Replacing the value of $\hat{Z}_m(x)$ and substituting $m = 0$ for the fundamental mode (LP_{01}) in equation (6.8), dispersion equation simplifies to

$$\frac{[v'cK_1(v'c)J_0(u) - uJ_1(u)K_0(v'c)]}{[v'cI_1(v'c)J_0(u) + uJ_1(u)I_0(v'c)]} = \frac{[v'K_1(v')K_0(v) - vK_1(v)K_0(v')]}{[v'I_1(v')K_0(v) + vK_1(v)I_0(v')]} \tag{6.9}$$

This transcendental (dispersion) equation ((Eq. (6.9)) is solved numerically in MATLAB software where the fiber parameters of SMF-28 (a = 4.15μm, n_{co} = 1.460, n_{clad} = 1.4564) are used owing to fact that the FBG used in the experiment is written in this standard fiber. While solving Eq. (6.9), n_{out} is varied from 1 (corresponding to 0%RH) to 1.456 (clad refractive-index) at a fixed cladding diameter. Solutions obtained from the above analysis are used to simulate the response of FBG towards the surrounding RI variations. Figure 6.1 shows the simulated response of FBG (λ_B vs n_{out}) for the optical fiber having cladding radii (b) equal to 62.5 (corresponding to the unetched fiber), 12, 10, 8, 6.75 and 6μm in the FBG region.

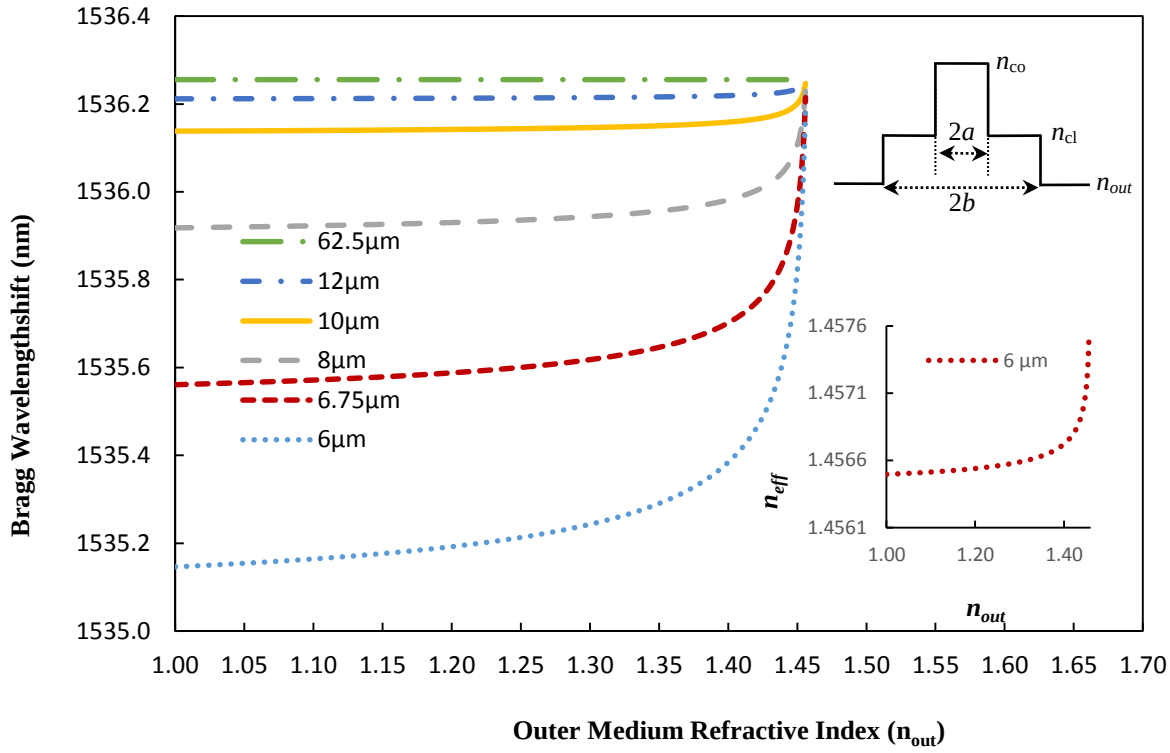

Figure 6.1: *Bragg wavelength of a FBG existing in a reduced cladding diameter fiber versus outer medium refractive-index for different cladding radii. Upper inset shows the refractive index variation along a cross section of a double cladding and weekly guiding fiber. Lower inset shows effective-refractive-index of the thinned FBG versus outer medium refractive-index for cladding radius of 6µm.*

As can be observed from Fig. 6.1, FBG in a normal (unetched) fiber is insensitive to the variations in the surrounding RI (and hence to the surrounding RH). Decreasing the cladding diameter in the FBG region increases its sensitivity towards the surrounding refractive-indices. In the present calculation, highest overall sensitivity towards the surrounding RI is witnessed for the fiber having a cladding radius of 6µm in the FBG region. Further, this sensitivity is observed to be very low for the surrounding RI variations in between 1 to 1.07. Sensitivity increases very slowly and linearly afterwards till surrounding RI approaches to 1.4; and afterwards, sharply and very significantly as surrounding RI approaches to n_{clad}. Basically, the sensor response is dictated by n_{eff} seen by the fundamental mode against the

surrounding RI variations. Hence, n_{eff} versus n_{out} is also plotted, as an example, for b = 6μm in the inset of Fig. 6.1. If the fundamental mode is confined within the fiber with its evanescent tail dying-off sufficiently well below the clad-outer medium interface, the effective-index (n_{eff}) seen by the mode will have no influence of the surrounding medium refractive-indices. This is exactly the case of unetched fiber in weekly-guiding approximation. However, when the fiber is sufficiently etched in its cladding region down towards the core, average RI in the cladding region gets significantly affected. Lower the average RI in the cladding region (as is the case with the lowest value of n_{out} = 1), the tighter is the confinement of the fundamental mode to the fiber core; which in turn, leads to a week influence of the surrounding RI on the effective-index (n_{eff}) seen by the mode. As n_{out} increases, average RI also increases. This leads to a lesser confinement of the fundamental mode to the fiber core and a greater interaction with the outer medium in the thinned cladding region, and that way, a greater influence of n_{out} on n_{eff} seen by the mode. Any influence of n_{out} on n_{eff} gets accordingly imprinted on the reflected Bragg wavelength, λ_B. The observed theoretical response of the FBG that exists in an etched fiber region is used to analyze the experimental findings in the subsequent section.

6.3 Experimental

6.3.1 Sensor Design and Construction

Two FBGs spliced together, each 8 mm long and written onto a germanium doped silica single-mode-fiber (SMF-28, 125μm diameter), were used in this study. Bragg wavelength of one of the FBG (λ_1) was 1545.0 nm whereas that of the other FBG (λ_2) was 1536.195 nm. In order to realize FBG based RH sensor, cladding of the fiber in the FBG region for the first FBG (λ_1) was etched to a few micron levels. This cladding reduction was achieved using

standard, but appropriately controlled, chemical etching procedure that employed HF (Hydrofluoric) acid solution. To do this, an etching chamber was designed with an inner dimension of 8 mm. This chamber was initially filled with HF solution at 40%wt. concentration. Fiber was fixed inside the etching chamber in such a way that only the length of the fiber that carries first FBG could get exposed to the HF solution. Effective etching of the fiber requires a suitable control over the etching time, especially when one desires to reduce the total fiber diameter to a few microns only. Hence, fiber in the FBG region was first exposed to this 40% HF for 48 minutes. Etching was stopped by removing the fiber from the etching chamber. Etched region of the fiber was then cleaned with NaOH solution. Afterwards, fiber diameter in the etched portion was examined by a field-emission scanning-electron-microscope (FE-SEM) (Sigma FE-SEM, Carl Zeiss NTS, USA, resolution 2.5 nm). A uniform fiber diameter with a reduced value of ~18µm was observed for the etched portion of the fiber. To develop the proposed FBG based RH sensor with fiber diameter in the FBG

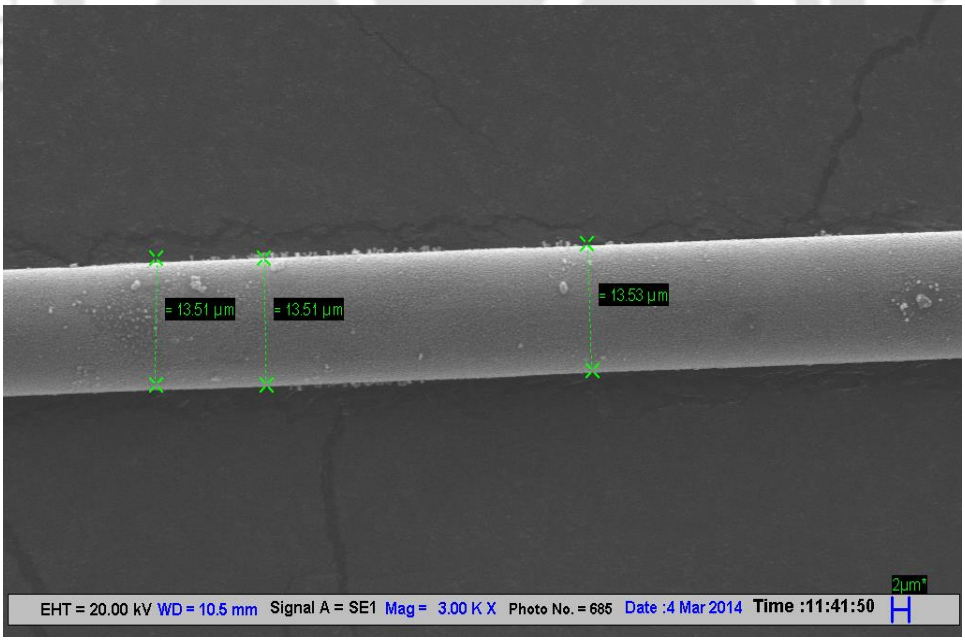

Figure 6.2: *Scanning electron microscopic image of the etched FBG region of the optical fiber.*

region reduced to the lowest possible working limit, this etched region of ~18μm fiber diameter was again fixed in the etching chamber to further expose it to the HF solution. For this second phase of final etching, the concentration of HF solution was suitably diluted to 15% wt. in order to slow down and to have a fine control on the etching processes. Exposure of the etched fiber to this 15% wt. HF solution was suitably controlled in order to estimate the critical exposure time required for the fiber to get completely etched out. This critical exposure time was observed to be 34.5 minutes. Etching of the FBG in this phase was stopped a few seconds before the observed critical exposure time by draining the HF solution out of the etching chamber and cleaning the etched fiber with NaOH solution. Entire etching process was carried out at room temperature (19.8^{o}C). Fiber diameter in the etched region at the end of this final etching process was again analyzed with FE-SEM. Figure 6.2 shows the FE-SEM image of the fiber in the finally etched FBG region. A uniform fiber diameter with a reduced value of ~13.5μm is observed for the etched portion of the fiber. Fiber with a further lower cladding diameter could not be achieved. It's worth mentioning that etching is a nonlinear process where etching rate increases extremely sharply within a few seconds just before the critical exposure time. One requires an automated system to stop etching process a few microseconds before the critical exposure time to achieve lowest possible fiber diameter within the working limit. Stopping the etching process a few seconds before the critical exposure time, as was the case in the present work, will result in a little higher cladding diameter. Finally, the Bragg wavelength of the FBG that exists in this finally etched fiber, λ_1^E, is observed to be 1541.311nm.

6.3.2 Sensor characterization

To investigate sensor characteristics against the applied RH perturbations, a humidity chamber of dimension 11cm × 9cm × 7cm was designed using Perspex sheet. Humidity

inside the chamber was varied by appropriately mixing the humid and dry airs. Two sophisticated flow meters were used to suitably control the flow rate as well as the mixing of dry and humid airs. A commercially available RH sensor (capacitive type), interfaced to a computer via DAQ card and LABview programming, was fixed to this humidity chamber. This commercial RH sensor monitored instantaneous humidity as well as temperature inside the chamber. Fiber carrying etched FBG at λ_1^E (RH sensor) and unetched FBG at λ_2 (temperature sensor) was carefully fixed inside this in-house developed humidity chamber.

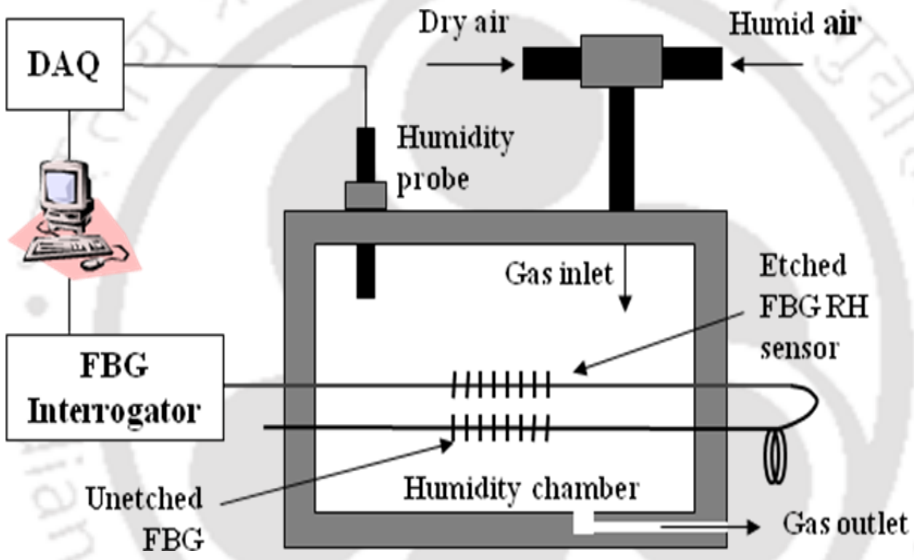

Figure 6.3: *Schematic diagram of experimental setup for sensor characterization.*

Fiber was fixed in such a way that both the gratings remained parallel to each other in the same horizontal plane and at the center of the chamber, as depicted in the schematics of the experimental setup (Fig. 6.3). While fixing the fiber, special attention was paid in order to keep Bragg wavelengths for both the FBGs to their natural values (λ_1^E & λ_2). This ensured that the gratings were not strained and preserved their normal length. In this configuration, unetched FBG can only respond to the temperature variations, if any, inside the humidity chamber. Thus, it acted as the temperature sensor. One end of this fiber was connected to a FBG interrogator (Micron Optics, SM130-700, resolution 0.05pm), which was configured

with a computer. To carry out the experiment, humidity level was first increased to the maximum possible value by injecting humid air into the chamber. Subsequently, RH was slowly decreased in suitable steps to the minimum possible value. RH changes in steps were imposed only after a proper stabilization of humidity inside the chamber at a particular value, that is, after a sufficiently large time gap. Entire experiment was carried out at a fixed room temperature of 19.8^{o}C. During the experiment, commercial sensor's output was monitored as a function of time with a resolution of 1s. Simultaneously, responses of both the FBG sensors were also monitored through the FBG interrogator in real-time basis. Wavelength response of the unetched FBG (acting as temperature sensor) was subtracted from the wavelength response of the etched FBG (acting as RH sensor) in order to compensate the effect of temperature variations during a particular experiment. It is this temperature insensitive response for the etched FBG based RH sensor which was subsequently analyzed.

6.4 Results and Discussion

Research in the present study is focussed on to capture RH variations in terms of an effective-index-modulation, rather than the traditional strain modulation, to realize an FBG based RH sensor. To achieve this, length of the fiber in the grating region was etched to the lowest possible practical limit under the laboratory constraints. A normal FBG (with full clad-diameter) was spliced to this fiber. For proper characterization of the developed sensor, fiber carrying both the FBGs was carefully fixed inside a humidity chamber. As mentioned earlier, both the FBGs, maintained in the same horizontal plane parallel to each other and at the center of the chamber, were exposed to different humid environments by suitably controlling the flow rates and properly mixing dry/humid airs. Experiments were carefully

and repeatedly carried out for decreasing as well as increasing humidity cycles. Only after the stabilization of humidity in the test-chamber, Bragg wavelengths as well as commercial

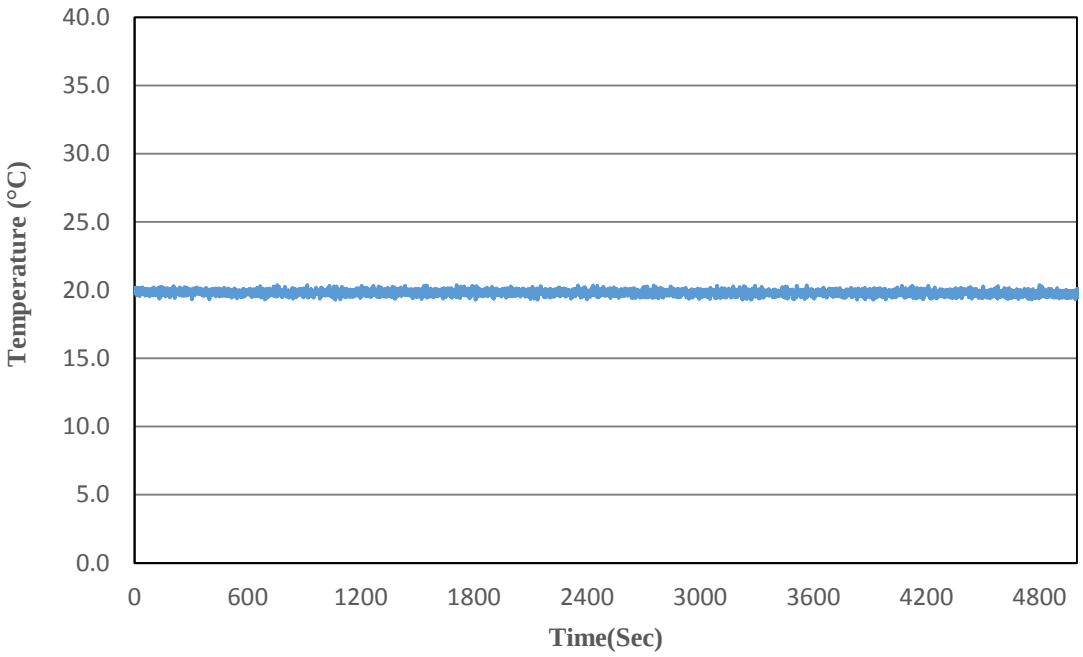

Figure 6.4: *Temperature variation inside the humidity chamber*.

sensor's output were recorded in the time domain. A constant temperature of 19.8 ºC was maintained throughout the experimental investigations. This is depicted in Fig. 6.4, which shows real-time temperature output from the commercial sensor, as an example, while decreasing the humidity. As can be observed from the figure, temperature remained almost constant at ~19.8 °C during entire experiment. A similar temperature variation was observed while increasing the humidity. Response characteristics of the normal (unetched) FBG was analyzed first. A typical response for this FBG is depicted in Fig. 6.5 while decreasing the humidity. As can be observed from the figure, FBG existing in a normal fiber (having full clad-diameter) does not respond to the applied RH perturbations. This is in accordance to the theoretical observation that for the fiber, which carries full diameter of 125µm in the grating region, varying RI in the surrounding medium will not affect n_{eff} and hence, λ_B. This establishes the fact that, for the present case, normal FBG will act only as a temperature

sensor. A maximum peak-to-peak wavelength variation for this FBG is observed to be less than 0.8pm. After establishing these facts for normal FBG sensor, response characteristics of

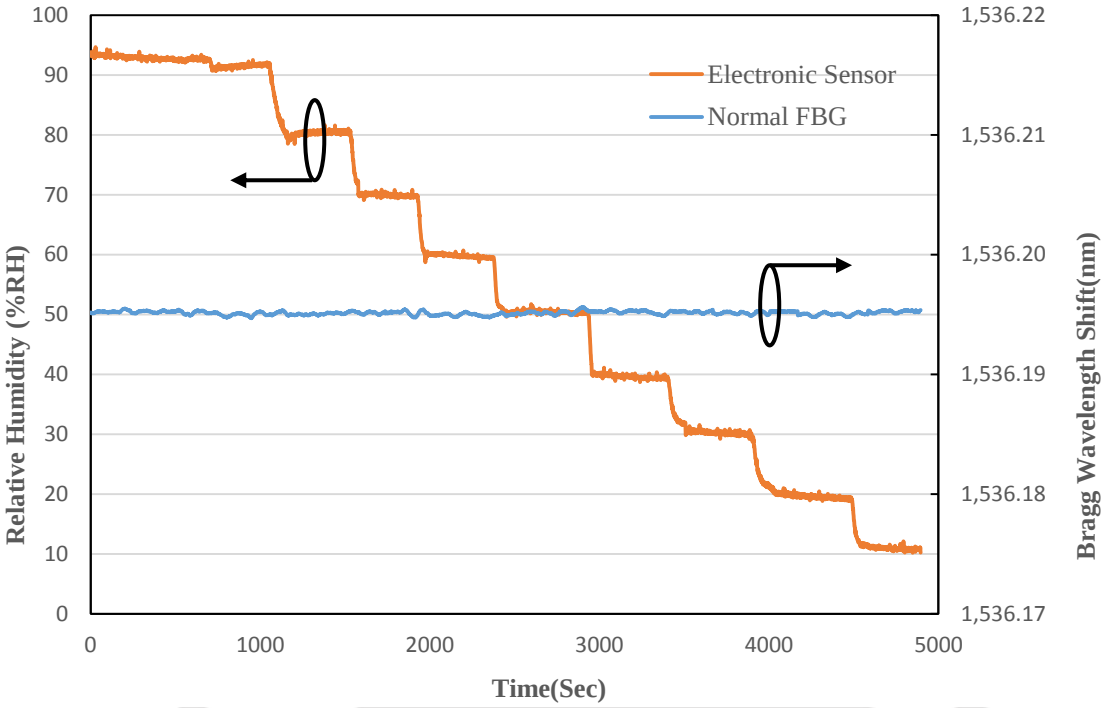

Figure 6.5: *Time variation of a commercial humidity sensor and normal (unetched) FBG sensor.*

etched FBG against applied RH perturbations were analyzed. In order to negate any effect of temperature variations in the humidity chamber, unetched FBG's (temperature sensor) response was subtracted from the etched FBG's (RH sensor) response. This enabled to realize a temperature independent all-optical fiber RH sensor. A typical temperature compensated response ($\lambda_1^E \sim \lambda_2$) of the developed humidity sensor while decreasing the humidity is shown in Fig. 6.6. As can be observed from the figure, the developed etched FBG based RH sensor follows the humidity changes very appreciably. Further, wavelength response, $\lambda_1^E \sim \lambda_2$, of the developed sensor decreases as humidity decreases inside the chamber. This can be physically understood as following: as the RH inside the chamber decreases, water content in the environment (surrounding to the fiber) decreses; and that ways, ambient refractive-index across the etched optical fiber decreases. This results in a reduced effective-refractive-index

and hence, smaller Bragg wavelength. To have a proper idea about the etched FBG based RH sensor's response, $\lambda_1^E \sim \lambda_2$ is plotted against %RH for decreasing humidity cycle in Fig. 6.7.

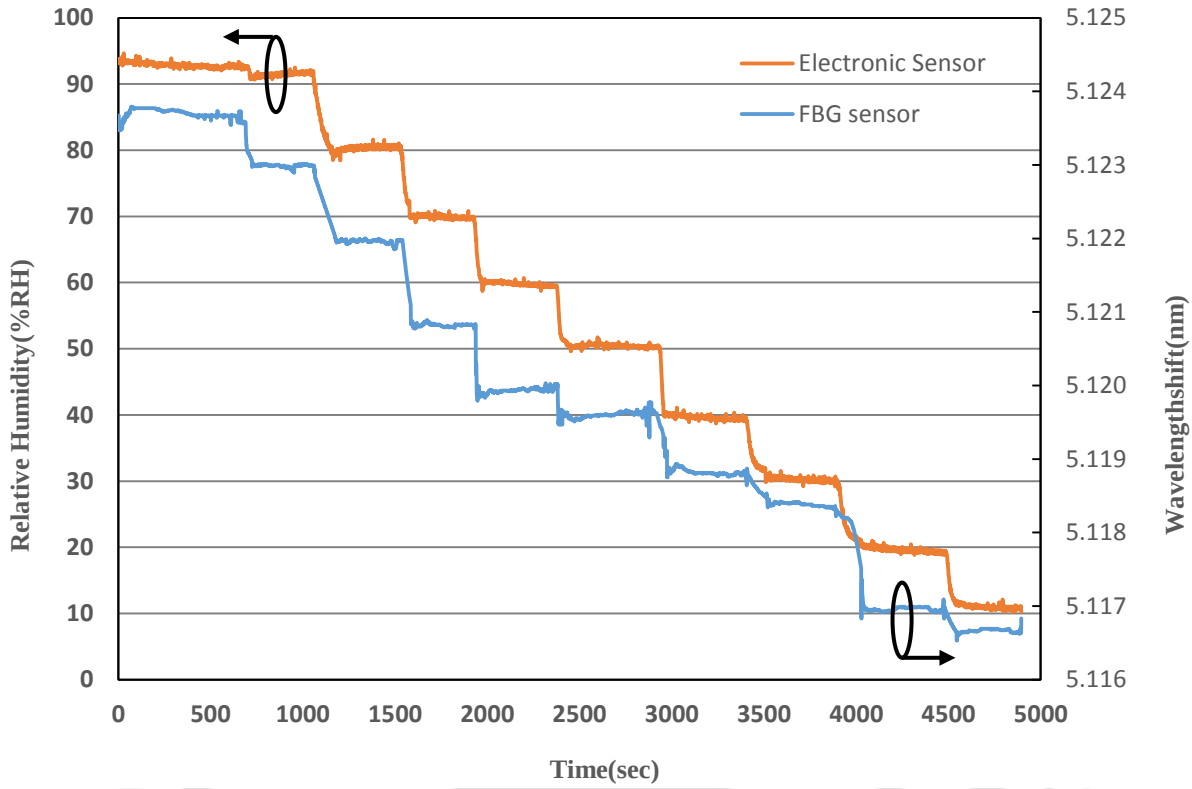

Figure 6.6: *Time variation of a commercial humidity sensor and etched FBG (RH) sensor.*

Bragg wavelength shifts and %RH values both were extracted from the stabilized portion of their time response characteristics depicted in Fig. 6.6. Theoretical response of the sensor against applied RH variations, calculated through Eq. (6.9), is also represented by the continuous line in the same figure. In order to obtain the theoretical response of the sensor, surrounding refractive-indices for different RH values are required. Its almost impossible to obtain these values of surrounding refractive-indices from the literature. Its worth mentioning that at room temperature, 100%RH corresponds to 3% water volume in the surrounding air, whereas 3%RH corresponds to a water content of 900 ppm. Without any loss of generality, one can assign the surrounding RI as 1 for 3%RH. A crude way to obtain the surrounding refractive-indices for the other RH values is by using the experimentally observed sensitivity. Utilizing the experimental data, the values of the surrounding refractive-indices (calculated

for different RH values) are found to range from 1 (assigned to 3%RH) to 1.072 (corresponding to 94%RH). Thus a total RI variation while varying RH from 3%RH to 94%RH

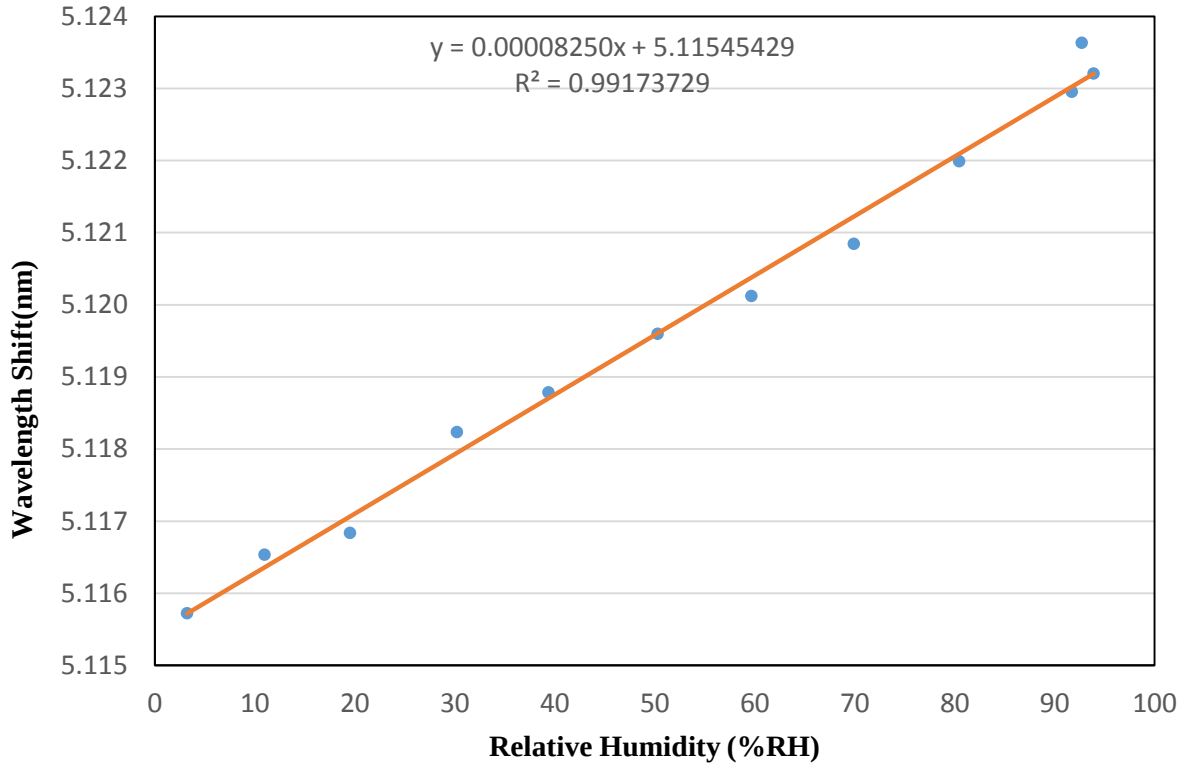

Figure 6.7: *Experimentally observed sensor response (λ_1^E ~ λ_2) while decreasing the humidity inside the chamber. Theoretical response is depicted by continuous line.*

is established to be only 0.072. These values of surrounding RI corresponding to different RH values were used to calculate the theoretical response of the sensor. As can be observed from the figure, etched FBG based RH sensor responds to an applied humidity perturbation as low as 3%RH to as high as 94%RH, thus spanning a dynamic range of 3%RH–94%RH. Importantly, the sensor characteristics is observed to be throughout linear over this dynamic range. A linear sensitivity of 0.082 pm/%RH is observed during this desiccation part of the experiment. Further, the average discrepancy is observed to be less than ±0.20pm with corresponding RH measurement accuracy of ±2.51%RH. The resolution of the sensor

completely depends on the resolution of the interrogating device. The wavelength resolution of 0.05 pm of the interrogator results in the RH resolution of 0.61%RH for the sensor. Importantly, the experimentally observed response of the proposed sensor is observed to be in accordance to the theoretically predicted one. Afterwords, humidity inside the chamber is increased in steps similar to the ones used for the desiccation part of the experiment. This time, water content in the environment, and that ways, ambient refractive-index across the etched optical fiber increases with an increase of RH inside the chamber. This results in an increased effective-refractive-index and hence, higher Bragg wavelength. Once again, wavelength response, $\lambda_1^E \sim \lambda_2$, of etched FBG based RH sensor followed step-wise increasing humidity changes very appreciably. Extracted Bragg wavelength shifts, $\lambda_1^E \sim \lambda_2$, (from the

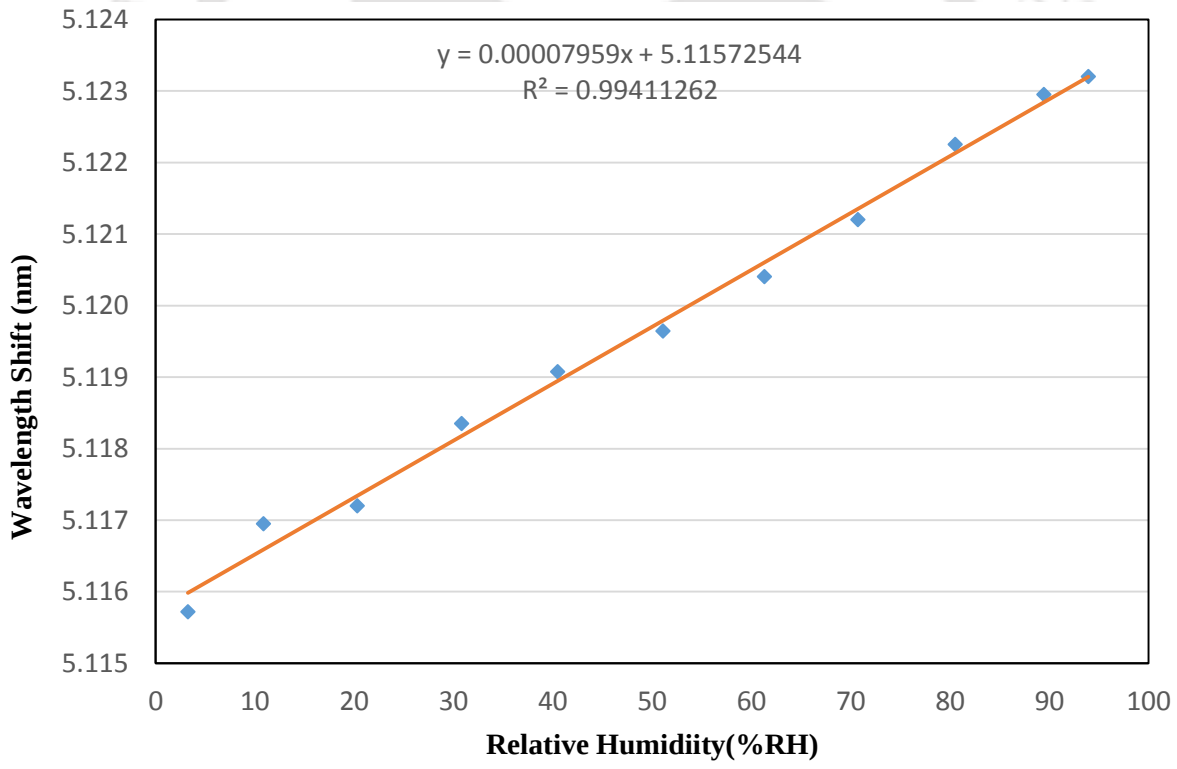

Figure 6.8: *Experimentally observed sensor response ($\lambda_1^E \sim \lambda_2$) while increasing the humidity inside the chamber. Theoretical response is depicted by continuous line.*

stabilized portion of the corresponding time response characteristics) are depicted against %RH values in Fig. 6.8 for this humidification part of the experiment. Once again, the theoretical response of the sensor against applied RH variations is also ploted (continuous line) in the same figure. As can be observed, sensor response is again linear throughout over an identical dynamic range of 3%RH–94%RH. The observed linear sensitivity for this reverse cycle of the experiment (humidification) is found to be 0.080 pm/%RH, which is almost the same as observed for the desiccation. It's important to mention that the sensitivity should ideally not depend whether the humidity is decreased or increased. Further, average discrepancy, corresponding RH measurement accuracy and the RH resolution are observed to be less than ±0.21pm, ±2.69%RH and 0.63%RH respectively, which are also closely identical to the ones observed during the desiccation. Importantly, the experimentally observed response of the proposed sensor during this humidification cycle is also observed to

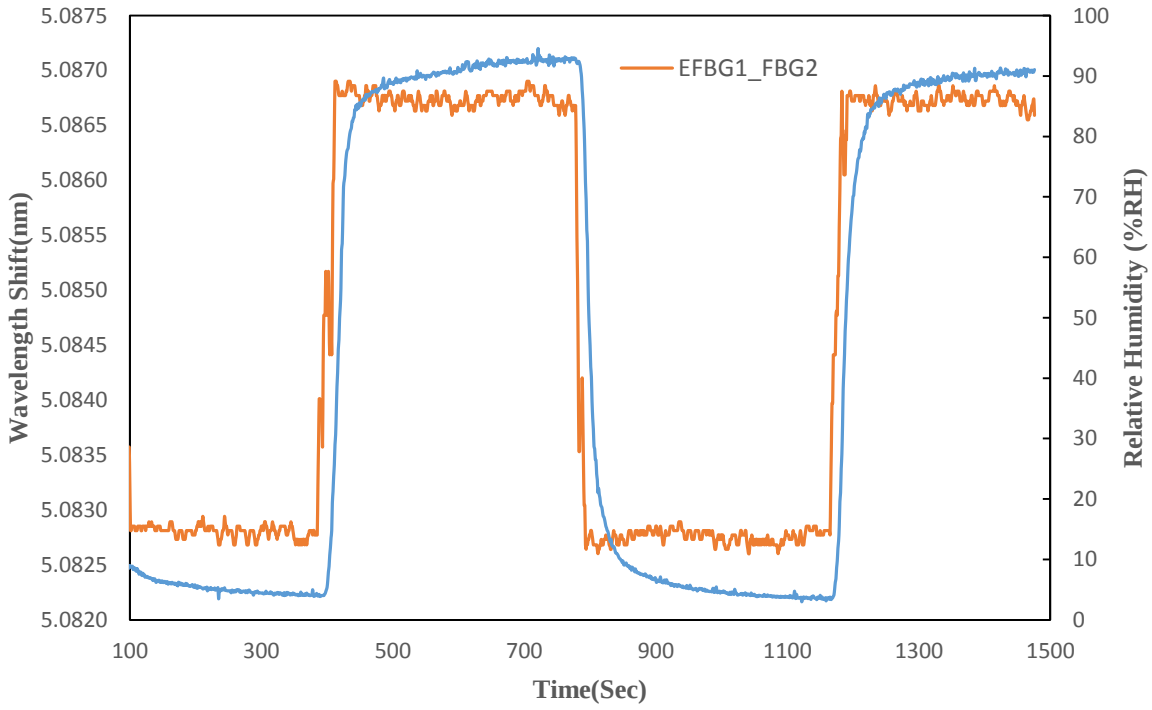

Figure 6.9: *Observed time response behavior for the etched FBG based sensor against cyclic humidity perturbations*.

be in accordance to the theoretically predicted one. In the next step, dynamic performance of the fiber sensor was investigated by exposing the fiber sensor to a repeat and quick RH step change between 5%RH to 90%RH. The humidity chamber was first desiccated to 5%RH and then quickly humidified to 90%RH by a sudden release of the humid air through a quick control of the flow meter. Observed time response for the FBG sensor during quick humidification and desiccation cycles is shown in Fig. 6.9. A markedly high signal-to-noise ratio is observed with the Bragg wavelength closely identical to the extreme RH values during the humidification and desiccation cycles. This establishes a remarkable reversibility and reproducability with no hysteresis effects for the sensor. Further, the Bragg wavelength almost instantly and smoothly responds to step-wise humidity changes. An average response time for humidification as well as for desiccation is observed to be less than 0.2 second. Upon

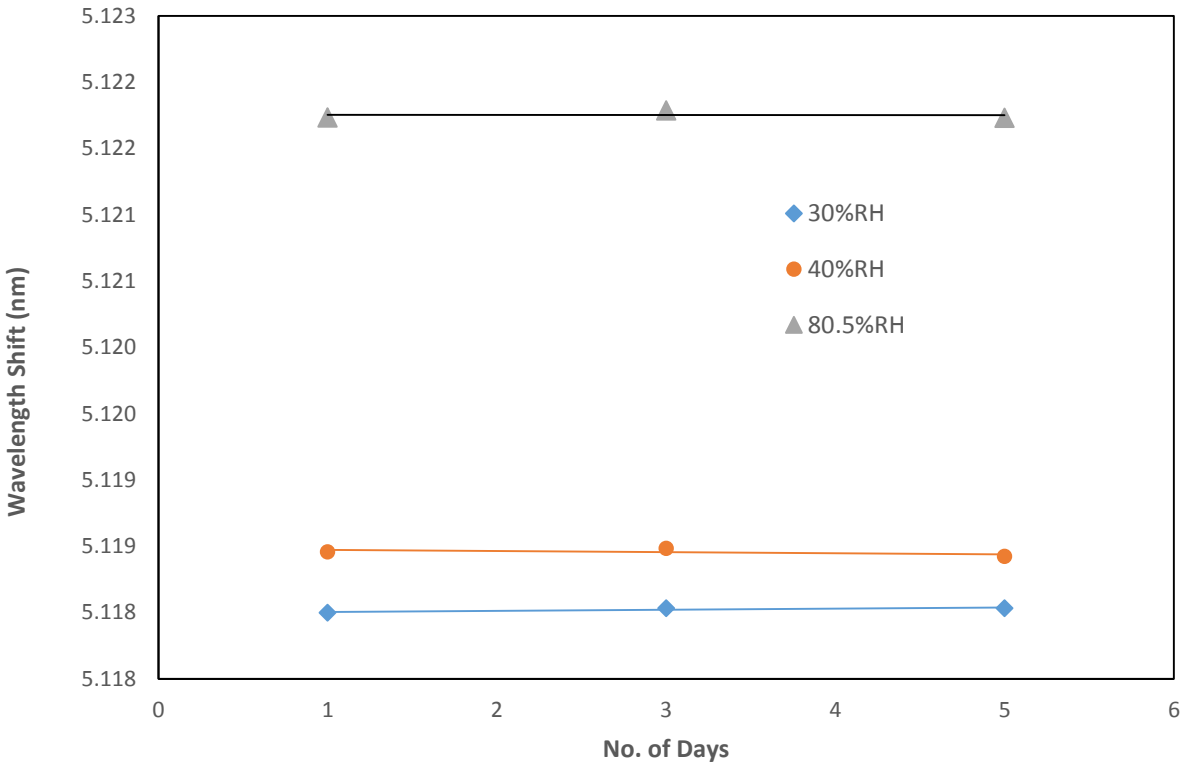

Figure 6.10: *Repeatability and reliability test: FBG sensor output on the three different days, each at an interval of 7 days for 30%, 40%, and 80.5% RH.*

comparision, this reveals that the etched FBG based RH sensor is more than ten times faster than the commercial sensor. Another equally important and desirable feature of a sensing system is its repeatability, which makes the sensor more reliable. To assess the long-term repeatability of the sensor, repeatability and reliability tests were performed. For this, experiment with the same etched and unetched. FBGs was repeated on 3 different days with an interval of one week. Sensor outputs corresponding to the three different humidity values (30%, 40%, and 80.5%RH) as an example are shown in Fig. 6.10. As can be observed from the figure, sensor output is almost constant over a span of 3 weeks. Compared to day 1, a maximum variation in the sensor output at the three different humidity values of 30%, 40%, and 80.5%RH is observed to be of the order of 10^{-4} nm. This depicts a good reliability and repeatability of the proposed sensor. Finally, the performance characteristics of the proposed FBG based RH sensor is compared with the other FBG based RH sensors reported in the literature that are characterized with linear response across the observed dynamic range. Table 1 lists, for comparison, some of the most important performance parameters that menifest an effective sensing capability of a

Table 6.1: Comparison of the performance characteristics of the developed sensor.

Author	Sensing element	Linear dynamic range (%RH)	Sensitivity	Response time	Resolution (%RH)	Accuracy (%RH)	Ave. discrepancy
Kronenberg et al. [111]	Polyimide coated FBG	10-90	~3.4pm/%RH	-	-	-	-
Yeo et al. [104]	Polyimide coated FBG	22-97	4.5pm/%RH	↓ 60 s ↑ 39 s	2	±4	±0.02 nm
Yeo et al. [112]	Polyimide coated FBG	23-97	5.6pm/%RH	↓ 21 s ↑ 34 s	-	-	-
Huang et al. [113]	Polymer coated FBG	11-98	0.000266 V/%RH	↓ 5 s ↑ 5 s	-	-	-
Reported Sensor	Etched FBG (etched core dia 13.5μm)	3-94	↓0.082pm/%RH	↓ 0.2 s	↓ 0.61	↓±2.51	↓ ±0.20 pm
			↑0.080pm/%RH	↑ 0.2 s	↑ 0.63	↑±2.69	↑ ±0.21 pm

given sensor, e.g., linear dynamic range, sensitivity, response time, resolution, accuracy and the maximum discrepancy. In this table "↓" represents dessication and "↑" represents

humidification. As can be observed from the table, among all the reported data for other FBG based RH sensors, widest linear dynamic range, fastest response time for humidification/dessication, best RH measurement accuracy and resolution are achieved in the present work. On the other hand, sensitivity of the proposed sensor appeared to be the lowest among the other sensors tabulated here. This is because of the fact that the RH variations in the present work corresponds to the surrounding RI variations that are confined at around 1. As already mentioned in the theoretical analysis, sensitivity would be very low if the RH variation would lead the surrounding RI variations confined in the range of 1 to 1.07. However, if the RH variations are mapped at around the surrounding RI of ~1.4 while keeping the fiber diameter in the etched region same (~13.5 μm), theoretically predicted sensitivity comes out to be 16pm/%RH, which is much higher than the highest sensitivity reported in [112]. Theoretically predicted sensitivity will further increase to 24pm/%RH if the fiber diameter is etched down to 12 μm and if the RH variations are mapped once again at around the surrounding RI of ~1.4. It is worth mentioning that the RH variations can be easily mapped at around the surrounding RI of ~1.4 by coating the etched cladding in the FBG region with a thin film of suitable chemical composition, which we are presently working on.

5.5 Conclusion

An all-optical temperature compensated humidity sensor is developed employing etched and unetched FBG. The main objective of the sensor development in the present study is to exploit an effective-index modulation induced Bragg wavelength shift to capture RH variations for the first time to the best of author's knowledge rather than the traditional strain induced Bragg wavelength shift scheme reported in the literature. To design the sensor, FBG structure is suitably modified by reducing fiber diameter in the grating region to a lowest possible working limit (~13.5μm). Employing three-layer fiber model, response characteristic

of the sensor against ambient environmental parameter that results from RH variations is theoretically investigated. Afterwards, sensor is experimentally investigated by exposing it to the repeat cycles of increasing and decreasing RH variations over a sufficiently long time period. Obtained results are observed to be in agreement with the theoretical analysis. Obtained results are observed to be in agreement with the theoretical analysis carried out employing three-layer fiber model. Sensor response is observed to be linear over a dynamic range as wide as ~3 – 94% RH with a sensitivity of ~ 0.082 pm/%RH. Developed sensor's response is also compared with the reported sensors in the literature. It is observed that a far better sensitivity, in comparison to the highest sensitivity reported in the literature, can be achieved by suitably mapping the RH induced surrounding RI variations at around ~1.4. A relatively better resolution (~ 0.6%RH), accuracy (~ ±2.5%RH) and average discrepancy (~ ±0.2 pm) is observed during humidification and dessication cycles. Proposed sensor is more than ten times faster than the commercial sensor. In addition, sensor response is characterized with a very high degree of reversibility and repeatability.

Chapter 7

Conclusion of Thesis

A comprehensive experimental study is carried out to develop FBG based all-optical sensors to monitor tilt, vibration, strain and relative humidity (RH), which are some of the most important parameters in SHM and other engineering/industrial applications. It's important to mention that not only a reasonably good sensitivity is required in such applications; sensor is simultaneously desired to have an ability to capture the applied perturbations strategically very effectively and without any inherent instability. The objective of the research carried out in the present thesis is to develop these sensors with manifold enhanced sensitivity, tunable response characteristics and without inherent measurement instabilities. A novel, temperature insensitive, pendulum based sensor design strategy employing four FBGs with a feature of inherent tuning capability for its sensitivity is characterized. Sensor exhibits a completely reversible linear response over a dynamic range of $\pm 10^{o}$. An excellent sensitivity (~0.0626 nm/^{o}) that can further be nonlinearly tuned with a much improved resolution (0.008^{o}), accuracy ($\pm 0.36^{o}$), maximum discrepancy (less than ±0.0231nm) and maximum angular uncertainty ($\sim \pm 0.34^{o}$) are established for this sensor. In order to capture the applied tilt perturbations strategically more effectively with enhanced stability, another novel FBG based tilt sensor, employing a non-pendulum type design strategy is realized. Being non-pendulum type, there is no possibility of any inherent friction and the limiting effects at mechanical joints. This sensor exhibits a better resolution (better than 0.004°), a better accuracy (~±0.05°) and a lesser maximum discrepancy (~±0.001nm) during the forward as well as the reverse tilts. Sensor response is characterized by a very high degree of reversibility

and repeatability over the observed dynamic range. In the next step, a simple design strategy of FBG based two axial all-optical vibration sensor, employing a methodology to ensure chirp-free mechanism is proposed and experimentally demonstrated. In this design, vibration of sensor displaces the seismic mass fixed between two flexural beams, thus inducing a variable strain in the two beams. This strain variation results in a Bragg wavelength shift for corresponding FBGs attached to the beams. An excellent capability of resolving externally applied signals having frequency in 10Hz to 350Hz and the acceleration in 0.65 to 70m/sec^2 range is observed. Further, if the inherent strain sensitivity of FBG can be enhanced to a very large value, it will improve the response of all the FBG based sensors. In order to achieve this, a single FBG sensor with corrugated cladding structure over the FBG carrying core is designed and experimentally investigated for strain sensitivity enhancement. The corrugated structure across the FBG section of the fiber splits a single FBG into multiple & independent FBGs, each suitable for independently sensing an applied perturbation. Further, a manifold enhancement of the strain sensitivity (over ten times relative enhancement of strain sensitivity) is observed, which is impossible to realize with a normal FBG. Finally, in the last part of research, FBG based humidity sensor is developed employing a novel mechanism of effective-index modulation with an ambition to achieve widest possible dynamic range and optimum sensitivity. To achieve these objectives, fiber diameter in the grating region is reduced to a lowest possible working limit (~ a few microns) using appropriately controlled chemical etching. A wide linear dynamic range ~3–94 %RH with good sensitivity of ~0.082 pm/%RH is realized. The response of the developed sensor is observed to be completely reversible with an appreciably stable characteristic during repeatability tests.

Thesis work leads to the possibility of wide range of potential research work to be carried out in the future. For example, all the sensors reported here in the thesis are characterized in the laboratory environment; however, these sensors are aimed for real-field applications such as in SHM. While deploying the sensor in monitoring locations/over the monitored infrastructures, fiber sensor should not only be protected from a possible source that may damage it but also, all the characteristic features and merits of the sensor should be preserved in such real-field monitoring applications. As an example, the reported FBG based RH sensor in the present form cannot be used to detect moisture content in concrete structures. This emphasises the need of an intelligent packaging of the sensor and then re-characterizing the sensor response in real-filed locations. Further, as mentioned for the corrugated FBG based sensor developed in the thesis work, a single FBG sensor splits into three independent FBG sensors with enhanced strain sensitivity. As a future work, one needs to employ the three sections of this sensor to design a sensor that can monitor three different parameters independently without any cross-talk. Similarly, in the case of FBG based humidity sensor, owing to the laboratory constraints, we could not etch the diameter of the fiber over FBG region below 13.5μm, though, we observed that the sensitivity will increase if the diameter is lowered further. In addition, we also observed that if the RH variations are mapped around the surrounding RI of ~1.4, sensitivity will increase manifold. RH variations can be easily mapped at around this surrounding RI by coating the etched fiber in the FBG region with a thin film of suitable chemical composition. This leads to the possibility of designing a FBG based RH sensor employing effective-index modulation technique with a far better response characteristics.

References

1. B. P. Pal, "Fundamentals of fiber optics in telecommunication and sensor systems," (*New Age Inc.*, 2003).
2. P. J. Schubert, and J. H. Nevin, "A Polyimide-based capacitive humidity sensor" *Tran. Electr. Devi.*, **32**, pp.1220 (1985).
3. M. Suster, J. Guo, N. Chaimanonart, W. H. Ko, and D. J. Young, "A high-performance MEMS capacitive strain sensor," *J. Micro Electromechan. Syst.*, **15**, pp.1069 (2006).
4. H. Seidel, H. Riedel, R. Kolbeck, G. Muck, W. Kupke, and M. Koniger, "Capacitive silicon accelerometer with highly symmetrical design" *Sens. Actuators A*, **21**, pp.312 (1990).
5. D. Benz, T. Botzelmann, H. Kuck, and D. Warkentin, "On low cost inclination sensor made from selectively metallized polymer," *Sens. Actuators A*, **123**, pp.80 (2005).
6. H. Kautsky, and A. Hirsch, "Optical sensor for low level oxygen detection", *Chem. Ber.*, **64**, pp2677, 1931
7. X. Y. Fang, and M. S. Cao, "Theoretical analysis of 2D laser angle sensor and several design parameters," *Opt. Laser Tech.*, **34**, pp.225 (2002).
8. X. Ge, Y. Kostov, and G. Rao, "High-stability non-invasive auto cleavable naked optical CO_2 sensor," *Biosens. Bioelectron.*, **18**, pp.857 (2003).
9. S. K. Lee, and I. Okura, "Porphyrin-doped sol-gel glass as a probe for oxygen," *Anal. Chim. Acta.*, **342**, pp.181 (1997).

10. H. J. Nam, T. Sasaki, and N. Koshizaki, "Optical CO gas sensor using a cobalt oxide thin film prepared by pulsed laser deposition under various argon pressures," *J. Phys. Chem. B,* **110**, pp.23081 (2006).
11. J. W. Aylott, D. J. Richardson, and D. A. Russell, "Optical biosensing of gaseous nitric oxide using spin-coated sol-gel thin films," *Chem. Mater.,* **9**, pp.2261 (1997).
12. P. Fedtke, M. Wienecke, M. C. Bunescu, M. Pietrzak, K. Deistung, and E. Borchardt, "Hydrogen sensor based on optical and electrical switching," *Sens. Actuators B,* **100**, pp.151 (2004).
13. E. Higurashi, R. Sawada, and T. Ito, "Monolithically integrated optical displacement sensor based on triangulation and optical beam deflection," *Appl. Opt.,* **38**, pp.1746 (1999).
14. K. T. V. Grattan, "Optical Fiber Sensor Technology" (*Kluwer academic publisher*, 2000).
15. T. G. Giallorenzi, J. A. Bucaro, A. Dandridge, G. H. Sigel, J. H. Cole, S. C. Rashleigh and R. G. Priest, "Optical fiber sensor technology," *IEEE Trans. Micro. Theory Tech.,* **MTT-30**, pp.472 (1982).
16. E. Udd, "Fiber optic sensor," (Wiley Interscience, 2006).
17. H. Y. Fu, H. Y. Tam, L. Y. Shao, X. Dong, P. K. A. Wi, C. Lu, and S. K. Khijwania, "Novel pressure sensor using a polarization-maintaining photonic crystal fiber based Sagnac interferometer," *Appl. Opt.,* **47**, pp.2835 (2008).
18. F. Chiadini, A. Paolillo, and A. Scaglione, "A reflectometric optical fiber temperature sensor," *IEEE J. Sens.,* **3**, pp.80 (2003).

19. T. Lü, and S. Yang, "Extrinsic Fabry-Perot cavity optical fiber liquid-level sensor," *Appl. Opt.*, **46**, pp.3682 (2007).

20. J. Villatoro, and D. M. Hernandez, "Low-cost optical fiber refractive-index sensor based on core diameter mismatch," *J. Lightwave Technol.*, **24**, pp.1409 (2006).

21. B. Gu, M. Yin, A. P. Zhang, J. Qian, and S. He, "Low-cost high-performance fiber-optic pH sensor based on thin-core fiber modal interferometer," *Opt. Express*, **17**, pp.22302 (2009).

22. J. Jensen, P. Hoiby, G. Emiliyanov, O. Bang, L. Pedersen, and A. Bjarklev, "Selective detection of antibodies in microstructured polymer optical fibers," *Opt. Express*, **13**, pp.5883 (2005).

23. M. Belal, Z. Song, Y. Jung, G. Brambilla, and T. P. Newson, "Optical fiber microwire current sensor," *Opt. Lett.*, **35**, pp.3045 (2010).

24. K. Bohnert, M. Ingold, and J. Kostovic, "Fiber-optic voltage sensor for SF6 gas-insulated high-voltage switch gear," *Appl. Opt.*, **38**, pp.1926 (1999).

25. A. M. Boronakhin, A. A. Velikoseltsev, A. N. Tkachenko, A. A. Yankovski, and D. B. Pukhov, "Fiber-optic rotation sensors for seismic measurements," *J. Opt. Technol.*, **77**, pp.447 (2010).

26. W. Shen, X. Wu, H. Meng, G. Zhang, and X. Huang, "Long distance fiber-optic displacement sensor based on fiber collimator," *Rev. Sci. Instrum.*, **81**, pp.123104 (2010).

27. A. Malki, P. Lecoy, J. Marty, C. Renouf, and P. Ferdinand, "Optical fiber accelerometer based on a silicon micromachined cantilever," *Appl. Opt.*, **34**, pp.8014 (1995).

28. Y. Li, X. Wang, and X. Bao, "Sensitive acoustic vibration sensor using single-mode fiber tapers," *Appl. Opt.,* **50**, pp.1873 (2011).

29. R. Gibson, R. Selfridge, and S. Schultz, "Electric field sensor array from cavity resonance between optical D-fiber and multiple slab waveguides," *Appl. Opt.,* **48**, pp.3695 (2009).

30. L. Sun, S. Jiang, and J. R. Marciante, "All-fiber optical magnetic-field sensor based on Faraday rotation in highly terbium-doped fiber," *Opt. Express,* **18**, pp.5407 (2010).

31. D. H. Kim, "A fiber-optic tiltmeter system based on the moire-fringe effect," *Meas. Sci. Technol.,* **20**, pp.025203 (2009).

32. H. Y. Fu, S. K. Khijwania, H. Y. Tam, P. K. A. Wai, and C. Lu, "A novel fiber optic polarimetric torsion sensor based on polarization-maintaining photonic crystal fiber," *Appl. Opt.,***49**, pp.5954 (2010).

33. M. Schmidt, N. Fürstenau, W. Bock, and W. Urbanczyk, "Fiber-optic polarimetric strain sensor with three-wavelength digital phase demodulation," *Opt. Lett.,***25**, pp.1334 (2000).

34. K. O. Hill, and Gerald Meltz, "Fiber Bragg Grating Technology Fundamentals and Overview," *J. Lightwave. Technol.,* **15**, pp.1263 (1997).

35. D. A Jackson, A. B. Lobo Riebeiro, L. Reekie, and J. L. Archambault, "Simple multiplexing scheme for a fiber-optic grating sensor network", *Opt. Lett.,* **18**, pp. 1192-1194 (1993).

36. M. R. Shenoy, S. K. Khijwania, A. Ghatak, and B. P. Pal, "Fiber optics through experiments" (*Viva Books,* 2009).

37. A. Orthonos, "Fiber Bragg Gratings" *Rev. Sci. Instrum.,* **68**, pp.4309 (1997).

38. Y. J. Rao, "In-fiber Bragg grating sensors," *Meas. Sci. Technol.,* **8**, pp.355 (1997).

39. M. G. Xu, J. L. Archambault, L. Reekie, and J. P. Darkin, "Discrimination between strain and temperature effects using dual-wavelength fiber Bragg grating sensors," *IEEE Elect. Lett.,***30**, pp.1085 (1994).

40. Y. Zhao, and Y. Liao, "Discrimination methods and demodulation techniques for fiber Bragg grating sensors" *Opt. & Lasers in Eng.,* **41**, pp.1 (2004).

41. A. Méndez, "Fiber Bragg grating sensors: A market overview", *Proc. SPIE*, **6619**, pp.661905 (2007).

42. B. O. Guan, H. Y. Tam, X. M. Tao, and X. Y. Dong, "Simultaneous Strain and temperature measurement using a superstructure fiber Bragg Grating," *IEEE Photon. Technol. Lett.,* **11**, pp.105 (1999).

43. M. G. Xu, H. Geiger, and J. P. Darkm, "Fiber grating pressure Sensor with enhanced sensitivity using gas - bubble housing," *IEEE Elect. Lett.,* **32**, pp.128 (1996).

44. T. Guo, Q. Zhao, Q. Dou, H. Zhang, L. Xue, G. Huang, and X. Dong, "Temperature-insensitive fiber Bragg grating liquid-level sensor based on bending cantilever beam," *IEEE Photon. Technol. Lett.,* **17**, pp.2400 (2005).

45. H. Y. Au, S. K. Khijwania, H. Y. Fu, W. H. Chung, and H. Y. Tam, "Temperature-insensitive Fiber Bragg Gratings Based Tilt Sensor with Large Dynamic Range," *J. Lightwave Technol.,* **29**, pp.1714 (2011).

46. H. Yu, X. Yang, Z. Tong, Y. Cao, and A. Zhang, "Temperature-Independent rotational angle sensor based on fiber Bragg grating," *IEEE J. Sens.*, **11**, pp.1233 (2011).

47. C. Shen, and C. Zhong, "Novel Temperature insensitive FBG sensor for displacement," *Sens. Actuators A,* **170**, pp.51 (2011).

48. M. D. Todd, G. A. Johnson, B. A. Althouse, and S. T. Vohra, "Flexural Beam-Based Fiber Bragg grating Accelerometers," *IEEE Photon. Technol. Lett.,* **10**, pp.1605 (1998).

49. M. C. Emmons, H. K. D. Kim, G. P. Carman, and W. L. Richards, "Magneto-optic field coupling in optical fiber Bragg gratings," *Opt. Fiber Technol.,* **18**, pp.157 (2012).

50. X. Ni, Y. Zhao, and J. Yang, "Research of a novel fiber Bragg grating underwater acoustic sensor," *Sens. Actuators A,* **138**, pp.76 (2007).

51. X. G. Tian, and X. M. Tao, "Torsion measurement using fiber Bragg grating sensors," *Exp. Mech.,* **41**, pp.248 (2001).

52. T. Yeo, T. Sun, K. T. V. Grattan, D. Parry, R. Lade, and B. Powell, "Polymer-Coated fiber Bragg grating for relative humidity sensing," *IEEE J. Sens.,* **5**, pp.1082 (2005).

53. S. M. Lee, M. Y. Jeong, and S. Saini, "Etched-Core fiber Bragg grating sensors integrated with microfluidic channels," *J. Lightwave Technol.,* **30**, pp.1025 (2012).

54. R. Aneesh, "Experimental studies on the development of nanoparticle based optical fiber humidity sensor with linear response over a large dynamic range," (*PhD Thesis, Indian Institute of Technology Guwahati,* India, 2011).

55. J. M. Lopez-Higuera, C. L. Rodriguez, I. Antonio Quintela, and A. Cobo, "Fiber Optic Sensors in Structural Health Monitoring", *J. of Lightwave Technol.,* **29**, pp.587 (2011).

56. R. Olaru, and C. Cotae, "Tilt sensor with magnetic liquid," *Sens. Actuators A,* **59**, pp.133 (1997).

57. D. Benz, T. Botzelmann, H. Kck, and D. Warkentin, "On low cost inclination sensors made from selectively metalized polymer", *Sens. Actuators A,* **123**, pp.18 (2005).

58. H. Jung, C. J. Kim, and S. H. Kong, "A MEMS-Based electrolytic tilt sensor," *IEEE Sens. Conference,* pp.1199 (2006).

59. Z. W. Zhong, L. P. Zhao, and H. H. Lin, "Development and investigation of an optical tilt sensor," *Opt. Comm.,* **261**, pp.23 (2006).

60. W. Zhou, and L. Cai, "Interferometer for small-angle measurement based on total internal reflection," *Appl. Opt.,* **37**, pp.5957 (1997).

61. P. S. Huang, and J. Ni, "Angle measurement based on the internal-reflection effect using elongated critical-angle prisms," *Appl. Opt.,* **35**, pp.2239 (1996).

62. F. Hua, I. Reading, and F. Z. Ping, "Novel optical sensor for precise tilt angle measurement," *IEEE Conference ICARCV,* pp.1154 (2006).

63. F. Xiaoyong and C. Maosheng "Theoretical analysis of 2D laser angle sensor and several design parameters" *Opt. Laser. Tech*., **34**, pp.225 (2002).

64. L. B. Yuan "Push-pull fiber optic inclinometers based on Mach-Zehnder optical low-coherence reflectometer", *Rev. Sci. Instrum.,* **75**, pp.2013 (2004).

65. Y. G. Lee, H. K. Jang, D. H. Kim, and C. G. Kim, "Development of a mirror mounted fiber optic inclinometer" *Sens. Actuators A,* **184**, pp.46 (2001).

66. J. S. Bajic, D. Z. Stupar, L. M. Manojlovic, M. P. Slankamenac, and M. Zivanov, "A simple, low-cost, high-sensitivity fiber-optic tilt sensor," *Sens. Actuators A,* **185**, pp.33 (2012).

67. B. O. Guan, H. Y. Tam, and S. Y. Liu, "Temperature-independent fiber Bragg grating tilt sensor," *IEEE Photon. Technol. Lett.,* **16**, pp.224 (2004).

68. X. Dong, C. Zhan, K. Hu, P. Shum, and C. C. Chan, "Temperature-insensitive tilt sensor with strain-chirped fiber Bragg gratings," *IEEE Photon. Technol. Lett.*, **17**, pp.2394 (2005).

69. H. J. Chen, L. Wang, and W. F. Liu, "Temperature-insensitive fiber Bragg grating tilt Sensor," *Appl. Opt.*, **47**, pp.556 (2008).

70. H. Bao, X. Dong, C. Zhao, L. Shao, C. C. Chan, and P. Shun, "Temperature-insensitive FBG Tilt Sensor with a large Dynamic Range," *Opt. Comm.*, **281**, pp.968 (2010).

71. S. He, X. Dong, K. Ni, Y. Jin, C. C. Chan, and P. Shum, "Temperature-insensitive 2D Tilt Sensor with three Fiber Bragg Gratings," *Meas. Sci. Technol.*, **21**, pp.025203 (2010).

72. K. Ni, X. Dong, Y. Jin, and H. Xu, "Temperature-independent Fiber Bragg Gratings Tilt Sensor," *Micro. Opt. Technol. Lett.*, **52**, pp.2250 (2010).

73. P. F. C. Antunes, H. F. T. Lima, N. J. Alberto, H. Rodrigues, P. M. F. Pinto, R. N. Nogueira, H. Varum, A. G. Costa and P. S. B. Andre, "Optical fiber accelerometer system for structural dynamic monitoring," *IEEE J. Sens.*, **9**, pp.1347 (2009).

74. V. Ferrari, A. Ghisla, D. Marioli, and A. Taroni, "Silicon resonant accelerometer with electronic compensation of input-output cross-talk," *Sens. Actuators A*, **123**, pp.258 (2005).

75. J. Kalenik, and R. Pajak, "A cantilever optical-fiber accelerometer," *Sens. Actuators A*, **68**, pp.350 (1998).

76. P. F. C. Antunes, H. Varum, and P. S. Andre, "Intensity encoded polymer optical fiber accelerometer," *IEEE Sensors J.*, **13**, pp.1716, (2013).

77. M. Kimura, and K. Toshima, "Vibration sensor using optical-fiber cantilever with bulb-lens," *Sens. Actuators A,* **66**, pp.178 (1998).

78. D. H. Kim, and M. Q. Feng, "Real-Time structural health monitoring using a novel fiber-optic accelerometer system," *IEEE Sensors J.*, **7**, pp.536 (2007).

79. J. M. Corres, J. Bravo, F. J. Arregui, and I. R. Matias, "Vibration monitoring in electrical engines using an in-line fiber etalon," *Sens. Actuators A,* **132**, pp.506 (2006).

80. Y. Zhao, X. G. Li, F. C. Meng, and Z. Zhao, "A Vibration-sensing system based on SMS fiber structure," *Sens. Actuators A,* **214**, pp.163 (2014).

81. J. A. Ferrari, and P. Garcia, "Optical fiber vibration sensor using step interferometry," *Appl. Opt.*, **35**, pp.5667 (1996).

82. T. A. Berkoff, and A. D. Kersey, "Experimental demonstration of a fiber Bragg grating accelerometer," *IEEE Photon. Technol. Lett*., **8**, pp.1677 (1996).

83. Y. Zhu, P. Shum, C. Lu, B. Lacquet, P. Swart, and S. Spammer, "Temperature-Insensitive fiber Bragg grating accelerometer," *IEEE Photon. Technol. Lett*., **15**, pp.1437 (2003).

84. W. Zhou, X. Dong, K. Ni, C. Chan and P. Shum, "Temperature-insensitive accelerometer based on a strain-chirped FBG," *Sens. Actuators A,* **157**, pp.15 (2010).

85. Y. Weng, X. Qiao, T. Guo, M. Hu, Z. Feng, R. Wang, and J. Zhang, "A Robust and Compact Fiber Bragg grating vibration sensor for seismic measurement," *IEEE J. Sens*., **12**, pp. (2011).

86. Q. P. Liu, X. G. Qiao, J. L. Zhao, J. A. Jia, H. Gao, and M. Shao, "Novel Fiber Bragg grating accelerometer based on diaphragm," *IEEE Sensors J*., **12,** pp.3000 (2012).

87. T. Guo, L. Shao, H. Y. Tam, P. A. Krug, and J. Albert, "Tilted fiber grating accelerometer incorporating an abrupt biconical taper for cladding to core recouping" *Opt. Exp.,* **17,** pp.20651 (2009).

88. H. Y. Au, S. K. Khijwania, and H. Y. Tam, "Fiber Bragg grating Accelerometer," *Proc. SPIE.*, **7004**, pp.70042S-1 (2008).

89. A. Stefani, S. Andresen, W. Yuan, N. H. Rasmussen, and O. Bang, "High sensitivity polymer optical fiber Bragg grating based accelerometer," *IEEE Photon. Technol. Lett.*, **24**, pp.763 (2012).

90. A. Fender, W. N. Macpherson, R. R. J. Maier, J. S. Barton, D. S. George, R. I. Howden, G. W. Smith, B. J. S. Jones, S. Mcculloch, X. F. Chen, R. Suo, L. Zhang, and I. Bennion, "Two-axis temperature-insensitive accelerometer based on multicore fiber Bragg gratings" *IEEE J. Sensors*, **8**, pp.1292 (2008).

91. M. Suster, J. Guo, N. Chaimanonart, W. H. Ko and D. J. Young, "A high-performance MEMS capacitive strain sensing system", *J. Microelectromechanical Syst.*, **15**, pp.1069 (2006).

92. Y. Kim, Y. Kim, C. Lee, and K. Sejin, "Thin Polysilicon Gauge for Strain Measurement of Structural Elements", *IEEE J. Sens.,* **10**, pp.1320 (2010).

93. F. J. Arregui, I. R. Matias, and M. L. Amo, "Optical fiber strain gauge based on a tapered single-mode fiber," *Sens. Actuators A,* **79**, pp.90 (2000).

94. E. Li, "Sensitivity-Enhanced fiber-optic strain sensor based on interference of higher order modes in circular fibers," *IEEE Photon. Technol. Lett.,* **19**, pp.1266 (2007).

95. S. W. James, M. L. Dockney, and R. T. Tatam, "Simultaneous and independent temperature and strain measurement using in-fiber Bragg grating sensors," *IEEE Elec. Lett.,* **32**, pp.1133 (1996).

96. S. K. Mondal, U. Tiwari, G. C. Poddar, V. Mishra, N. Singh, S. C. Jain, S. N. Sarkar, K. D. Chattoypadhya, and P. Kumar, "Single fiber Bragg grating sensor with two sections of different diameters for longitudinal strain and temperature discrimination with enhanced strain sensitivity", *Rev. of Sci. instr.,* **80**, pp.103106:1 (2009).

97. O. Fraz, S. Silva, A. Guerreiro, J. L. Santos, L. Ferreira, and F. A. Jo, "Strain sensitivity control of fiber Bragg grating structures with fused tapers," *Appl. Opt.,* **36**, pp.8578 (2007).

98. L. Ren, J. Chen, H. N. Li, G. Song, and X. Ji, "Design and application of a fiber Bragg grating strain sensor with enhanced sensitivity in the small-scale dam model", *Smart Mater. Struct.,* **18**, pp.035015:1 (2009).

99. M. G. Xu, L. Dong, L. Reekie, J. A. Tucknott, and J. L. Cruz, "Temperature independent strain sensor using a chirped FBG in a tapered optical fiber", *Electron. Lett.,* **31**, pp.823 (1995).

100. F. Gu, H. Yu, W. Fang, and L. Tong, "Nano-imprinting polymer Micro/nanofiber Bragg gratings for high sensitivity strain sensing," *IEEE Photon. Technol. Lett.,* **25**, pp.22 (2013).

101. X. Dong, and H. Y. Tam, "Temperature-insensitive strain sensor with polarization-maintaining photonic crystal fiber based Sagnac interferometer," *Appl. Phy. Lett.,* **90**, pp.15113 (2007).

102. J. Ju, and W. Jin, "Photonic crystal fiber sensors for strain and temperature measurement," *J. Sensors*, **2009**, pp.1 (2009).

103. S. M. Lee, S. Saini and M. Y. Jeong, "Simultaneous measurement of refractive index, temperature, and strain using etched-core fiber Bragg grating sensors," *IEEE Photon. Technol. Lett.*, **22**, pp.1431 (2010).

104. T. L. Yeo, T. Sun, K. T. V. Grattan, D. Parry, R. Lode and B. D. Powell, "Fiber-optic sensor technologies for humidity and moisture measurement," *IEEE J. Sens.*, **5**, pp. 1082 (2005).

105. R. Aneesh, and Sunil K. Khijwania, "Titanium dioxide nanoparticle based optical fiber humidity sensor with linear response and enhanced sensitivity," *Appl. Opt.*, **51**, pp.2164 (2012).

106. S. K. Khijwania, K. L. Srinivasan, and J. P. Sing, "Performance Optimized Optical Fiber Sensor for Humidity Measurement," *Opt. Eng.*, **44**, pp.034401 (1-7) (2005).

107. J. M. Corres, J. Bravo, I. R. Matias, and F. J. Arregui, "Non-adiabatic tapered single-mode fiber coated with humidity sensitive nanofilms," *IEEE Photon. Technol. Lett.*, **18**, pp.935 (2006).

108. A. Alvarez-Herrero, H. Guerrero, and D. Levy, "High-sensitivity sensor flow relative humidity based on overlay on side-polished fibers," *IEEE J. Sensors*, **4**, pp.52 (2001).

109. J. A. Francisco, Y. J. Liu, and R. M. Ignacio, "Optical fiber humidity sensor using a nano Fabry–Perot cavity formed by the ionic self-assembly method," *Sens. Actuators B*, **59**, pp.54 (1999).

110. P. Hu, X. Dong, K. Ni, L. H. Chen, W. C. Wong, and C. C. Chan "Sensitivity-enhanced Michelson interferometric humidity sensor with waist-enlarged fiber bitaper," *Sens. Actuators B,* **194,** pp.180 (2014).

111. P. Kronenberg, P. K. Rastogi, P. Giaccari and H. G. Limberger, "Relative humidity sensor with optical fiber Bragg gratings," *Opt. Letts*., **27**, pp.16, (2002).

112. T. L. Yeo, T. Sun, and K. T. V. Grattan, "Characterization of a polymer-coated fiber Bragg grating sensor for relative humidity sensing," *Sens. Actuators B,* **110**, pp.148 (2005).

113. X. F. Huang, D. R. Sheng, K. F. Cen, and H. Zhou, "Low-cost relative humidity sensor based on thermoplastic polymide-coated fiber Bragg grating," *Sens. Actuators B,* **127**, pp.518 (2007).

114. W. Zhang, D. J. Webb, and G. D. Peng, "Investigation into time response of polymer fiber Bragg grating based humidity sensors," *J. Lightwave Technol.,* **30**, pp.1090 (2012).

115. G. Rajan, Y. Noor, B. Liu, E. Ambikairaja, D. Webb, and G. Peng, "A Fast response intrinsic humidity sensor based on etched single mode polymer fiber Bragg grating," *Sens. Actuators A,* **203**, pp.107 (2013).

116. T. Venugopalan, T. L. Yeo, T. Sun and K. T. V. Grattan, "LPG-based PVA coated sensor for relative humidity measurement," *IEEE J. Sensors,* **8**, pp.1093 (2008).

117. H. Chen, Z. Guc, and K. Gao, "Humidity sensor based on cascaded chirped long-period fiber gratings coated with TiO2/SnO2 composite films," *Sens. Actuators B,* **196** pp.18, (2014).

118. K. M. Tan, C. M. Tay, S. C. Tjin, C. C. Chan, and H. Rahardjo, "High relative humidity measurements using gelatin coated long-period grating sensors", *Sens. Actuators B*, **110**, pp.335 (2005).

119. Y. Liu, X. Huang, B. Liu, Y. Miao, H. Zhang, and X. Chen, "Relative humidity sensor based on long period grating with agarose gel coating", *Proc. SPIE*, **8301**, pp.820109:1 (2011).

120. Y. Miao, B. Liu, H. Zhang, Y. Li, H. Sun, W. Zhang and Q. Zhao, "Relative humidity sensor based on tilted fiber Bragg grating with polyvinyl alcohol coating," *IEEE Photon. Technol. Lett.*, **21**, pp.441 (2009).

121. J. Mathew, Y. Semenova, and G. Farrell, "Relative humidity sensor based on an Agarose infiltrated photonic crystal fiber interferometer," *IEEE Quant. Electro.***18**, pp.1553 (2012).

122. H. C. Hesse, "Optical fiber chemical sensor," East German patent 106,086 (1974).

123. F. T. S. Yu and S. Yin, Fiber Optic Sensors (Marcel Dekker, 2002).

124. J. Yang, Y. Zhao, B. J. Peng and X. Wan, "Temperature-compensated high pressure FBG sensor with a bulk-modulus and self-demodulation method", *Sens. Actuators A*, **118**, pp.254 (2005).

125. J. Lim, Q. P. Yang, B. E. Jones, and P. R. Jackson, "DP flow sensor using optical fiber Bragg grating", *Sens. Actuators A*, **92**, pp.102 (2001).

126. R. Aneesh, M. Maharana, H. Y. Tam and S. K. Khijwania, "Simple Temperature-insensitive Fiber Bragg Gratings Based Tilt Sensor with a Tunable Response and a Large Dynamic Range", *Photonics*, (2010).

127. P. Munendhar, R. Aneesh and S. Khijwania, "Development of an All-optical,

Temperature Insensitive Non-pendulum type Tilt Sensor Employing Fiber Bragg Gratings", *Applied Optics*, vol. **52**, pp 5493, (2014).

128. J. Kalenic, and R. Pajak, "A cantilever optical-fiber accelerometer," *Sens. Actuators A*, **68**, pp.350 (1998).
129. Y. Yu, H. Y. Tam, S. Geng, M. S. Demokan, Z. Liu, and W. Chung, "Chirp-free tuning of fiber Bragg grating using cantilever beam" *Jpn. J. Appl. Phys*., **38**, pp.1032 (1999).
130. F. Surre, R. H. Scott, P. Banerji, T. Sun, P. A. M. Basheer and K. T. V. Grattan, "Study of reliability of fibre Bragg grating fibre optic strain sensors for field-test applications", *Sens. & Actuators A,* Vol. **185**, 8-16, (2012).
131. R. Aneesh, and Sunil K. Khijwania, "Zinc oxide nanoparticle based optical fiber humidity sensor having linear response throughout a large dynamic range," *Appl. Opt*., **50**, pp.5310 (2011).
132. A. Iadicicco, A. Cusano, S. Campopiano, A. Cutolo, and M. Giordano, "Thinned fiber Bragg gratings as refractive index sensors," *IEEE J. Sens.*, **5**, pp.1288 (2005).
133. X. F. Huang, Z. Chen, L. Shao, K. Cen, D. Sheng, J. Chen, and H. Zhou, "Design and characteristics of refractive index sensor based on thinned and microstructure fiber Bragg grating," *Appl. Opt*., **47**, pp.504 (2008).
134. W. Liang, Y. Huang, T. Xu, R. K. Lee, and A. Yariv, "Highly sensitive fiber Bragg grating refractive index sensors," *Appl. Phys. Letts.*, **86**, pp.151122 (2005).
135. B. N. Shivananju, S. Yadagni, R. Fazuldeen, A. K. Sarin Kumar, and G. M. Hegde, "CO2 sensing at room temperature using carbon nanotubes coated core fiber Bragg grating," *Rev. Sci. Instrum.*, **84**, pp.065002:1 (2013).

136. S. Sridevi, K. S. Vasu, N. Jayaraman, S. Asokan, and A.K. Sood, "Optical Bio-Sensing Devices Based on Etched Fiber Bragg Gratings Coated with Carbon Nanotubes and Graphene Oxide along with a specific dendrimer," *Sens. Actuators B,* **203**, pp.1 (2014).

137. M. Monerie, "Propagation in Doubly Clad Single-Mode Fibers," *IEEE Trans. Microwave Theo. Techniques,* **18**, pp.381 (1982).